NAVAL POSTGRADUATE SCHOOL
MONTEREY, CALIFORNIA

THESIS

SOLAR HEATING EFFECTS ON BALLOON-BORNE MICROTHERMAL PROBES FOR THE AIRBORNE LASER PROGRAM

by

Daniel J. Richardson

June, 1997

Thesis Advisor: Donald L. Walters
Co-Advisor: D. Scott Davis

Approved for public release; distribution unlimited.

REPORT DOCUMENTATION PAGE

Form Approved OMB No. 0704-0188

1. AGENCY USE ONLY *(Leave blank)*	2. REPORT DATE June 1997	3. REPORT TYPE AND DATES COVERED Master's Thesis

4. TITLE AND SUBTITLE
SOLAR HEATING EFFECTS ON BALLOON-BORNE MICROTHERMAL PROBES FOR THE AIRBORNE LASER PROGRAM

5. FUNDING NUMBERS

6. AUTHOR(S)
Richardson, Daniel J.

7. PERFORMING ORGANIZATION NAME(S) AND ADDRESS(ES)
Naval Postgraduate School
Monterey CA 93943-5000

8. PERFORMING ORGANIZATION REPORT NUMBER

9. SPONSORING/MONITORING AGENCY NAME(S) AND ADDRESS(ES)

10. SPONSORING/MONITORING AGENCY REPORT NUMBER

11. SUPPLEMENTARY NOTES The views expressed in this thesis are those of the author and do not reflect the official policy or position of the Department of Defense or the U.S. Government.

12a. DISTRIBUTION/AVAILABILITY STATEMENT
Approved for public release; distribution is unlimited.

12b. DISTRIBUTION CODE

13. ABSTRACT *(maximum 200 words)*

Atmospheric optical turbulence induces phase fluctuations in a propagating electromagnetic wave. The resulting degradation in coherence limits the capability of any laser, target acquisition, or surveillance system. Past data collection methods for the parameterization of atmospheric turbulence profiles, in support of critical Theater Ballistic Missile Defense (TBM) systems, from ground level to 30 km, have depended on meteorological balloon-thermosonde systems, probes carried on the U.S. Air Force Argus aircraft, as well as radar and optical measurements.. The balloon and aircraft systems measure temperature fluctuations and compute the temperature structure function, C_T^2 and the related index of refraction structure parameter, C_n^2. It has recently become critical to explain why turbulence profiles from daytime thermosonde data consistently show a two order of magnitude increase over that taken during the night, primarily between 12-20 km.

This thesis analyzed the TSI 3.8 μm platinum coated tungsten thermosonde probe used by the USAF Research Laboratory (AFRL) to quantify the magnitude of the solar heating and to investigate other heat transfer mechanisms in the probe. A model of the thin wire probe was developed to identify each of the contributions to the temperature error and its significance. Experimental measurements where collected to verify most aspects of the final model.

We found that the sun induces a temperature rise in the TSI 3.8 μm fine wire probe, during the day, that can vary from near zero to 0.175 K. It is strongly dependent on probe orientation with respect to the sun and on variations in the air flow over the probe. This then causes an apparent increase by two orders of magnitude in the daytime measurements of the optical turbulence parameters C_T^2 and C_n^2.

14. SUBJECT TERMS
thermosonde, optical turbulence, Airborne Laser Program,

15. NUMBER OF PAGES 108

16. PRICE CODE

17. SECURITY CLASSIFICATION OF REPORT	18. SECURITY CLASSIFICATION OF THIS PAGE	19. SECURITY CLASSIFICATION OF ABSTRACT	20. LIMITATION OF ABSTRACT
Unclassified	Unclassified	Unclassified	UL

NSN 7540-01-280-5500

Standard Form 298 (Rev. 2-89)
Prescribed by ANSI Std. 239-18 298-102

Approved for public release; distribution is unlimited.

SOLAR HEATING EFFECTS ON BALLOON-BORNE MICROTHERMAL PROBES FOR THE AIRBORNE LASER PROGRAM

Daniel J. Richardson
Lieutenant Commander, United States Navy
B.S., United States Naval Academy, 1985

Submitted in partial fulfillment
of the requirements for the degree of

MASTER OF SCIENCE IN PHYSICS

from the

NAVAL POSTGRADUATE SCHOOL
June 1997

Author: _____
Daniel J. Richardson

Approved by: _____
Donald L. Walters, Thesis Advisor

_____
D. Scott Davis, Co-Advisor

_____
Anthony A. Atchley, Chairman, Department of Physics

ABSTRACT

Atmospheric optical turbulence induces phase fluctuations in a propagating electromagnetic wave. The resulting degradation in coherence limits the capability of any laser, target acquisition, or surveillance system. Past data collection methods for the parameterization of atmospheric turbulence profiles, in support of critical Theater Ballistic Missile Defense (TBM) systems, from ground level to 30 km, have depended on meteorological balloon-thermosonde systems, probes carried on the U.S. Air Force Argus aircraft, as well as radar and optical measurements.. The balloon and aircraft systems measure temperature fluctuations and compute the temperature structure function, C_T^2 and the related index of refraction structure parameter, C_n^2. It has recently become critical to explain why turbulence profiles from daytime thermosonde data consistently show a two order of magnitude increase over that taken during the night, primarily between 12-20 km.

This thesis analyzed the TSI 3.8 μm platinum coated tungsten thermosonde probe used by the USAF Research Laboratory (AFRL) to quantify the magnitude of the solar heating and to investigate other heat transfer mechanisms in the probe. A model of the thin wire probe was developed to identify each of the contributions to the temperature error and its significance. Experimental measurements where collected to verify most aspects of the final model.

We found that the sun induces a temperature rise in the TSI 3.8 μm fine wire probe, during the day, that can vary from near zero to 0.175 K. It is strongly dependent on probe orientation with respect to the sun and on variations in the air flow over the probe. This then causes an apparent increase by two orders of magnitude in the daytime measurements of the optical turbulence parameters C_T^2 and C_n^2.

TABLE OF CONTENTS

ACKNOWLEDGEMENTS

I would like to express my thanks to those who helped in the completion of this thesis. To my thesis adviser, Dr. Donald L. Walters, I give my special thanks for sharing some of your vast experience in the laboratory from which I learned a great deal both through your instruction and example. I would also like to extend my appreciation to Dr. Alan G. Fox and Mr. Richard Y. Hashimoto, of the NPS Mechanical Engineering Department, whose advice and assistance in the use of the scanning electron microscope provided information which proved to be invaluable in this research.

I. INTRODUCTION

The Airborne Laser Program (ABL) must contend with several problems associated with the propagation of electromagnetic radiation through the atmosphere. Specifically, random fluctuations in the atmospheric index of refraction cause phase front distortions of the propagating plane wave [Ref. 1:p. 6-6]. Other effects such as thermal blooming, absorption and scattering by atmospheric particles, and stimulated Raman scattering are also important but go beyond the scope of this thesis [Ref. 2]. The concept of mounting a weapons class laser on an aircraft has been around for over two decades and was proven possible by the Airborne Laser Laboratory in the 1970's. The technologies to make it practical, however, have only recently been demonstrated by Lockheed Martin and scale laser testing done by the Air Force Research Laboratory in 1995 as part of the ABLE ACE experiment [Ref. 3:p. 6].

The basic requirements of the ABL system are to detect, track, and destroy theater ballistic missiles (TBMs) while still in their boost phase and prior to the missile's leaving the hostile country's own airspace. The ABL system will use a passive infrared (IR) search and track system along with an active Multi-Beam Illuminator (MBIL) laser for accurate positioning and better dwell characteristics during high power Chemical Oxygen Iodine Laser (COIL) missile destruction [Ref. 4:p. 1]. Adaptive optics will be needed to achieve effective ranges beyond ~100km.

The ABL program utilizes atmospheric turbulence data that have been collected by the Air Force Research Laboratory (AFRL), Naval Postgraduate School (NPS), and Argus aircraft for this and other Department of Defense atmospheric laser programs over the past decade. Characterization of atmospheric turbulence is essential in the design and use of atmospheric laser systems. A critical factor in the design is whether a perceived enhancement in the measured temperature structure parameter, C_T^2, during the daytime as compared to night is real or is a consequence of solar heating of the measurement apparatus itself [Ref. 5:p. 30]. Experiments done by AFRL, as well as subsequent ones done by NPS, have shown a significant enhancement in daytime C_T^2 values, most likely caused

solar heating of the thermosonde probes used to do the measurement, coupled with the complications of package rotation, pendulum motion, and probe vibration [Ref. 5:p. 55].

This thesis investigated the systematic effects caused by solar heating of the balloon thermosonde probes used by AFRL and NPS. Extensive probe response modeling and experimental measurements were done to identify and to quantify the individual contributions to temperature variation and to determine if the signal generated would be interpreted as a false turbulence signal within the electronic bandpass of the instrumentation. Package rotation, pendulum motion, and other dynamics where apparent in the experimental data.

The ABL program has entered the Program Definition and Risk Reduction phase (PDRR) which calls for one complete weapon system, including a laser and its controlling system, to be integrated onboard a 747-400 platform and to be successfully demonstrated by 2002. Success of the system will be evaluated by attempting to shoot down a SCUD type missile [Ref. 6:p. 1-2]. Essential risk assessment and management issues underlying the feasibility of proceeding past the project's scheduled acquisition program Authority to Proceed Milestone (ATP) in mid-1998 relies partly on the resolution of the atmospheric turbulence problem. The underlying motivation of this investigation was to identify any systematic error sources that might affect the microthermal platinum coated tungsten probes that provide critical turbulence measurements needed for effective deployment of theater ballistic missile defense systems.

II. BACKGROUND

A. OPTICAL TURBULENCE PARAMETERS

Atmospheric turbulence degrades the wave front of a collimated laser beam. Random fluctuations in the atmospheric index of refraction, n, caused by temperature and humidity inhomogeneities, induce centroid wander, beam broadening, and interference that all reduce the beam's spatial coherence (Figure 2-1) [Ref. 7:p. 1].

Tatarski and others have developed useful parameters for the statistical quantification of optical turbulence in the atmosphere by defining so-called structure functions. By describing the atmosphere as a three dimensional random field Tatarski considered the correlation function of some relevant quantity of interest, f, as [Ref. 7:p. 3]

$$B_f(t_1,t_2) = \left\langle \left[f(t_1) - \langle f(t_1) \rangle \right] \left[f^*(t_2) - \langle f^*(t_2) \rangle \right] \right\rangle, \tag{1}$$

where the angled brackets denote the mean value, the superscript star is the complex conjugate, and t denotes time. Because the atmosphere is not statistically homogenous or stationary, the mean values $\langle f(t_1) \rangle$ are not well defined. To avoid this problem Kolmogorov and Tatarski introduced the structure function

$$D_f(t_1,t_2) = \left\langle \left[f(t_1) - f(t_2) \right]^2 \right\rangle, \tag{2}$$

which characterizes the intensity of the particular random fluctuations of f(t) [Ref. 7:p. 9-10]. For our use then, a structure function tensor can be described by the mean square difference between two measurements, such as temperature, by

$$D_T(\vec{r}_1,\vec{r}_2) = \left\langle [(T(\vec{r}_1) - T(\vec{r}_2)]^2 \right\rangle. \tag{3}$$

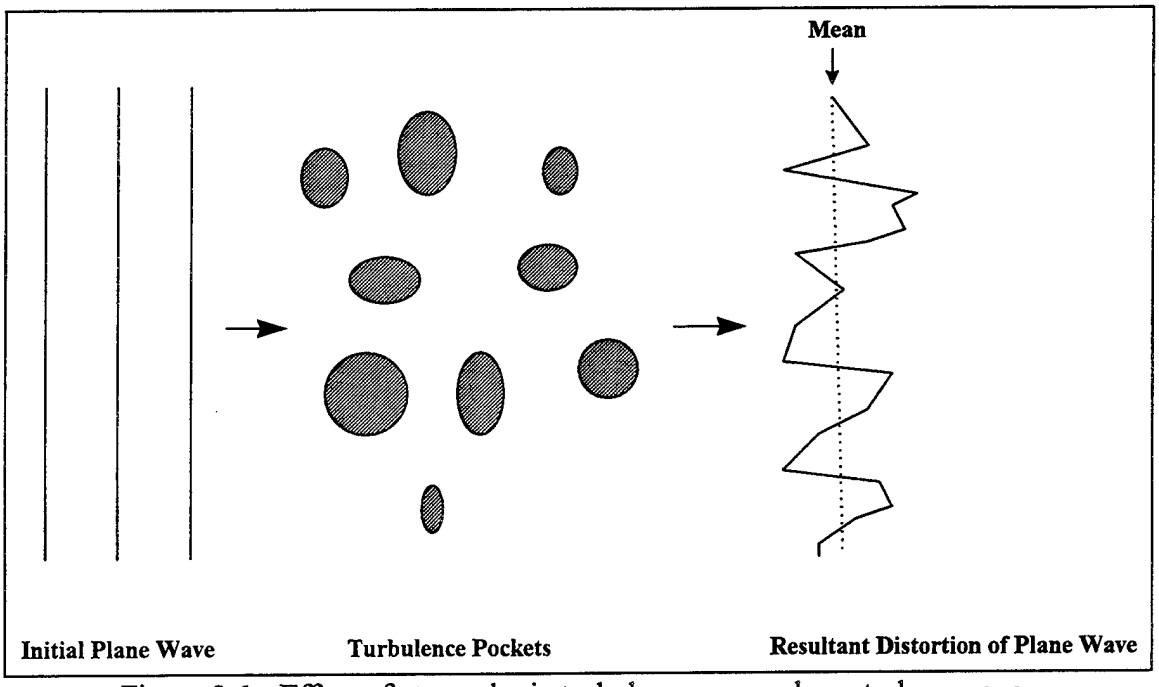

Figure 2-1: Effect of atmospheric turbulence on a coherent plane wave.

For an isotropic and homogeneous quantity the structure function must necessarily be independent of the orientation angle and absolute position, and can depend only on r, the distance between the two observation points:

$$r = \left|\vec{r}_1 - \vec{r}_2\right|. \tag{4}$$

Although the atmosphere is generally not isotropic or homogenous, if r is sufficiently small, then some local volume may be sufficiently isotropic and homogenous to permit credible measurements [Ref. 7:p. 31].

It is found that the statistical behavior of the atmosphere is well behaved over a limited range of r, $l_0 \le r \le L_0$. This is called the inertial subrange. The inertial subrange is bounded on the lower end by l_0, which is the small scale turbulence region associated with viscous eddy dissipation. On the upper end of the inertial subrange, L_0 defines the outer scale length, which is the largest eddy size that can be considered isotropic throughout its volume [Ref. 8].

Kolmogorov and Obukhov proposed that the structure functions in the atmosphere have a $r^{2/3}$ dependence [Ref. 7:p. 31]. Assuming isotropic and homogenous conditions,

Tatarski proposed the temperature structure function, C_T^2 by normalizing Eq. (3) by $r^{2/3}$ [Ref. 7:p. 46]

$$C_T^2 = \frac{D_T(r)}{r^{\frac{2}{3}}} = \frac{\left\langle [T(\vec{r}_1) - T(\vec{r}_2)]^2 \right\rangle}{r^{\frac{2}{3}}}. \tag{5}$$

Since $n-1$ is proportional to density, which is a function of the pressure, P, in millibars and temperature, T, in K, the inertial range refractive index structure parameter, C_n^2, is related to the temperature structure parameter by

$$C_n^2(z) = \left[79.9x10^{-6} \frac{P(z)}{T^2(z)} \right]^2 C_T^2(z), \tag{6}$$

where z is the altitude in meters [Ref. 7:p. 79]. The temperature structure parameter, C_T^2, is measured by fine wire temperature sensors in a balloon or aircraft system as a function of altitude. C_n^2 is then computed from C_T^2 using Eq. (6).

The effects of turbulence on a laser beam propagating through the atmosphere appear as distortion in the final beam pattern at the target. A common measure of beam quality is the Strehl ratio, which is the relative intensity of the beam's point spread function measured at the mean centroid location relative to that of an ideal, diffraction limited optical system [Ref. 9]. The Strehl ratio depends on the spatial coherence of the laser radiation after passing through the atmosphere, which in turn depends on the atmospheric turbulence and its effects on the modulation transfer function [Ref. 18]. The atmospheric modulation transfer function (MTF), characterized by the transverse coherent path length r_o, is a measure of electric field transverse autocorrelation length, [Ref. 1:p. 6-29]. Fried showed that, for plane waves,

$$r_o = 2.1[1.46k^2 \int_0^L C_n^2(z)dz]^{\frac{-3}{5}}, \tag{7}$$

where k is the optical wave number ($2\pi/\lambda$) and L is the optical path length [Ref. 10:p. 397]. Values of r_0 range from centimeters under very turbulent conditions to meters

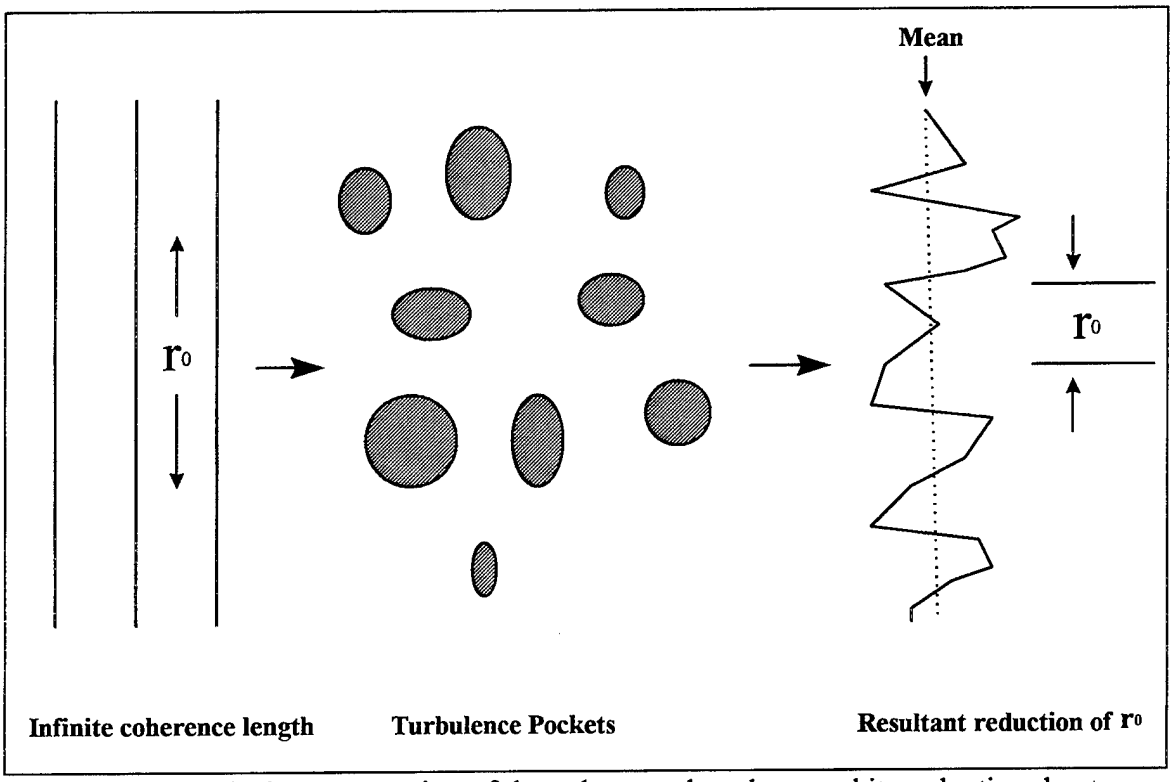

Figure 2-2: Physical representation of the coherence length, r_0, and its reduction due to atmospheric turbulence.

when turbulence is very low. Since r_0 describes the spatial coherence of the beam, the larger its value the better (Figure 2-2). The diffraction limit of the system, however, depends on the geometry of the optical system as well as r_0. Without turbulence the diffraction-limited resolution in radians for a circular aperture is [Ref. 11:p. 393]

$$\Delta\phi_{\min} = \frac{1.22\lambda}{D}, \tag{8}$$

where λ is the wavelength and D is the aperture diameter. When $D>r_0$, the effective turbulence-limited angular resolution just becomes

$$\Delta\phi_{\min} = \frac{\lambda}{r_0}. \tag{9}$$

The isoplanatic angle, θ_0, is another useful statistical parameter for the characterization of atmospheric optical turbulence. It is related to r_0, and represents a measure of the angular field of view of an optical system. It characterizes a cone within the atmos-

phere with similar turbulence characteristics. Fried [Ref. 12] showed that θ_0 depends on the integration of C_n^2 along an optical path and is given by

$$\theta_0 = \left[2.905k^2 \int_0^L C_n^2(z) z^{5/3} dz \right]^{-3/5}, \tag{10}$$

with L, the optical path length in meters.

As has been previously stated, current balloon and aircraft probe thermosonde systems can measure C_T^2 and then compute C_n^2 as a function of altitude and time. Using Eqs. (8) and (9) this data provides the basis for computing r_0 and θ_0 for a particular application in the design and development of an adaptive optics system.

B. THERMOSONDE

The AFRL thermosonde design used during the last decade consists of a VIZ 8000 electronics package with two fine wire TSI 3.8 μm platinum coated tungsten probes exposed to the ambient atmosphere and separated by 1 m (Figure 2-3). This system measures the wires' resistance fluctuations caused by changes in temperature. The balloon carrying the package is capable of ascending to an altitude of approximately 30 km.

Changes in the probe resistance, R_W, give the temperature, T_W, through the relation

$$R_W = R_0 + [1 + \alpha(T_W - T_0)] \tag{11}$$

[Ref. 13:p. 11], where R_0 and T_0, are values at a specific reference resistance and temperature respectively and α is a constant for the particular wire composition and geometry, platinum coated tungsten in this instance. In practice, the two probes form the opposing elements of an AC Wheatstone bridge. The difference in resistance from the Wheatstone bridge is amplified and converted to a temperature change by [Ref. 14:p. 15]

$$\Delta T = \frac{(R_2 - R_1)}{\alpha R_0}. \tag{12}$$

The probe data channels are sampled every 10 s along with ambient pressure, mean temperature, and humidity. The data are radioed via the modified VIZ 8000 radiosonde to the ground station that continuously displays and stores the data on a PC. Optimum thermosonde performance requires a compromise in the probe current. A value of 0.1 ma for a 20 Ω probe provides sufficient signal without inducing temperature differences above 0.002 K between the probe and the atmosphere. The ohmic heating temperature difference, ΔT_W, is

$$\Delta T_W = \frac{q_w}{A_s h}, \tag{13}$$

where q_w is the electrical power input, A_s is the surface area of the wire, and h is the coefficient of heat transfer [Ref. 14:p. 17].

The response of the probe to a change in temperature must be faster than the actual fluctuation to be measured if a meaningful measurement is to result. Failure of the probe response to follow the actual atmosphere will cause an underestimate of the structure function. The response time of our probe is given as [Ref. 14:p. 20]

$$\tau = \frac{\rho\left(\frac{\pi D^2 L}{4}\right)c}{h(\pi DL)} = \frac{\rho Dc}{4h}. \tag{14}$$

with:

ρ = density of probe wire (kg/m^3),
c = heat capacity of wire (J/kg K,
h = convective heat transfer coefficient ($W/m^2 K$),
D = wire diameter (m).

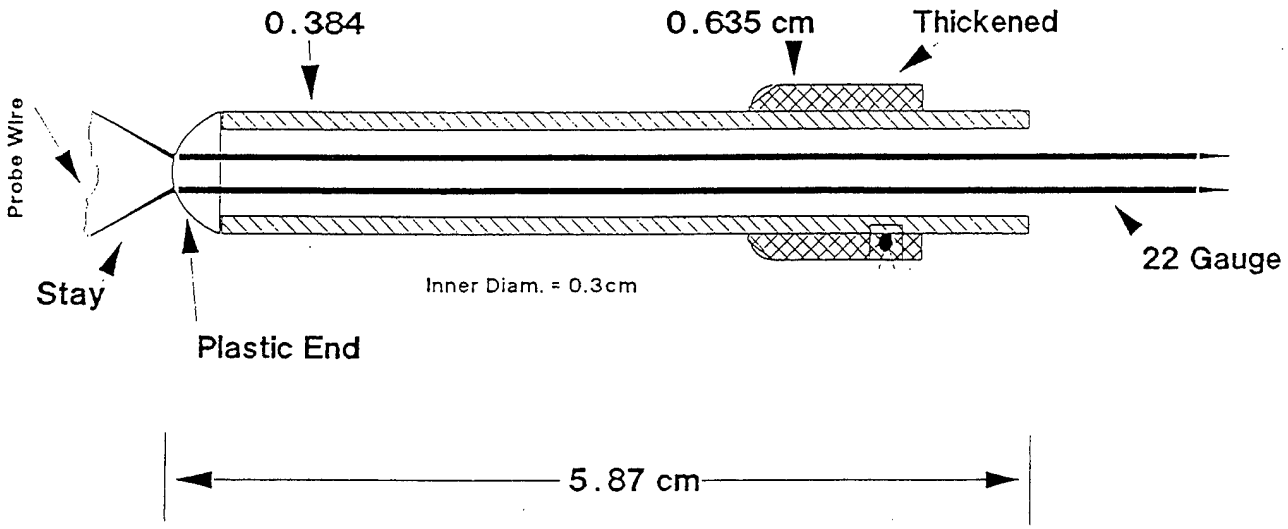

Figure 2-3: Construction layout of platinum coated tungsten AFRL probe and support.

C. CURRENT APPLICATIONS

The apparent increase in turbulence during the day compared to night has significant implications on the ABL program (Appendix A). Current performance specifications for the ABL's COIL laser require the destruction of a ballistic missile that is still in it's boost phase out to a range of several hundred kilometers [Ref. 15:p. 1]. The power requirements on target for these ranges have only recently become possible with the use of adaptive optical systems that rely on active compensation of wave front distortion of the propagating laser beam. Still, only under favorable atmospheric conditions can ranges such as these be attained. If existing daytime balloon measurements of C_T^2 are valid they imply that the useful range of the laser system is severely limited in the daytime. Other new programs which rely on laser propagation through the atmosphere to great distances would also have to be substantially re-thought.

D. PRE[illegible]US RESULTS

Numerous experiments have been performed by AFRL and NPS to characterize the microthermal probes and to determine C_T^2 and C_n^2 during day and night conditions. Brown has flown many balloon launches since July of 1981 and performed extensive analysis to show that the probe supports do not contribute to observed diurnal differences [Ref. 5, 14, and 16]. Walters, Weitekamp, Roper, and others through multiple balloon launch experiments (notably from 31 May to 3 June 1990 at AMOS observatory on Mt. Haleakala, Hawaii and 4 -9 December 1990 at Holloman Air Force Base, New Mexico) showed that solar contamination of data was a real effect. Figure 2-4 is a representative example of night time data collected over Maui on 2 June 1990 showing that at least some of the raw C_n^2 data reached the lower noise limit (solid line) of the sonde electronics. Figure 2-5, shows a two order of magnitude shift in C_n^2 data for a next day launch from the same location. None of the data approached the noise limit of the electronics. One would expect that under normal conditions, there should be some parcel of air within the atmosphere that is not turbulent. Yet the measurements show that that assumption is valid at night but not during the day. Hence some doubt has been cast on the general validity of the daytime measurements.

Additional work by Walters, Weitekamp, and Roper have also shown that balloon wake effects are not a source of contamination [Ref. 17 and 18]. Additional attempts at methods of sonde stabilization have also been investigated by them to eliminate solar effects, but to date no satisfactory method has been found.

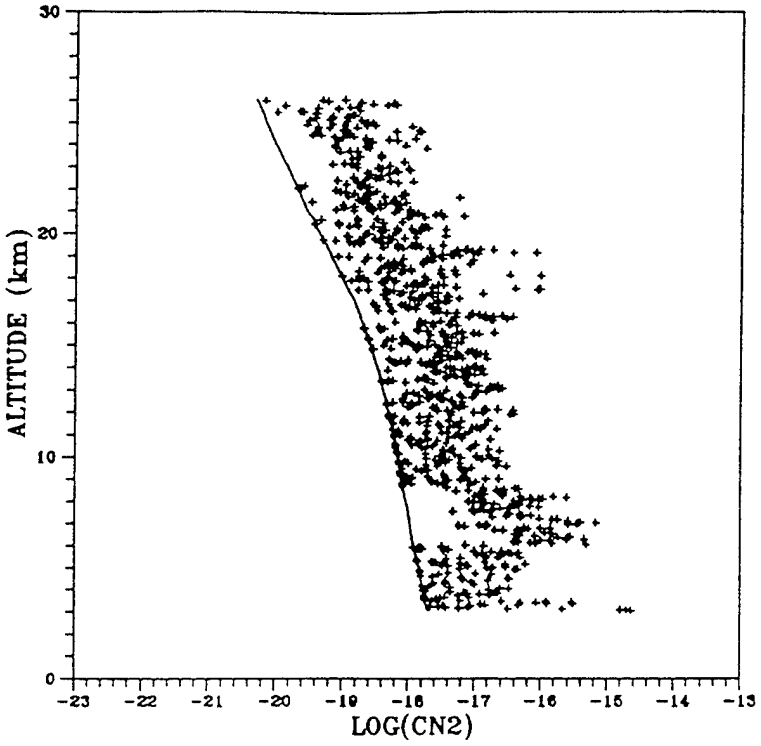

Figure 2-4: Raw night time AFRL probe C_n^2 data collected on Maui, 2 June 1990 showing the lower electronic noise limit (solid line) and corresponding data points near this.

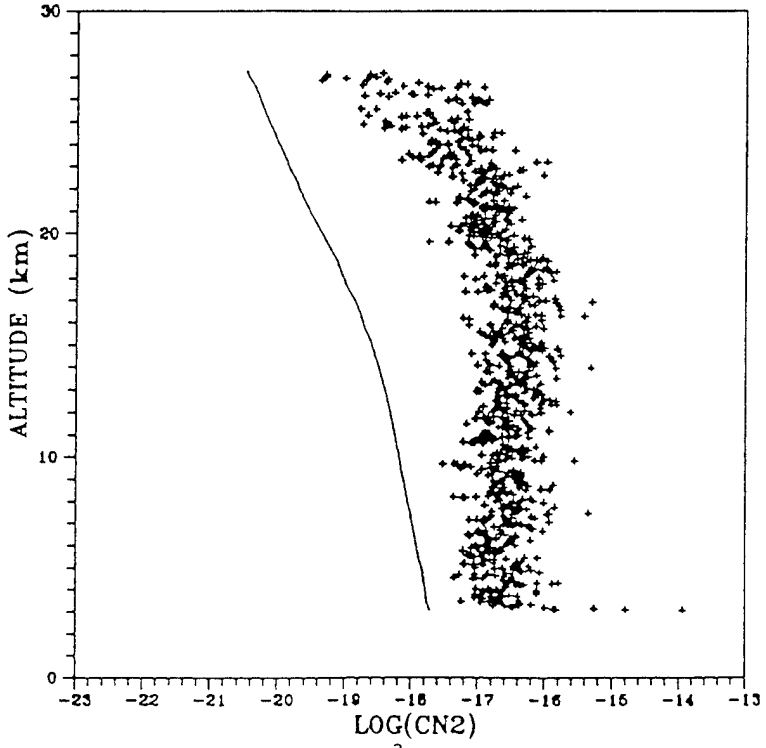

Figure 2-5: Raw day time AFRL probe C_n^2 data collected on Maui, 2 June 1990 showing the lower electronic noise limit (solid line) and corresponding data points with solar induced shift of two orders of magnitude.

III. MODELING THERMOSONDE PROBE HEAT TRANSFER EFFECTS

A. INTRODUCTION

In this Chapter, the heat balance equation for the TSI probe wire is described in detail. Special attention is paid to convective cooling of the wire, the effects of changing solar illumination areas, and effective free stream velocity fluctuations. MATLAB programming was used to model the probe under these changing conditions as a function of altitude. Once the model was validated by experimental measurement as described in Chapter IV, simulations of different probes' responses to material and geometry changes was investigated as shown in Chapter V.

B. HEAT BALANCE EQUATION

The equilibrium temperature of a fine wire probe is given by the heat balance equation

$$Q_{conv} + Q_{solar} + Q_{refl} + Q_{planck} + Q_{Ohmic} = 0, \tag{15}$$

where:

Q_{conv} = convective transfer of power from the probe to the atmosphere (W),
Q_{solar} = solar power absorbed directly by the probe (W),
Q_{refl} = reflected solar power from the Earth absorbed by the probe (W),
Q_{planck} = Planck radiation power transfer between the probe and the environment (W),
Q_{ohmic} = ohmic heating caused by current in the probe wire (W).

In terms of power (W) the equilibrium condition is

$$-hA_1\Delta T + \alpha A_2 P_s + \alpha A_4 P_s \gamma + (\varepsilon A_6 P_{atm} - \varepsilon\sigma A_3 T^4 + \varepsilon A_5 P_e) + I^2 R = 0. \tag{16}$$

The individual terms in Eq. (16) will be defined in the section in which the heat transfer mechanism is introduced. The thin wire probe areas A_1 -A_6 depend on the heat transfer mechanism, package pendulum motion and rotation, probe wire vibration, and solar zenith angle and are also defined in their appropriate sections.

The time for wire to reach thermodynamic equilibrium is short compared to the heat transfer time via convection, so equilibrium was assumed [Ref. 17:p. 32]. Thermal conduction through the probe wire to the supports was also ignored as shown in [Ref. 5:p. 45] for the simulation, but was experimentally measured as described in Chapter IV.

During flight, the effective free stream air velocity over the probe wire is also variable. Variations in the wind velocity alter the heat transfer from a probe that has a different temperature from the air. These fluctuations were modeled both as a steady state characteristic air velocity (V= 5 m/s) and as a random fluctuation distribution about a characteristic free stream velocity (Figure 3-1).

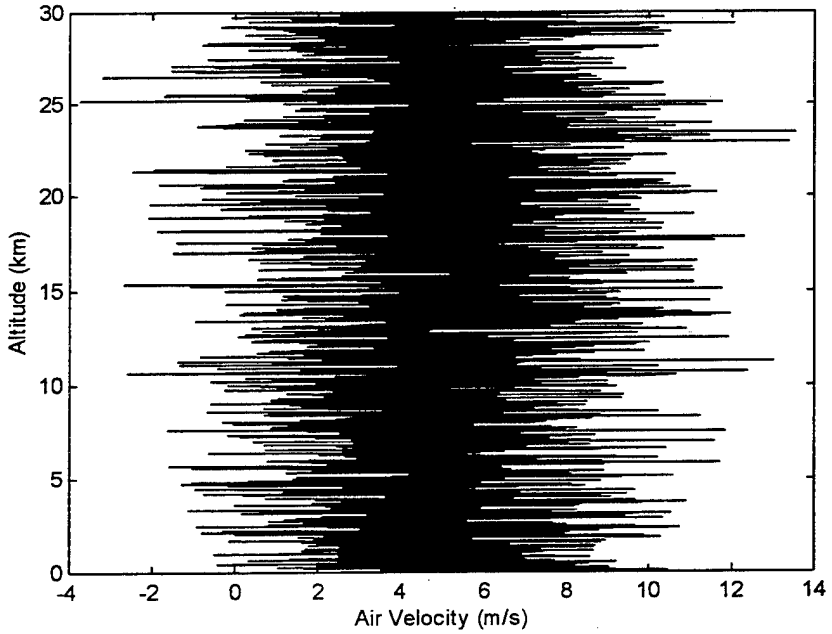

Figure 3-1: Simulation of air velocity fluctuation over probe wire for a fluctuation of 2.5 m/s about a velocity of 5 m/s.

C. CONVECTIVE COOLING

1. Convection with Steady State Free Stream Velocity

The convective transfer of power from the probe wire to the atmosphere is

$$Q_{conv}=hA_1\Delta T, \tag{17}$$

where:

h = convective heat transfer coefficient (W/m^2 K),
$A_1 = \pi DL$ = surface area of the probe subject to convection (m^2),
$\Delta T = T_{probe} - T$ (K).

Heat transfer from a heated probe wire to the atmosphere consists of free convection from buoyancy effects at low air velocity, forced convection at higher air velocities (Reynolds numbers, Re >0.5), and mixed free and forced convection between both these regions, about Re=0.5 [Ref. 20:p. 323]. Figure 3-2, developed by Collis and Williams, illustrates the complicated behavior of this low Re region.

The Reynolds number is the ratio of inertial to viscous forces on a parcel of fluid. In this application,

$$\mathrm{Re} = \frac{DV}{\nu}, \tag{18}$$

where D is the probe diameter, ν, is the kinematic viscosity (which is the ratio of dynamic viscosity, μ, and density, ρ) and V is the characteristic velocity [Ref. 21:p.54]. The NPS-AFRL probe, as modeled, would experience Reynolds number as low as 0.00024 but no more than about 4. The Nusselt number

$$Nu = \frac{hD}{k_t}, \tag{19}$$

is another useful dimensionless number describing the heat transfer coefficient, where k_t is the thermal conductivity of the fluid, in this case air.

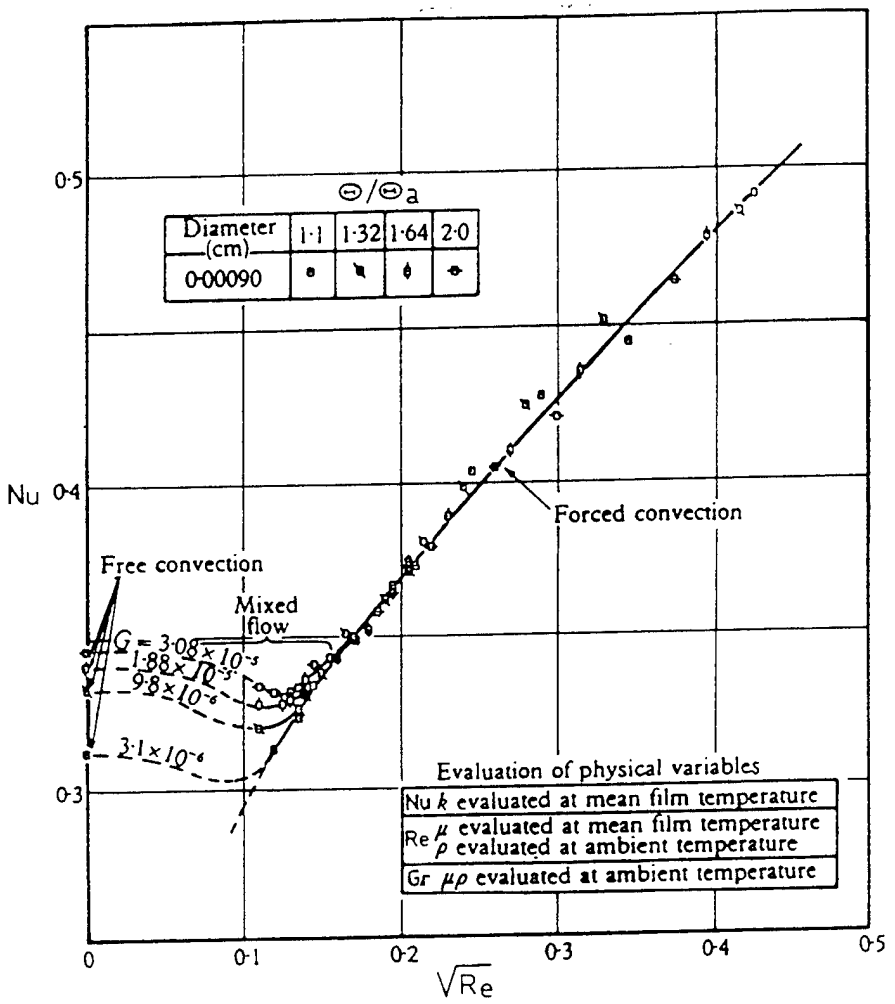

Figure 3-2: Interaction of free and forced convection from [Ref. 27].

At low Reynolds numbers, where buoyancy becomes important, the dimensionless Grassof number, given by

$$Gr = \frac{\rho^2 g \beta_2 (T_{probe} - T) D^3}{\mu^2}, \tag{20}$$

relates the ratio of buoyant to viscous forces near the wire where g is the local gravitational acceleration and β_2 is the coefficient of expansion of the fluid. The Grassof number is important when $Re<Gr^{1/3}$ and buoyant effects become a significant contributor to the probe's ability to dissipate heat [Ref. 22:p. 131]. Grassof numbers modeled for our probe varied from near zero to 3.25×10^{-8}. The effect of the Grassof number on the buoyancy effect for low Reynolds number is also shown in Figure 3-2. At altitudes above 30 km molecular diffusion becomes dominant over convective effects for the heat transfer mechanism of the AFRL probe wire [Ref. 14:p. 19].

2. Determination of h

The convective heat transfer coefficient h is the heat flux leaving the wire surface per unit temperature difference between the wire and the free stream. The effect of h on the probe is significant and is a complex function of geometry, Reynolds, Grassof, and Prandtl numbers as well as the overheat ratio, $(T_{probe}-T)/T$ [Ref. 23: p.352]. The dimensionless Prandtl number, Pr, is the ratio of the momentum diffusivity to the heat diffusivity and is given by

$$\Pr = \frac{\mu c_p}{k_t}. \tag{21}$$

The conductivity k_t is defined in Table 3-1, and c_p is the specific heat of the atmosphere.

The convective heat transfer coefficient can be found using a variety of methods. Most relate the Nusselt , Reynolds, and Prandl numbers and are valid over certain Reynolds and Nusselt number regimes, probe geometries and fluid/gas compositions. No single credible model for our probe's entire operating environment was found. Four different models were compared, and the relative merits of each were contrasted to our probe's

actual performance. Consideration was also given to the physical processes that were included in the model. The four methods considered are summarized below.

a. h, Using Kothandaraman and Subramanyan's Method

Kothandaraman and Subramanyan in [Ref. 24: p. 91] proposed the following relation for the Nusselt number

$$Nu_D = \frac{hD}{k_t} = C\,\mathrm{Re}^n, \tag{22}$$

where k_t is the conductivity of the fluid (air) determined empirically in Table 3-1:

Altitude (km)	**0-12**	**12-20**	**20-32**
k_t **(W/mK)**	$\frac{Alt - 50.57}{-1983.47}$	0.0195	$\frac{Alt + 206.5}{+11636}$

Table 3-1: Conductivity k_t of atmosphere variation with altitude in kilometers, adapted from the Geophysics Handbook [Ref. 25:p. 14-6].

C and n are constants as given in [Ref. 24:p. 91] for the Reynolds number range $0.4<\mathrm{Re}<4.0$ and have values of C=0.891 and n=0.330. Values of Re less than 0.4 require further extrapolation, as done in [Ref. 17]. The altitude, Alt, here and throughout, is given in kilometers. A characteristic velocity V of 5 m/s, corresponding to the approximate ascent rate of the balloon, and characteristic length D of 4.7 μm (measured fine wire probe diameter; refer to Chapter V) were used. A more elaborate treatment for modeling the effective velocity over the probe wire was done in Ref. 5:p. 7-9 and Ref. 19:p. 22, but for our methods this characteristic velocity will be sufficient. The density assumed the validity of the ideal gas law

$$P = \frac{\rho RT}{M}, \tag{23}$$

and modeled the pressure variation with altitude by

$$P = p_0 e^{\frac{-z}{z_0}}. \tag{24}$$

R, above, is the universal gas constant (8.31 J/Mole-K) and M is the mean molecular weight of the atmosphere (28.9644 kg/kMol) [Ref. 25:p. 14-5]. Atmospheric temperature variation with altitude, T, came from the USAF Geophysics Handbook and is shown in Table 3-2. The scale height, z_0, and scale pressure, p_0, are 8.1 km and 1013 mBar (101.3 kPa) respectively [Ref. 25:p. 14-5].

Altitude (km)	**0-11**	**11-20**	**20-32**
T (K)	$\frac{Alt - 44.62}{-0.15493}$	217	$\frac{Alt + 142.75}{0.75}$

Table 3-2: Atmospheric mean temperature variation with altitude adapted from the Geophysics Handbook [Ref. 25:p. 14-3].

Dynamic viscosity was determined using the relation

$$\mu = \frac{\beta_1 T^{\frac{3}{2}}}{T + S}, \tag{25}$$

[Ref. 25:p. 14-5]. Here β_1 is a constant (1.45×10^{-6} kg/s-m-$K^{1/2}$) and S is Sutherland's constant (110.4 K).

With all quantities known and solving for h we find

$$h = \frac{C \mathrm{Re}^n k}{D}. \tag{26}$$

For this probe the diameter, D, was 4.7 μm and the length, L, was 4.15 mm.

b. h, Using Kramer's Method

Kramer's law for circular cylinders of infinite length is given by Hinze in [Ref. 26:p. 201] as

$$Nu = 0.42 \mathrm{Pr}^{0.20} + 0.57 \mathrm{Pr}^{0.33} \mathrm{Re}^{0.50}. \tag{27}$$

Kramer's law is valid for Reynolds numbers in the range $0.1 < \mathrm{Re} < 10{,}000$ [Ref. 19:p. 63]. So now using Eq. (23), h can be found.

c. h, Using Zijnen's Method

The heat transfer proposed by Zijnen does not have any stated valid Reynolds number range for circular cylinders and is given as [Ref. 19:p. 64]

$$Nu = 0.38\,\mathrm{Pr}^{0.2} + (0.56\,\mathrm{Re}^{0.5} + 0.001\,\mathrm{Re})\,\mathrm{Pr}^{0.333}. \tag{28}$$

Once again Eq. (23) is used to solve for h.

d. h, Using Collis and William's Method

Collis and Williams developed the following relation for the Nusselt number [Ref. 27:p. 357-384]

$$Nu_f = (A + B\,\mathrm{Re}_f^n)\left[\frac{T_{probe} - T}{T}\right]^{0.17}. \tag{29}$$

For air and in the Reynolds number range 0.02<Re<44 the constants are as follows: n=0.45, A=0.24, and B=0.56 [Ref. 22:p. 130]. The subscript f denotes measurements were taken at the film temperature which is the average temperature between the wire and the atmosphere. Eq. (23) then gives the relation for h in this method.

Baille further modified this relation to account for the mixed convection effects in the region around Re<0.15, as shown in Figure 3-2, by introducing an effective Reynolds number, Re_{eff}, given by

$$\mathrm{Re}_{eff}^2 = \mathrm{Re}_f^2 + (0.9Gr^{0.418})^2. \tag{30}$$

Baille also investigated the error associated with assuming an infinite cylindrical probe in the above approximations and developed Figure 3-3, which shows the effect of aspect ratio (2l/D) on the Nusselt number [Ref. 22:p. 132]. The AFRL probe used has an aspect ratio of over 2000 and therefore behaves as an infinite wire to high degree.

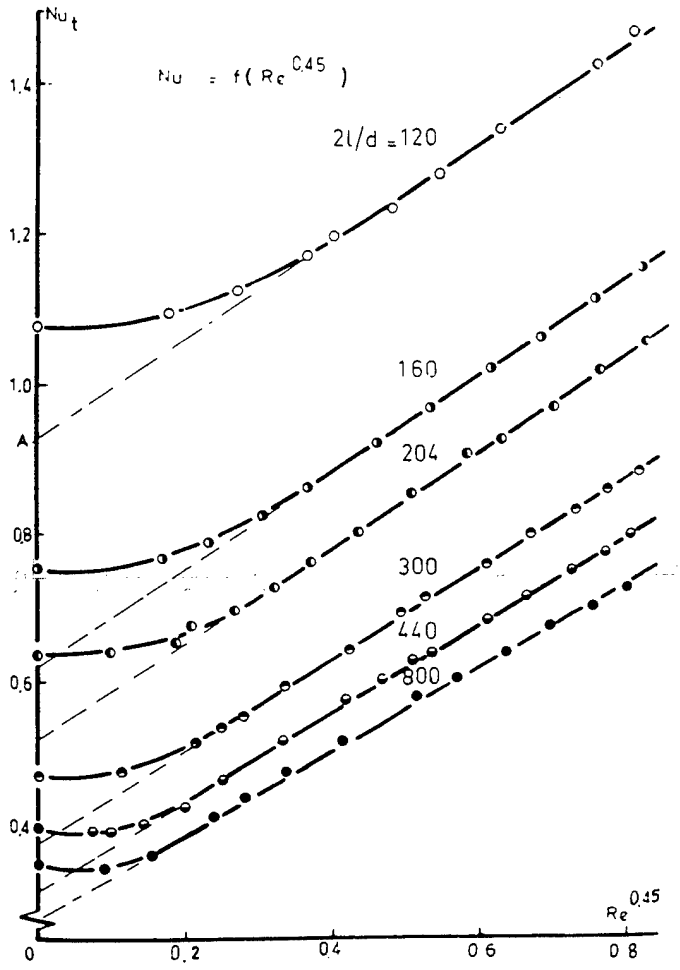

Figure 3-3: Effect of wire aspect ratio on Nusselt number. From [Ref. 22:p. 132].

e. Comparison of h Values

Although no method covered the extremely low Reynolds numbers encountered in this work, the Collis and Williams method best represented the physical effects encountered and the behavior of our probe that is as most represented by the low Reynolds number regions shown in Figure 3-2. All four methods were in good agreement at Reynolds numbers greater than 1. Final values for the coefficient of heat transfer for air velocities of 0 and 5 m/s as derived from the Collis and Williams technique are shown in Figure 3-4.

The kink in the curves in Figures 3-4 to 3-9 around 12 km comes from the rate of change of temperature versus altitude of this part of the stratosphere.

Figure 3-5 summarizes the coefficient of heat transfer values for the four methods as a function of altitude for an air velocity of 5 m/s using a MATLAB program (Appendix B). This program was also used to produce the plots of the, Re, Nu, and Gr numbers, atmospheric temperature T and kinematic viscosity ν versus altitude, as shown as Figures 3-6 to 3-11 for the steady state free stream velocity of 5 m/s and as a function of altitude.

Although not a factor with balloon mounted probes, those mounted on aircraft, such as Argus, also need to consider the heat loss effects at different Mach numbers. Spangeuberg [Ref. 22:p. 133] presents the reported heat loss at various Mach numbers and is reproduced here as Figure 3-12.

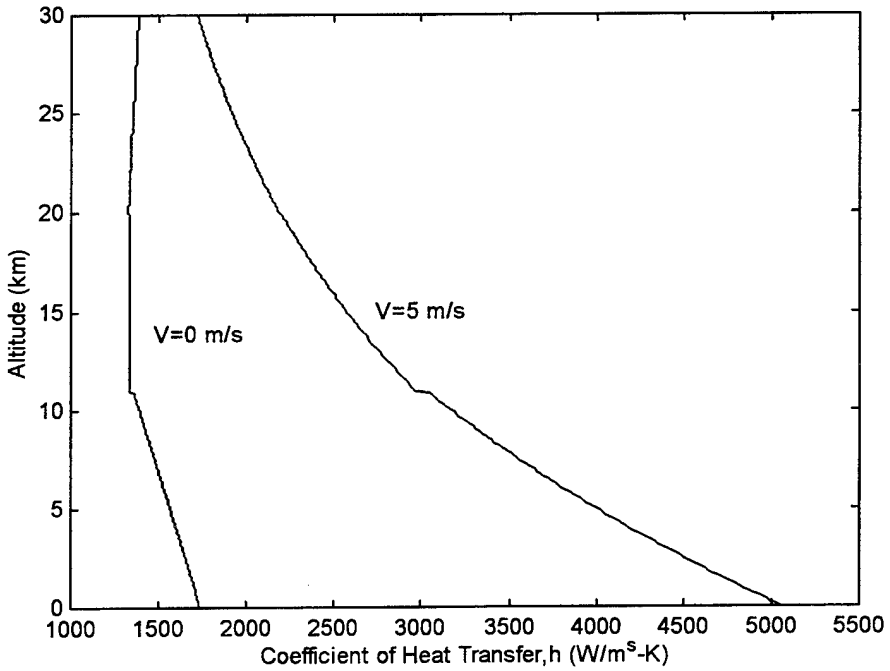

Figure 3-4: Convective heat transfer coefficient of 4.7 μm probe using Collis and Williams method versus altitude with constant free stream velocity of 0 and 5 m/s.

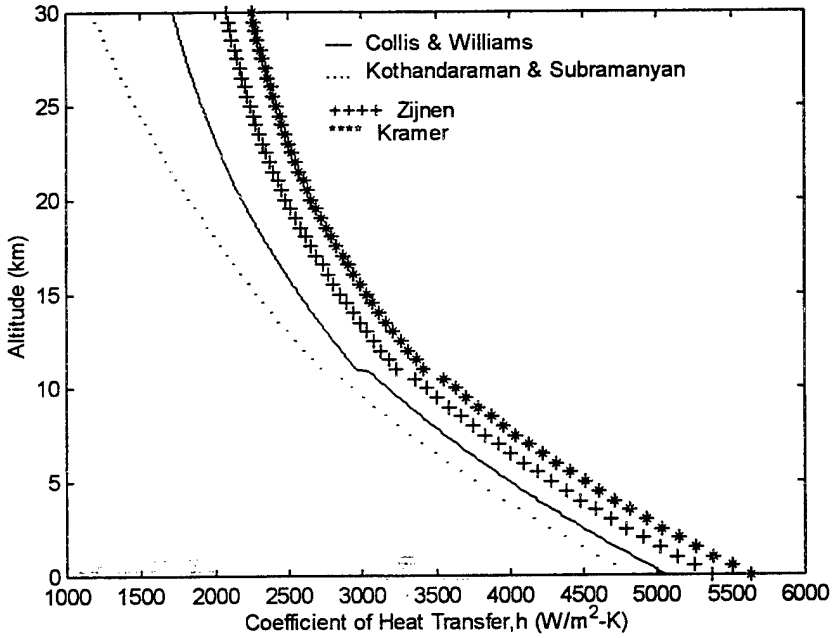

Figure 3-5: Comparison of h, for the 4.7 μm probe, using the four methods investigated at an air velocity of 5 m/s.

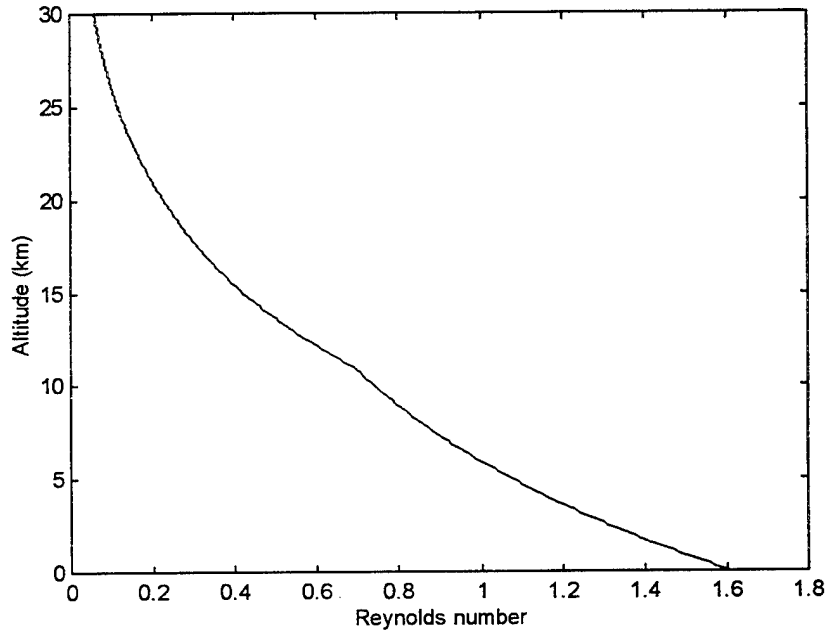

Figure 3-6: Reynolds number versus altitude, for the 4.7 μm probe, for a constant free stream velocity of 5 m/s.

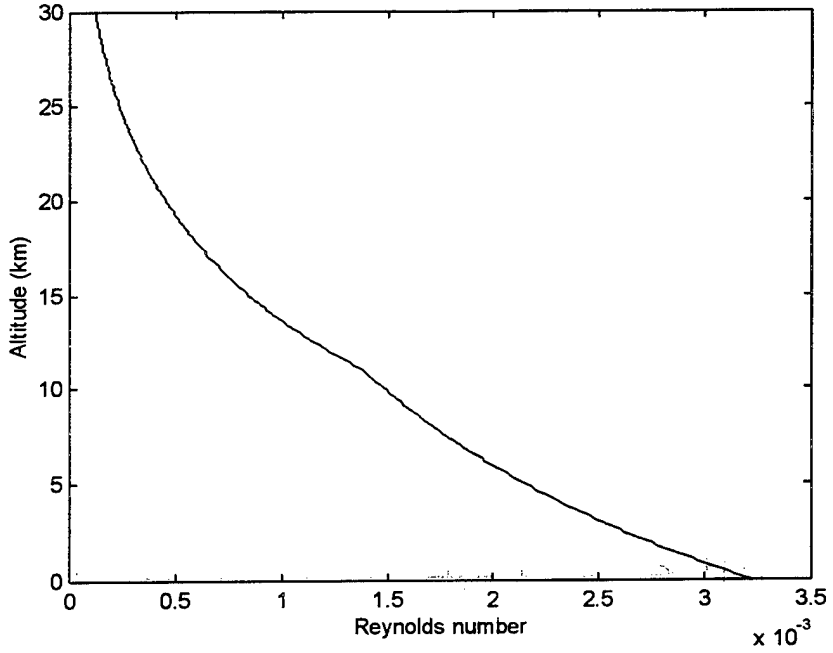

Figure 3-7: Reynolds number versus altitude, for the 4.7 μm probe, for an air velocity of 0.01 m/s.

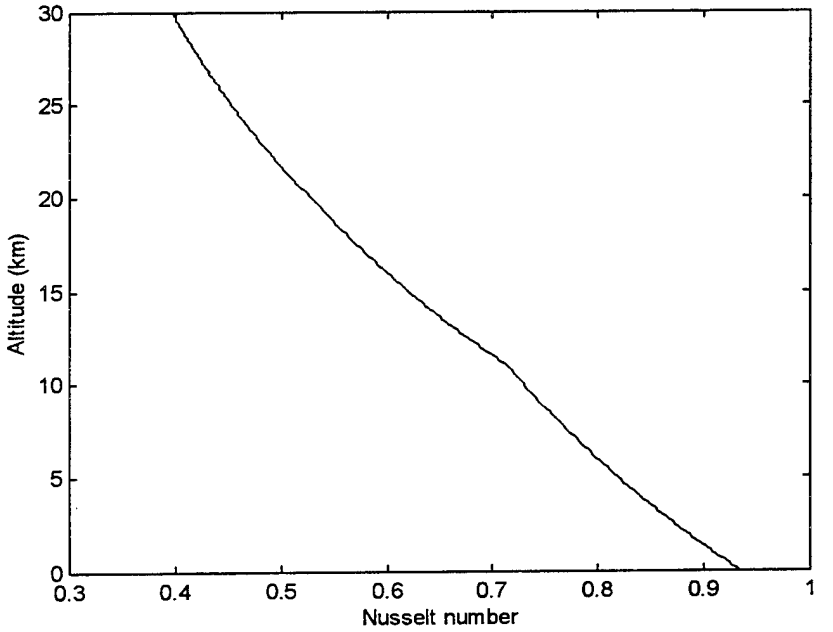

Figure 3-8: Nusselt number versus altitude, for the 4.7 μm probe, for a constant free stream velocity of 5 m/s.

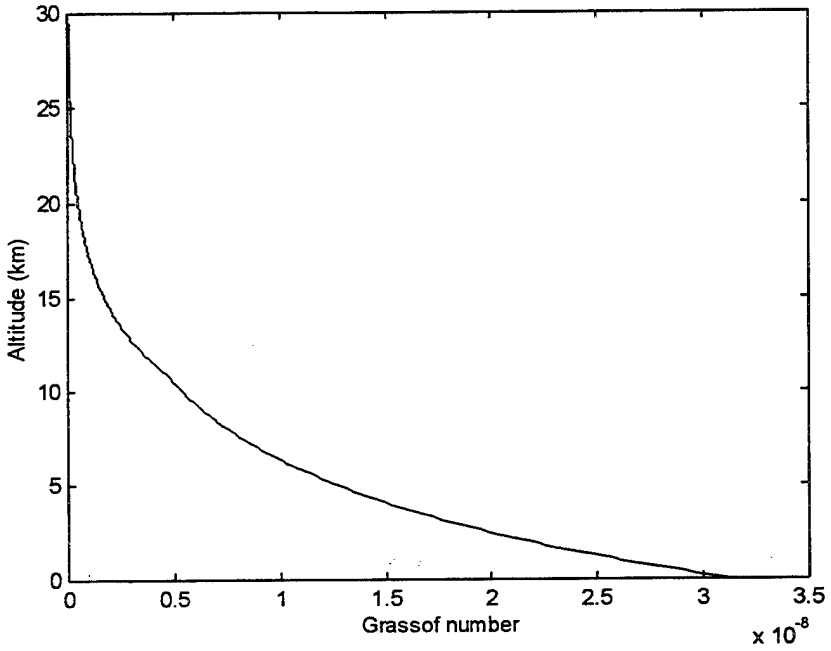

Figure 3-9: Grassof number, showing ratio of buoyancy to viscous forces, versus altitude for constant free stream velocity of 5 m/s and corresponding to a differential probe temperature of 0.035 K for the 4.7 μm probe.

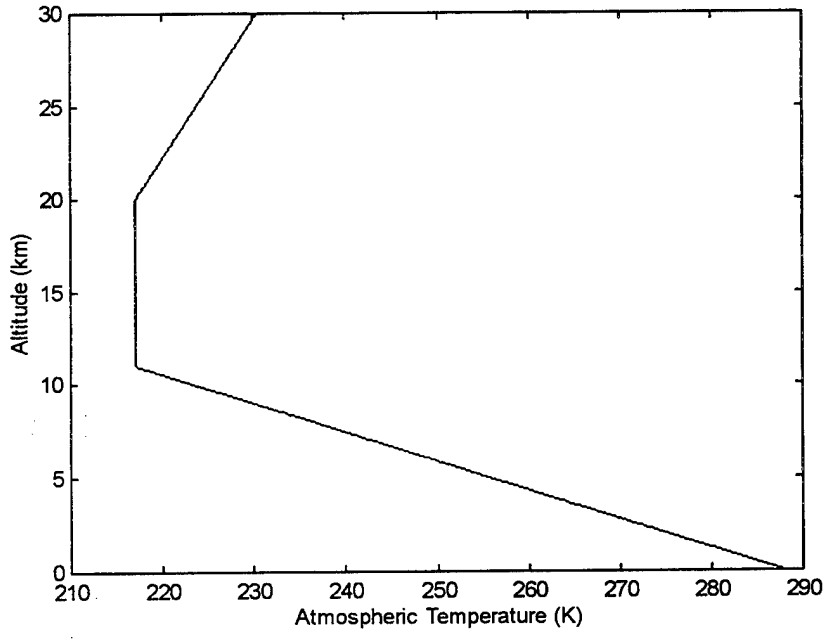

Figure 3-10: Atmospheric temperature versus altitude.

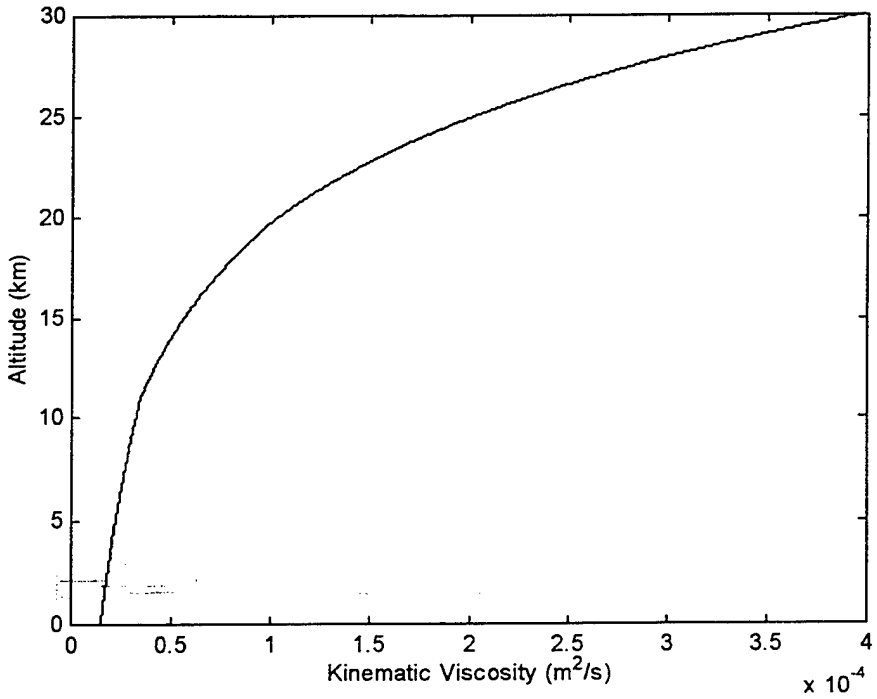

Figure 3-11: Kinematic viscosity of the atmosphere versus altitude.

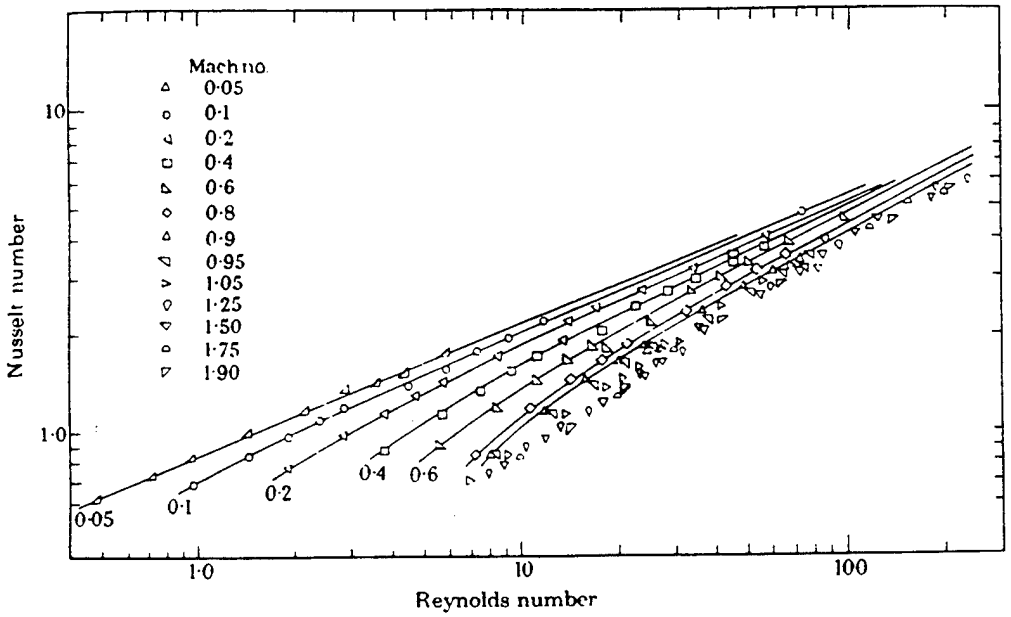

Figure 3-12: Heat loss at increasing Mach number, from Davies and Fischer in [Ref. 22:p. 133].

3. Convective Cooling Power

Typical values for the convective cooling of the wire at sea level are on the order of 10.63×10^{-6} W, but they are sensitive to the free stream velocity. Shown as a function of altitude in Figure 3-13 are values of Q_{conv} for a free stream velocity of 5m/s.

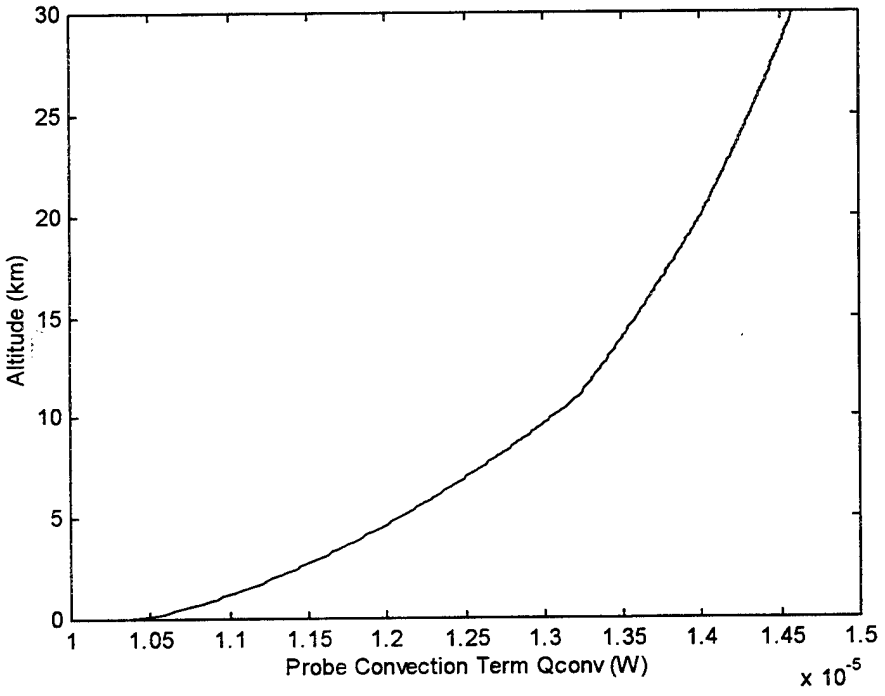

Figure 3-13: Probe convection, Q_{conv} versus altitude (V = 5 m/s)

4. Convection with Normal Free Stream Velocity Fluctuation

Real world conditions encountered by the probe involve dynamic fluctuations of the free stream velocity component over the probe wire. These fluctuations arise from package pendulum motion, rotation, possible balloon wake turbulence, actual atmospheric turbulence, and to a lesser extent probe vibration.

Velocity fluctuations ultimately affect the coefficient of heat transfer and Reynolds number which both depend on air velocity over the probe wire. The effect of a random normal mean free stream velocity fluctuation of 2 m/s about 5 m/s is shown in Figures 3-14 and 3-15 for both these quantities. The convection, Q_{conv}, term will vary similarly with altitude and is not plotted here.

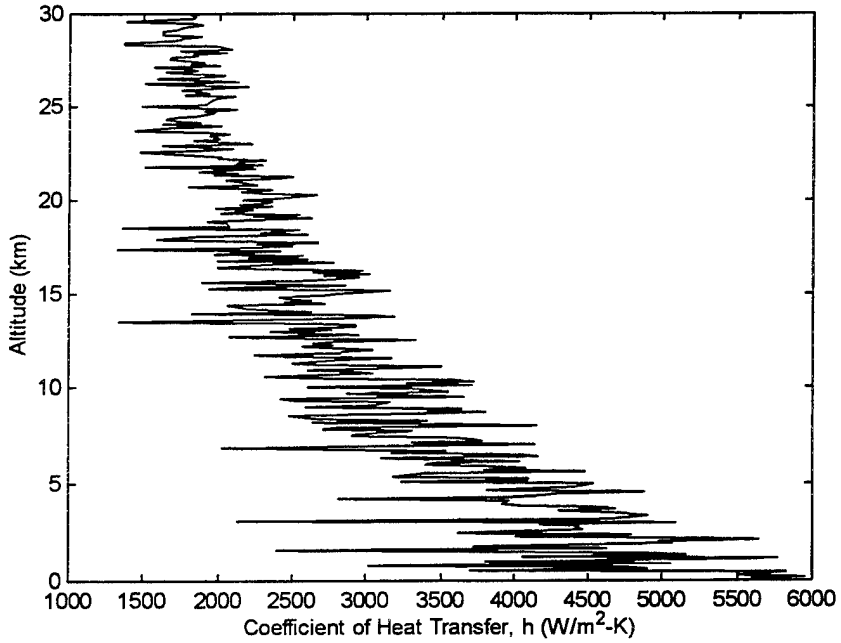

Figure 3-14: Modeled convective heat transfer coefficient with velocity variance of 2 m/s about 5 m/s for the 4.7 μm probe.

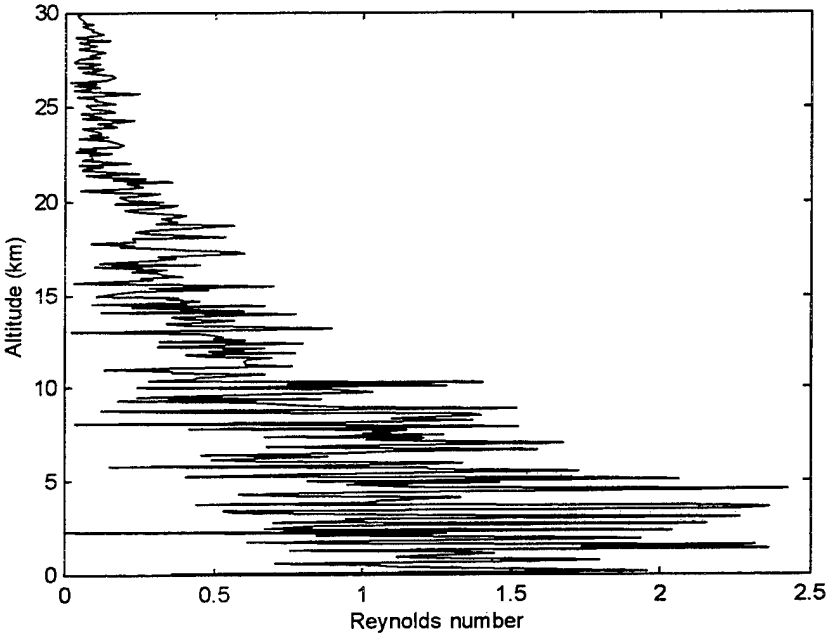

Figure 3-15: Modeled Reynolds number with normal mean velocity variance of 2 m/s about 5 m/s for the 4.7 μm probe.

D. DIRECT SOLAR ABSORPTION OF ENERGY

1. Constant Probe Cross Sectional Area Presented to Solar Radiation

The power absorbed directly from the sun by the probe wire is given by

$$Q_{solar}=\alpha A_2 P_s, \tag{31}$$

in the heat balance equation with:

α= solar absorptivity of the probe,
A_2= cross sectional area of probe seen by the sun (m^2),
P_s= solar power flux (W/m^2).

The solar absorptivity of the platinum coated tungsten wire probe is 0.435 from tabulated values of the normal incident reflectivity (R=0.565 @ 3.0eV) for platinum wire, which is related to the absorptivity by α=1-R [Ref. 28:p. 10-282]. The maximum illuminated area of the probe as seen by the sun to good approximation is the cross sectional area DL. The projected area, A_2, is a function of the complex probe pendulum motion and rotation, probe vibration, and solar zenith angle. The change in area subjected to solar radiation, as a function of time, was modeled as one half the magnitude of the sum of two sinusoidal variations of the total visible surface area. Periods for the two sine functions correspond to the observed frequency of pendulum motion and rotation. Theta dependence (sun zenith angle) was not modeled explicitly in this thesis but was done previously [Ref. 5:p. 10].

The solar flux, P_s, varies with altitude (meters) as given in [Ref. 25]

$$P_s = (Alt)^{0.584} + 890, \tag{32}$$

to our maximum altitude of interest, 30 km.

Typical values of the power absorbed directly from the sun by the probe at sea level are of the order 7.28×10^{-6} W and are shown as a function of altitude in Figure 3-16.

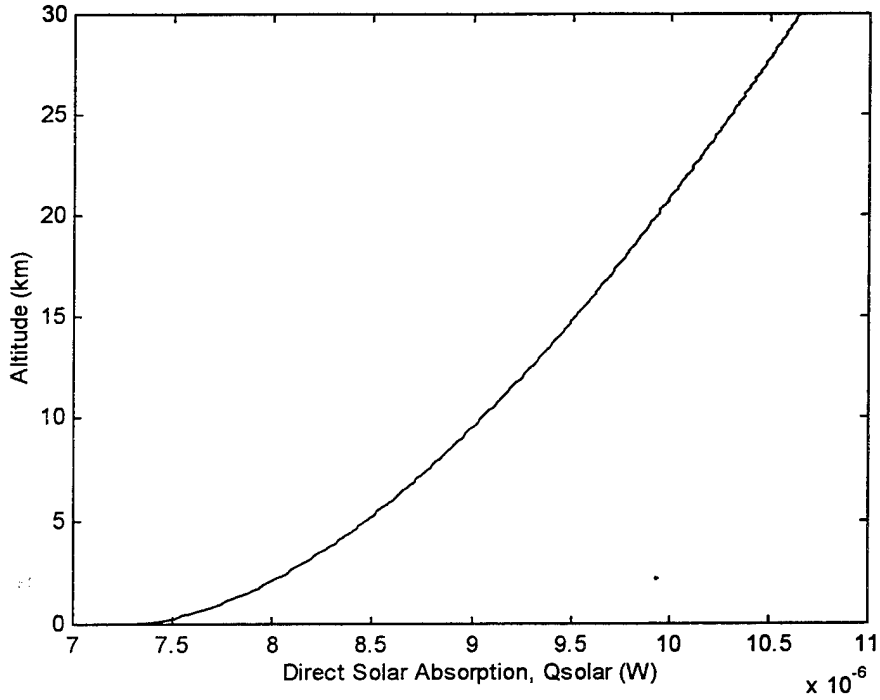

Figure 3-16: Direct solar absorption, Q_{solar}, of power with constant exposed cross sectional area versus altitude for the 4.7 μm probe.

2. Variation of Probe Cross Sectional Area Presented to Solar Radiation

The probe cross sectional area exposed to solar illumination is a function of the roughly sinusoidal geometry variations caused by pendulum motion and rotation with respect to the sun. Secondary influences of probe wire vibration are discussed below. Using MATLAB programs developed by Walters (Appendix C), digital filters and Fourier spectral techniques were used to analyze single probe thermistor data taken at Anderson Peak in September 1992. This launch was during the day and showed the characteristic C_n^2 enhancement obtained from higher order structure functions (Figure 3-17). Figure 3-18 shows the resultant power spectrum plot with two distinct periodicities of about 5 and 20 seconds. Visual observation of these balloon launches and simple calculation of the pendulum motion confirm that these correspond to the periods of the rotational and pendulum motion of the sonde package during its ascent. Hence these were used in our

model. The influence of the sinusoidal variation of the solar cross sectional area A_2 on solar absorption Q_{solar} is shown in Figure 3-19.

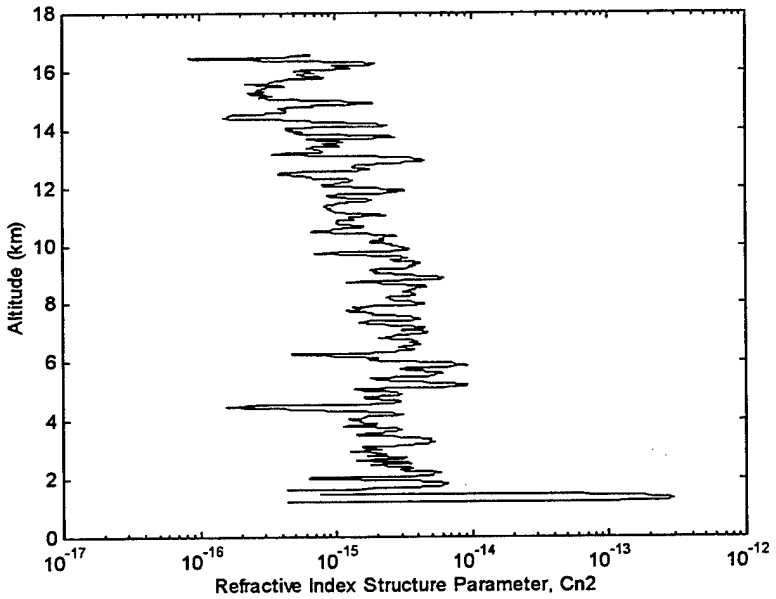

Figure 3-17: Anderson Peak C_n^2 during the day obtained from a single flake thermistor.

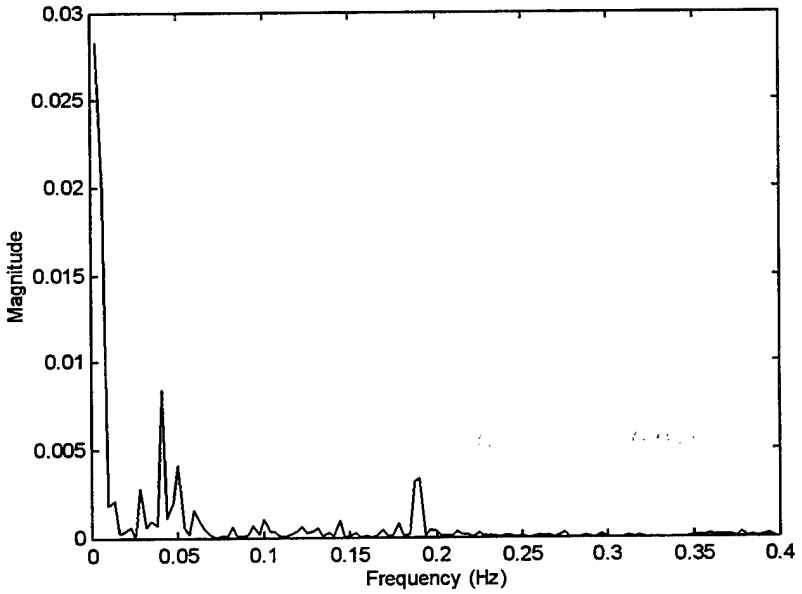

Figure 3-18: Power spectral plot of Anderson Peak data from Figure 3-17.

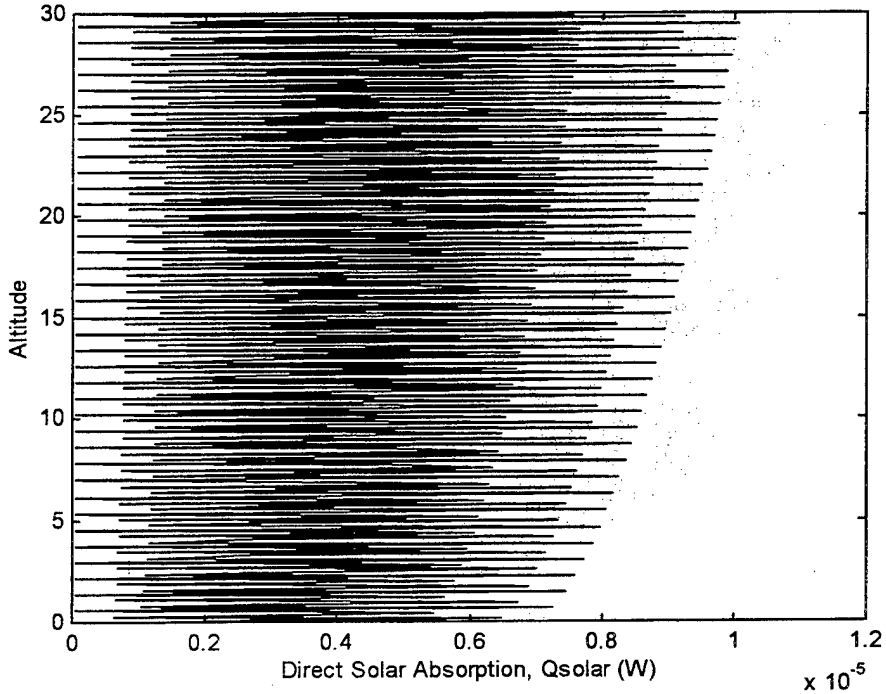

Figure 3-19: Effect of Sinusoidal variation of probe solar illumination area, A_2 on solar heat flux with air velocity of 5 m/s for the 4.7 μm probe.

3. Probe Vibration

Less well understood is the effect on solar heating caused by the probe wire vibrating in and out of solar view. Experimental work done to measure this phenomenon is discussed further in Chapter IV.

E. REFLECTED SOLAR ABSORPTION

The reflected solar power from the Earth onto the probe wire is given by

$$Q_{refl}=\alpha A_4 P_s \gamma, \tag{33}$$

where:

α= solar absorptivity of the probe,
A_4 = effective area of the probe that absorbes reflected sunlight (m^2),
P_s= solar energy flux (W/m^2),
γ= percent of solar energy reflected by the Earth (terrestrial albedo)

The solar absorptivity and solar flux terms are as previously determined. Solar flux is taken to be a fraction of that at the surface of the Earth (890 W/m^2). The maximum cross sectional area of the probe seen by the earth is DL. The percent of solar power reflected by the Earth (albedo) was estimated to be 39%.

Typical values of the reflected power of the sun from the Earth on the probe are of the order 2.84×10^{-6} W at sea level and are approximately constant with altitude.

F. PLANCK RADIATION

1. Planck Radiation from the Atmosphere

Planck radiation consists of three terms, that being absorption from the surrounding atmosphere, that being absorbed from the Earth, and that being radiated away by the probe. It is represented by

$$Q_{planck}=q_A+q_E-q_P. \tag{34}$$

Energy transfer in the form of Planck radiation from the atmosphere to the probe is

$$q_A=\varepsilon A_6 P_{atm}, \tag{35}$$

where:

ε= emissivity (0.065),
A_6= area of the probe presented to the atmosphere (m^2),
P_{atm}= thermal radiation emitted from the atmosphere (W/m^2).

The emissivity term is taken as a constant and given the value of that for 300 K radiation. The area A_6 is the total probe surface area. The radiation term P_{atm} was estimated by integrating over the plot of radiance versus wavelength for sky radiation as seen from the Earth, given in [Ref. 29:p. 3-75]. For a first order approximation the atmospheric flux on a sunlit summer day at 30°-40° latitude with an estimated probe field of view of 4π steradians was used. An approximate value for P_{atm} of 250 W/m^2 resulted.

Typical values of radiation from the surrounding atmosphere on the probe are of the order 9.6×10^{-7} W at sea level and are constant as a function of altitude. P_{atm} is more correctly a function of the air temperature and therefore would vary with altitude, but these effects are small and were neglected in this work..

2. Planck Radiation from Earth

Planck radiation from the Earth is given by

$$q_E = \varepsilon A_5 P_e, \tag{36}$$

with:

ε= emissivity for 300K radiation,
A_5= area of probe presented to earth (m^2),
P_e= radiation from Earth (W/m^2).

Emissivity is as before and A_5 is equal to the cross sectional area DL. The Earth-radiated flux was estimated using the same integration approximation technique as used for P_{atm} above but now integrating over the upper portion of the radiance versus wavelength plot of the Earth as seen from space as given in [Ref. 29:p. 3-54]. This integration yielded a first order approximation of the solar flux on a sunlit summer day at 30°-40° latitude with an estimated probe field of view of 2π steradians. An approximate value for P_e of 615 W/m^2 was used.

Typical values of radiation on the probe are of the order 7.5×10^{-7} W at sea level and are constant as a function of altitude.

3. Planck Radiation of the Probe Wire

Planck radiation from the surface of the wire is

$$q_P = \varepsilon \sigma A_3 T^4, \tag{37}$$

where:

ε= emissivity for 300K radiation,
σ= Stefan-Boltzman constant (5.67×10^{-8} W/m^2K^4),
A_3= area of the wire probe radiating (m^2),
T= atmospheric temperature (K).

The emissivity for platinum wire was 0.065 [Ref. 28:p. 10-282]. The area term, A_3, is the total surface area of the probe. The atmospheric temperature is used instead of the probe temperature T_{probe} to simplify the calculation and because $\Delta T << T_{probe}$ as shown in [Ref. 5:p. 4].

Typical values of the Planck radiation emitted by the probe are of the order 1.50×10^{-6} W at sea level and are shown as a function of altitude in Figure 3-20.

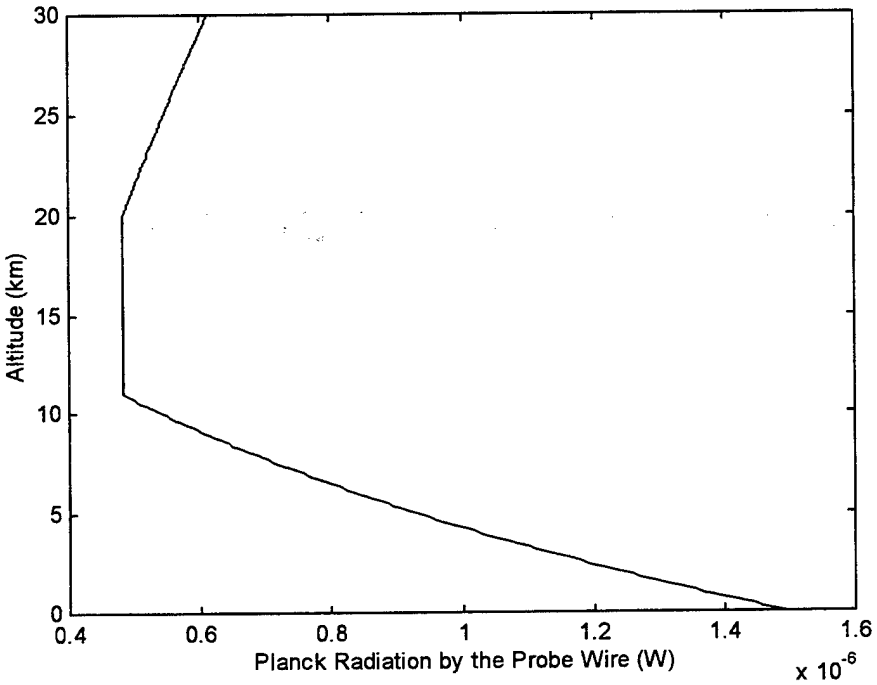

Figure 3-20: Planck radiation from the 4.7 μm probe as a function of altitude with constant air velocity of 5 m/s.

G. OHMIC HEATING OF THE PROBE WIRE

Probe wire heating due to the current through the wire is

$$Q_{Ohmic} = I^2 R, \tag{38}$$

where I is the current through the probe and R is the probe's resistance. Brown in [Ref. 14] measured this quantity to be 3.3×10^{-7} W at the small currents used in this type of probe, and we adopted his value for all of our modeling.

H. PROBE TEMPERATURE

1. Steady State Free Stream Velocity

Solving the equilibrium equation for T_{Probe} , using Eq. (15), the difference in probe temperature and atmospheric temperature ΔT versus altitude is shown in Figure 3-21.

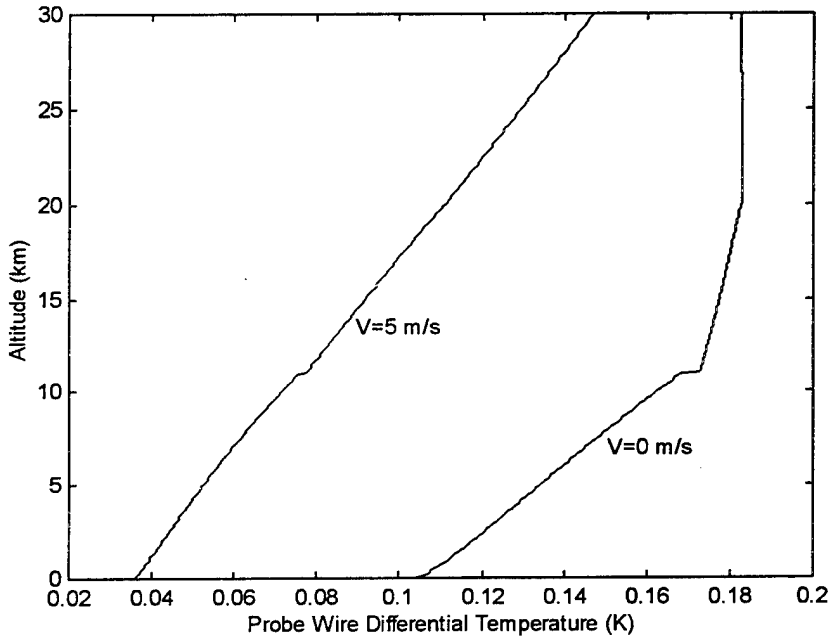

Figure 3-21 : Differential probe temperature versus altitude with constant free stream velocity of 0 and 5 m/s with all probe areas constant at their maximum value for a 4.7 μm platinum coated tungsten probe.

2. Normal Free Stream Velocity Fluctuations

As the sonde rises, balloon pendulum motion and rotation occur. With the combined vertical horizontal and rotational velocity it is possible for the relative wind speed on the probe to drop to low values. The transient zero velocity condition is of interest in our model because forced convective heat transfer would approach zero. Near zero air velocity, convection would be much smaller allowing the solar flux to dominate probe heating and increasing ΔT . In practice, though, free convection will create an induced effective

velocity over the probe wire, due to density differences near the wire so flow velocities will only approach zero.

Figure 3-22 represents the effects of velocity fluctuations on the differential temperature as a function of altitude.

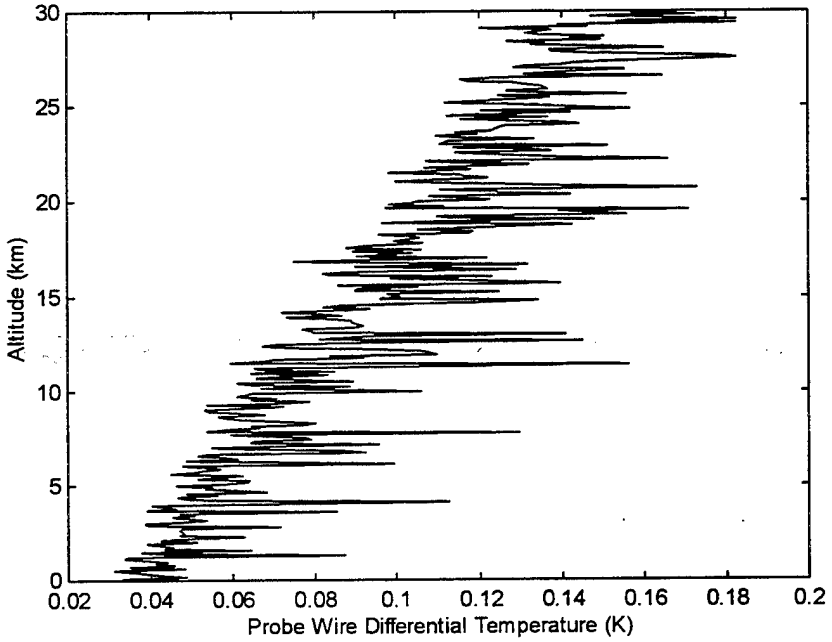

Figure 3-22: Simulated probe differential temperature for a normal velocity fluctuation of 2.5 m/s about a velocity of 5m/s versus altitude for the 4.7 μm probe.

3. Variation of Solar Illumination Area

The effect on the differential probe temperature of varying the probe's orientation with respect to the sun is shown in Figure 3-23 for sinusoidal change of area A_2 as a function of differential temperature and with constant altitude.

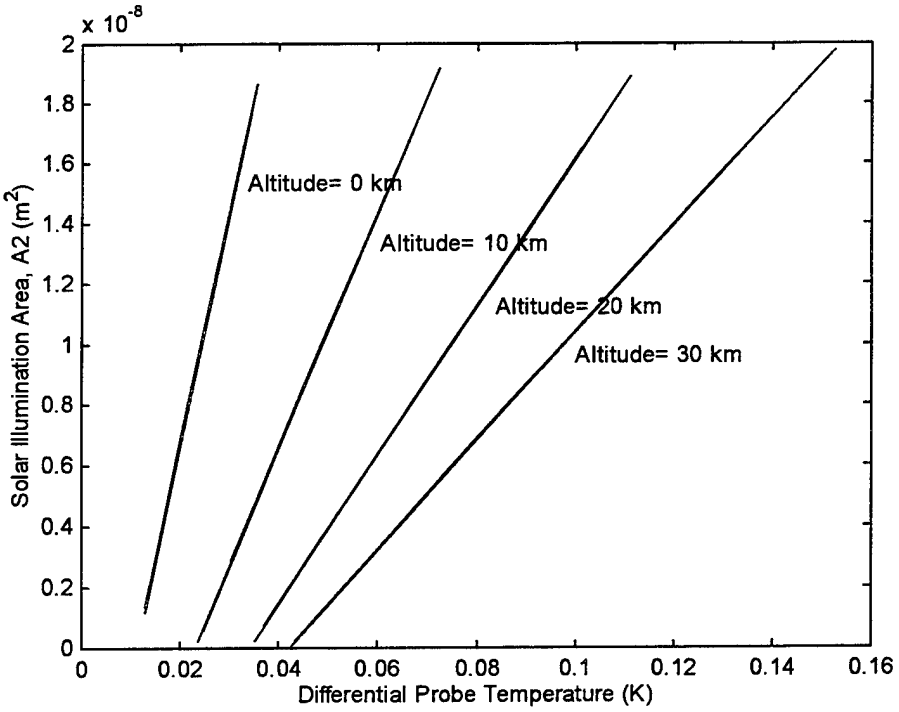

Figure 3-23: Effect of varying the solar illumination area, A_2, on the 4.7 μm probe differential temperature with constant altitude and air velocity (5 m/s).

4. Probe Orientation with Respect to the Earth

By sinusoidal variation of the area terms A_4 and A_5 with periods of 5 and 20 seconds, the effect of relative Earth-probe orientations on the probe differential temperature for constant altitude and air velocity (5 m/s) may be calculated. Examples are shown in Figure 3-24.

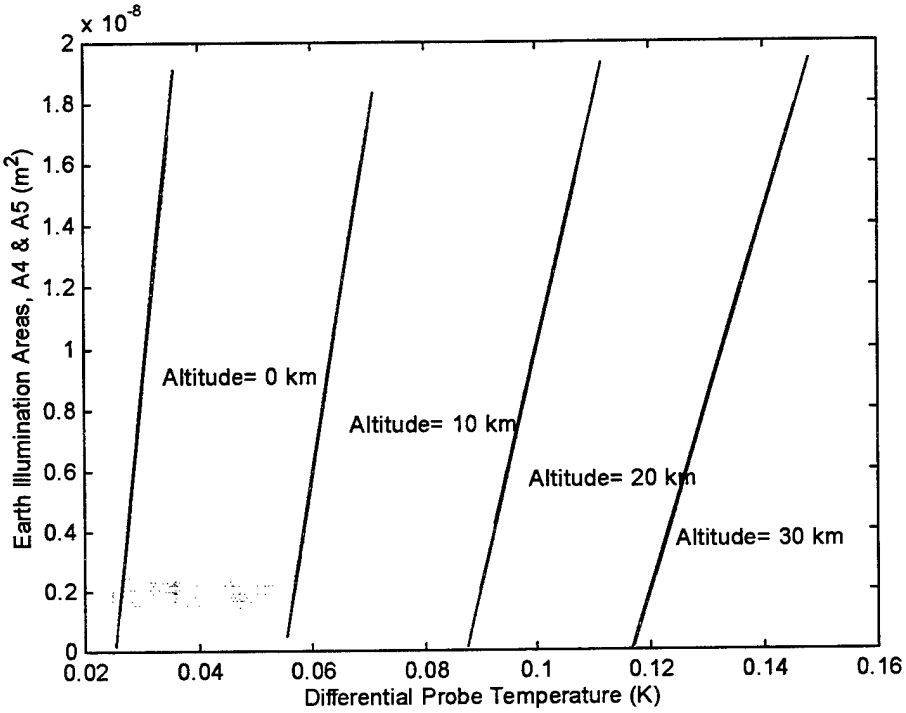

Figure 3-24: Effect of sinusoidal variation of Earth illuminated probe areas A_4 and A_5, (i.e., reflected solar radiation and Planck radiation from Earth) on the 4.7 μm probe differential temperature with constant altitude and air velocity (5 m/s).

I. SUMMARY

Relative energy contributions to the heat flux of the platinum coated tungsten wire are ranked by order of magnitude, and hence contribution to probe temperature, in Table 3-3 for an air velocity of 5 m/s at sea level. Probe convection and direct solar radiation terms dominate, with convection being strongly dependent on free stream air velocity. Solar radiation effects are strongly dependent upon probe orientation.

Fluctuations in the free stream air velocity over the probe can produce a maximum change in probe differential temperature of 0.1 K at 10 km.

Direct solar radiation loading alone accounts for a maximum probe temperature change of approximately 0.111 K with constant free stream velocity, V=5 m/s at sea level. This change is a consequence only of a change in probe solar illumination area A_2.

Variation of the probe cross sectional areas presented to Earth (A_4 and A_5) results in a maximum of 0.028 K variation of probe temperature with constant free stream velocity of V=5 m/s at 30 km.

Table 3-4 summarizes the maximum and minimum variation of the probe differential temperature as a function of free stream air velocity, probe solar illumination area, and probe Earth illuminated areas.

Heat Transfer Mechanism	**Power (μW)**
Convection	-10.63
Direct Solar Illumination	7.28
Earth Reflected Illumination	2.84
Probe Planck Radiation	-1.50
Atmospheric Planck Radiation	0.96
Earth Planck Radiation	0.75
Ohmic Heating	0.30

Table 3-3: Typical values for energy transfer mechanisms involved in the AFRL 4.7μm platinum coated tungsten probe wire at constant air velocity of 5 m/s at sea level with maximum wire areas illuminated.

Parameter Varied	**Maximum Change in T (K)**	**Altitude (km)**	**Minimum Change in T (K)**	**Altitude (km)**
Free Stream Velocity Variation about 5 m/s (2.5σ)	0.1	10	0.036	30
Solar Illumination Area, A_2	0.111	30	0.024	0
Earth Visible Areas, A_4, A_5	0.028	30	0.011	0

Table 3-4: Maximum and Minimum change in values for the AFRL 4.7 μm probe differential temperature for given parameter variation.

IV. EXPERIMENTAL MEASUREMENTS

A. PROBE TEMPERATURE SENSITIVITY CHARACTERISTICS

1. Purpose

Verification of the actual probe response characteristics when subjected to solar radiation and varying wind speeds was done experimentally to validate probe modeling of the solar and convective heat transfer mechanisms. In this experiment we measured the differential temperature of the probe in response to one solar flux of radiation as a function of wind speed. The effect of Earth reflected sunlight at zero wind speed on the probe was also approximated experimentally.

2. Experimental Procedure

The platinum coated tungsten probe was mounted in a wind tunnel with air flow perpendicular to the wire (Figure 4-1). A Radiac ELH 300 W tungsten halogen lamp was focused uniformly on the probe through an optical lens, and the lamp power was adjusted to correspond to one solar flux after being chopped with a Laser Precision Corporation CTX-534 Radiation Chopper. Calibration of our unit solar flux source was done by direct comparison with the Sun at local solar noon on a clear day at latitude 40N, as measured by a United Detector Technologies model 255 silicon photodetector. A uniform spectral response measurement was made with a Scientec 362 Thermopile Power Energy meter to cross check the spectral response of the photodetector. To the accuracy of our measurements (about 1%), the halogen lamp flux and the solar spectral flux produced the same probe heating with both the silicon and broadband detectors. The signal was passed through a Stanford Research Systems SR560 Low-Noise Preamplifier and voltage readings were then taken using a Hewlett-Packard 3561A Dynamic Signal Analyzer and Nicolet Pro 30 digital oscilloscope for wind speeds from 0 to 6.0 m/s. Wind velocities were

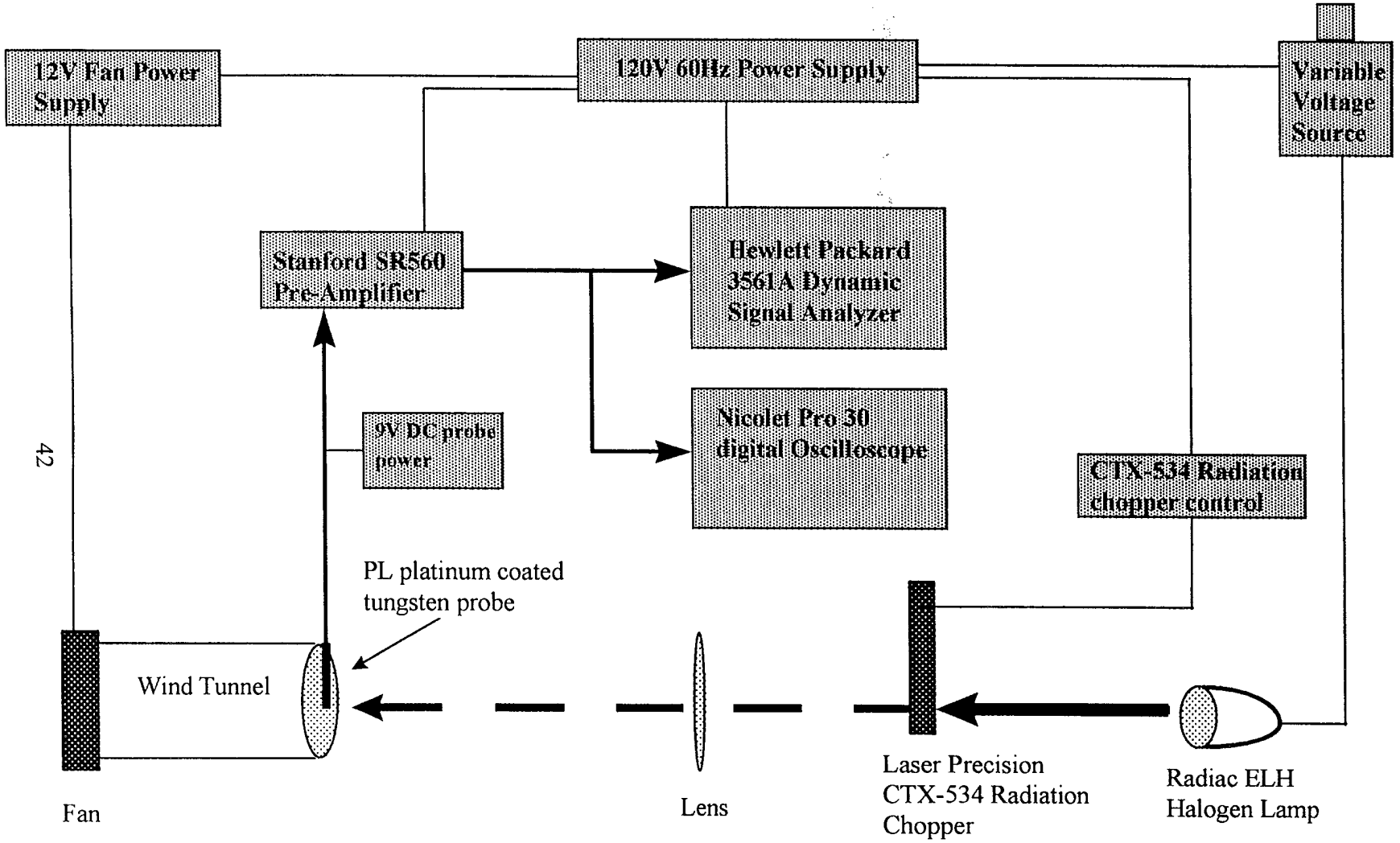

Figure 4-1: Laboratory bench setup for measurement of PL probe differential temperature.

measured using an Omega HHF 52 hot wire anemometer accurate to 0.1 m/s. Three separate experiments were conducted on 24-25 April, 16 May, and 29 May 1997 using three different platinum coated tungsten probes. Probes #1 and #2 were from similar batches of platinum coated tungsten wire while Probe #3 was a much older (1989) probe from a separate production run of wire obtained from the Air Force Geophysics Directorate.

The effect of Earth reflected sunlight was measured using a 41% reflective gray surface behind the probe. The reflected sunlight measurements were made at zero wind speed.

3. Results

Experimental results are tabulated in Tables 4-1 to 4-5. The rms voltages read from the HP-3561A spectrum analyzer were converted to peak-to-peak voltages by multiplying by a factor of $2\sqrt{2}$ and dividing by the gain applied at the SR560 preamplifier, since the wave form of the chopped light was nearly sinusoidal. For the second experiment (16 May 97) this procedure was modified slightly to include a correction factor, of 2.22, to account for an observed non-square, chopped wave form from the halogen lamp source. The probe differential temperature was obtained by solving for ΔT in the equation for probe resistance [Ref. 13:p. 11]

$$R_W = R_0(1+\alpha\Delta T), \tag{39}$$

where R_0 is the cold reference probe resistance. A different probe was used in each experiment so this value was measured as 19.94 Ω (24-25 April 97), 18.81 Ω (17 May 97), and 25.68 Ω (29 May 97). The constant alpha was assumed to be α=0.0042 for platinum coated tungsten wire [Ref. 30].

An upward drift in measured voltages was noted after continual illumination of about 60 s or more. We suspect that this was most probably due to probe support heating effects as shown in Ref. 5:p. 16. Severe direct thermal contamination was noted with the halogen lamp closer than about 0.5 m, obviating the use of a lens to separate the hot lamp from the wind tunnel.

The observed temperature change depended on the chopping frequency and the probe response time. The probe response time varied between 0.6 to 2 ms and acted like a one pole low-pass filter at these frequencies. Collecting measurements at low frequencies, on the order of 5 Hz, was not always possible because of interference from ambient turbulence. In these cases higher frequencies around 25 Hz were used after including a correction factor.

Probe #3 showed a lower probe differential temperature (Table 4-4) than Probes #1 and #2. Possible explanations for this discrepancy are investigated in Chapter V.

Air Velocity (m/s)	Measured Voltage hp 3561A (mV- rms)	Peak-to-Peak Voltage - (mV)	Actual Voltage (μV)	ΔR (mΩ)	Differential Temperature (K) [Corrected]
0	129.0	364.9	7.30	7.97	0.095 [0.120]
1.0	114.3	323.3	6.47	7.06	0.085 [0.091]
2.0	96.88	274.0	5.48	5.98	0.071
3.0	82.51	233.4	4.70	5.13	0.061
4.0	79.70	225.4	4.50	4.91	0.059
5.0	74.50	210.7	4.20	4.58	0.055
6.0	67.00	189.5	3.79	4.14	0.049

Table 4-1: Experimental probe differential temperature measurements of Probe #1 (new) for one solar flux from a halogen lamp using a chopping frequency of 50 Hz and corrected temperatures for 0 and 1 m/s air velocity measurements (19 April 1997).

Air Velocity (m/s)	Measured Voltage hp 3561A (mV- rms)	Peak-to-Peak Voltage - (mV)	Actual Voltage (μV)	ΔR (mΩ)	Differential Temperature (K) [Corrected]
0	128.1	362.3	7.3	7.9	0.095 [0.120]
1.0	114.2	323.0	6.5	7.1	0.084 [0.090]
2.0	98.6	278.9	5.6	6.1	0.073
3.0	88.6	250.5	5.0	5.5	0.065
4.0	81.5	230.5	4.6	5.0	0.060
5.0	76.8	217.3	4.4	4.8	0.057
5.5	73.8	208.7	4.2	4.6	0.054

Table 4-2: Experimental probe differential temperature measurements of Probe #1 (new) for one solar flux from a halogen lamp using a chopping frequency of 25 Hz and corrected temperatures for 0 and 1 m/s air velocity measurements (24 April 1997).

Air Velocity (m/s)	Measured Voltage Nicolet Pro 30 (mV- rms)	Actual Voltage (μV)	ΔR (mΩ)	Differential Temperature (K)
0	40.69	9.19	10.27	0.130
1.0	25.85	5.84	6.52	0.083
2.0	20.82	4.70	5.03	0.067
3.0	18.56	4.19	4.68	0.059
4.0	16.93	3.82	4.27	0.054

Table 4-3: Experimental probe differential temperature measurements of Probe #2 (new) for one solar flux from a halogen lamp using a chopping frequency of 5 Hz (16 May 1997).

Air Velocity (m/s)	Measured Voltage Nicolet 3091 (mV- rms)	Actual Voltage (μV)	ΔR (mΩ)	Differential Temperature (K)
0	37.2	8.26	9.19	0.085
1.0	24.9	5.53	6.15	0.057
2.0	20.3	4.51	5.02	0.047
3.0	17.6	3.91	4.35	0.040
4.0	16.0	3.55	3.95	0.037
5.0	15.0	3.34	3.71	0.034

Table 4-4: Experimental probe differential temperature measurements for Probe #3 (1991-3.8 μm) one solar flux from a halogen lamp using a chopping frequency of 10 Hz (29 May 1997).

Air Velocity (m/s)	25 Hz, Measured Voltage (mV)	5 Hz, Measured Voltage (mV)	Correction Factor
0	32.14	40.25	1.252
1	24.79	26.59	1.073

Table 4-5: Correction factor for low air velocity and higher frequency chopping rates.

Adding a gray cardboard background for reflection of the halogen lamp provided the probe with a 2π steradian solid angle reflective background surface which roughly simulated that of the Earth. Table 4-6 shows the increased signal differences due to "Earth reflected solar radiation" from the absence of a reflective surface, gray cardboard, reference (white) surface, and a first surface mirror.

Background (reflectivity)	Measured Voltage - HP 3561A (mV- rms)	Percent Change (%)
None (0%)	34.9	0
Gray (~41%)	43.0	19
White (~100%)	60.0	42
First Surface Mirror (~100%)	60.8	43

Table 4-6: Experimental data for the effect of reflective backgrounds on differential probe temperature of Probe #2 (new) with one solar flux of direct radiation at zero air velocity, sea level, and chopping frequency of 5 Hz (29 May 1997).

Sources of error for this experiment include the signal lost due to the high chopping rate in the earlier data. This is partly resolved with the correction factor in Table 4-5. Other minor sources of error involve probe support heating effects, inaccuracy in wind velocity measurements, and assumptions that the halogen lamp accurately reflects the spectral output of the sun.

4. Summary

At sea level, with no forced air flow over the probe, radiation heating countered by free convection and Planck radiation caused probe heating about 0.130 K above ambient temperature. This differential temperature decreased as forced air flow over the probe effected more efficient forced convection cooling to about 0.055 K at 5.0 m/s.

Earth reflected solar radiation contributed an additional 19% increase in probe temperature at zero forced air velocity and would be expected to remain independent of air velocity and approximately independent of altitude.

B. MEASUREMENT OF PROBE WIRE RESPONSE TO DIRECT SOLAR RADIATION

1. Purpose

The probe response to direct solar illumination at sea level was measured under natural conditions to detect any additional error sources or procedural omissions in our laboratory measurements and simulations.

2. Experimental Procedure

Using a similar procedure to that described in Section IV-A, above, the platinum coated tungsten probe was subjected to direct solar illumination on the roof of the NPS physics building (Spanagel Hall) at approximately solar noon on a clear day. High background turbulence forced the use of a spectrum analyzer with chopping frequencies of 25 Hz (see Figure 4-2) but otherwise the experimental procedure followed that of Section IV-A.

3. Results

The results of this experiment are tabulated in Table 4-7. Multiple data points for each air speed where taken and averaged because of the difficult measurement conditions.

Possible error sources include effects from heated air rising from the rooftop concrete surface. This caused noticeable fluctuations as the fan pulled the hotter turbulent air over the probe. The wind speed on the roof varied from zero to almost 5 m/s. Although the experiment was sheltered from direct wind, some breeze was evident. Ambient atmospheric turbulence made it difficult to collect probe solar illumination data accurately. A chopping frequency of 25 Hz facilitated in this but forced a correction to the results as discussed in the previous section.

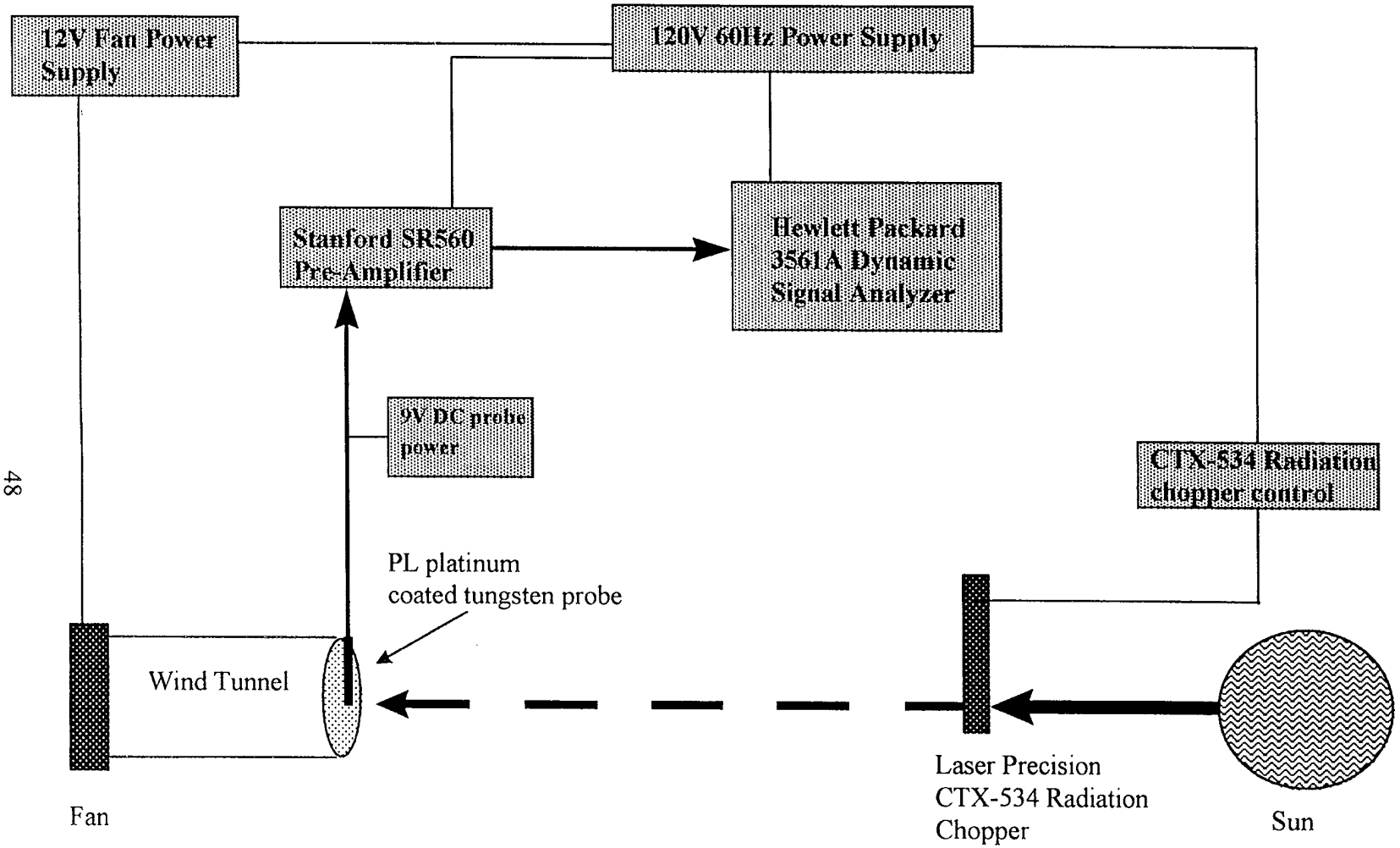

Figure 4-2: Laboratory bench setup for solar measurement of PL probe differential temperature.

4. Summary

Probe temperature rises, as seen in Table 4-7, from direct solar illumination were about 30% lower than those for the laboratory measured halogen illumination, after applying the correction because of the higher chopping frequency. The error was most likely introduced from ambient air flow fluctuations encountered on the rooftop. Considering these corrections and the unsteady air, agreement with experiment was good.

Air Velocity (m/s)	**Measured Voltage (mV)**	**Actual Voltage (μV)**	**R_W (mΩ)**	**ΔT (K)**	**Average ΔT (K) [Corrected]**
0	25.45	5.86	6.54	0.0789	0.0782
	25.40	5.84	6.53	0.0788	
	24.30	5.59	6.25	0.0753	[0.0980]
	25.60	5.89	6.58	0.0794	
1	20.70	4.76	5.33	0.0642	0.0749
	25.80	5.94	6.64	0.0805	
	22.76	5.24	5.86	0.0761	[0.0804]
	25.40	5.85	6.54	0.0788	
2	17.21	3.97	4.43	0.0540	0.0534
	18.03	4.15	4.64	0.0560	
	16.22	3.74	4.17	0.0503	
3	15.97	3.68	4.11	0.0496	0.0462
	13.83	3.19	3.56	0.0429	
	14.18	3.27	3.65	0.0440	
	15.50	3.57	3.99	0.0481	
4	13.43	3.10	3.46	0.0417	0.0430
	13.84	3.19	3.57	0.0430	
	14.27	3.27	3.67	0.0443	
5	10.72	2.47	2.76	0.0332	0.0337
	11.63	2.68	3.00	0.0361	
	10.24	2.36	2.63	0.0318	

Table 4-7: Data from rooftop experiment using a chopping frequency of 25 Hz (16 May 97).

C. MEASUREMENT OF PROBE WIRE VIBRATION EFFECTS

1. Purpose

Historically, error sources in the balloon thermosonde data were thought to result partly from probe wire vibration effects. As air flow over the probe induces vibration in the probe fine wire filament, it would be subjected to periodically varying solar radiation. This vibration, along with the package pendulum motion and rotation, could induce a significant artifact in the data.

2. Experimental Procedure

With the probe mounted in the wind tunnel (Figure 4-3) the behavior of the thin wire filament was investigated with respect to air flow speed and orientational dependence on vibration. Illumination of the probe wire was by a Hughes 7.35mW helium-neon laser beam chopped at 90 Hz. The probe output signal was amplified by a Stanford Research Systems SR560 Low-Noise Preamplifier, passed through a Wavetek Brickwall bandpass filter (model 753A), and read on both a Hewlett-Packard 3561A Dynamic Signal Analyzer and a Tektronix 2236 100 MHz oscilloscope. The bandpass filter was set at 80-100 Hz and the gain was optimized for the signal being read. The probe was also visually monitored using an American Optical microscope placed above the probe but out of the air flow.

Turbulent flow over the wire was induced using a thin rod placed just to one side and upstream of the probe. Reynolds number for the flow over this rod is on the order of Re=1000, which is in the turbulent regime and corresponds to a vortex shedding frequency of 50 Hz from [Ref. 31:p. 15]

$$f_s = \frac{SV}{D}, \tag{40}$$

with S the Strouhal number (S=0.15 in this case), V the free steam velocity, and D the thin rod diameter.

3. Results

Models for flow induced vibration of thin wires developed by Perry in [Ref. 13:p. 99] and Blevins [Ref. 31:p. 15] predict vibration frequencies about two orders of magnitude greater than what were observed visually. Because of the very low Reynolds numbers involved with the platinum coated tungsten wire, the probe wire vibration is most likely due to turbulence in the free stream flow over the wire and not to resonance or vortex shedding effects from the wire itself. As previously shown, the Reynolds number throughout the realm of our model is less than 4 (Figure 3-6 and 3-7), which is under that for separation of flow and turbulence for a circular cylinder which occurs with $Re>5$ [Ref. 21:p. 52]. Observed vibration of the wire was very dependent on the presence of turbulence in the air flow (necessitating the thin rod obstruction) and also showed a marked vibration onset near velocities of 2 m/s with oscillations continuing at nearly constant frequency and magnitude to the limit of our test, 5.8 m/s.

With the probe oriented such that the wire was vibrating in and out of laser illumination, the presence of filament vibration had a noticeable effect on the output signal characteristics as observed on the oscilloscope. Fluctuation about the mean sinusoidal (chopped) output would increase with visible turbulence but was sufficiently random and not of a magnitude that would allow spectral components or harmonics to be noted above the background noise on the Hewlett-Packard signal analyzer.

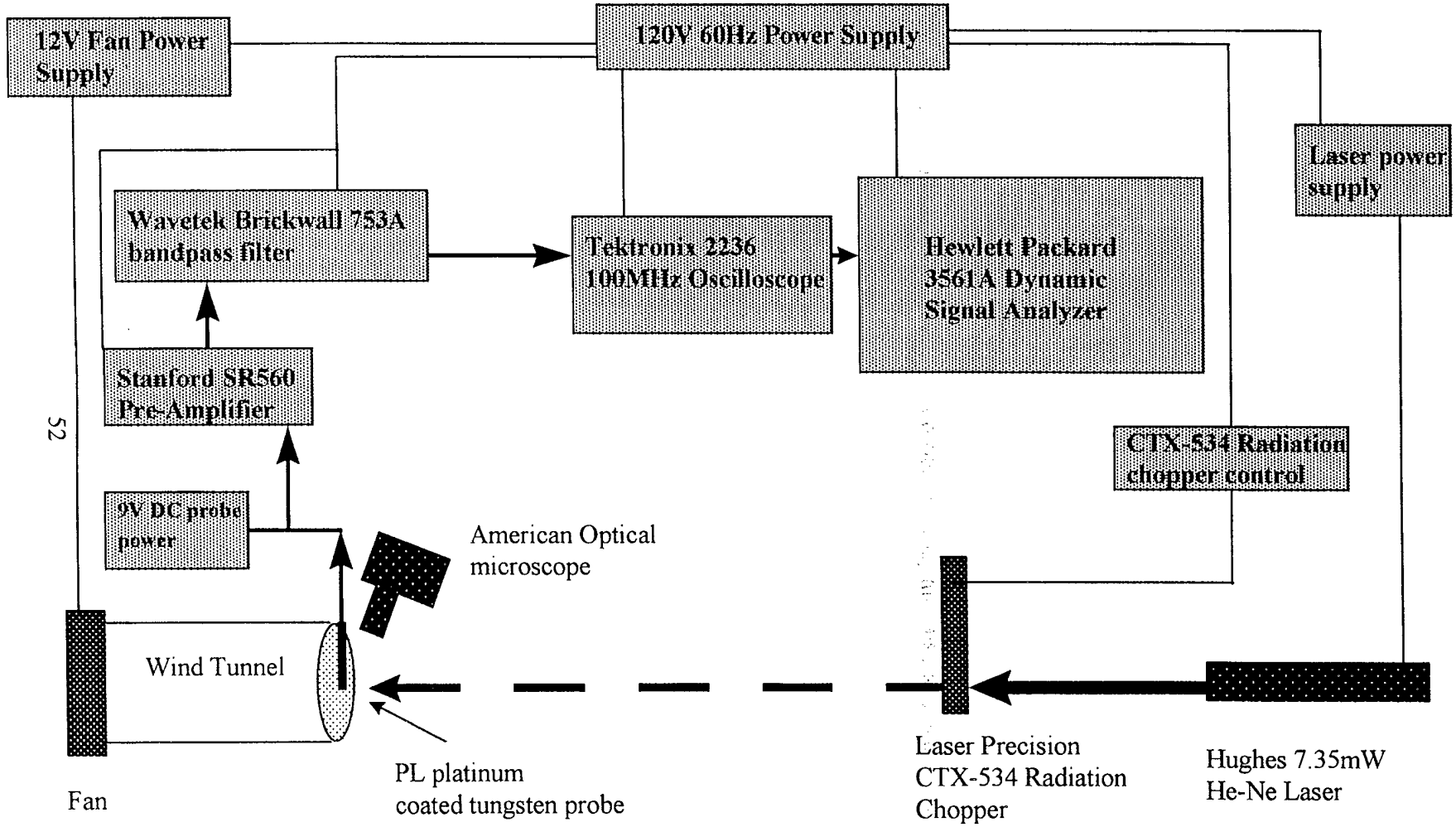

Figure 4-3: Laboratory bench setup for measurement of PL probe vibration effects.

4. Summary

Although the probe wire was noticeably vibrating in and out of the laser beam at a frequency of less than 50 Hz, near that of the thin rod vortex shedding frequency, no appreciable signal could be quantified to the accuracy of our experiment. From this we conclude that probe solar illumination vibration effects are not a significant source of data contamination, although they can occur in the presence of velocity fluctuations in the air flowing over the probe. On the other hand, airflow over the probe will displace the probe wire, since it is not taught. Differential displacement of the probe wires, in a dual probe configuration, will alter the area exposed to the sun. The magnitude of this displacement depends on the drag force, which declines with altitude. This reduction with altitude can produce the pattern seen in Figure 2-5, where the solar induced contamination declines with altitude above 20 km.

D. MEASUREMENT OF COEFFICIENT OF THERMAL CONDUCTIVITY

1. Purpose

Four analytical methods based on experimental data for the modeling of the coefficient of thermal conductivity, h, have been presented in Chapter III. To provide a check of the analytical expressions we chose to independently measure h for our probe. Two experimental methods were used. Atmospheric pressure was varied from sea level to 1 torr, with air velocities over the probe ranging from 0 to 5.8 m/s. Three different probes were measured with tungsten coated platinum wires from two different manufacturing batches. Probes #1 and #2 were purchased new for this work while Probe #3 was previously used in 1991.

2. Experimental Procedure

The platinum coated tungsten probes' response to a square wave input was measured on both a Nicolet Pro 30 and Nicolet 3091 digital oscilloscope (Figure 4-4). Our first method used the heat rate of change equation given in Richards [Ref. 22:p. 87]

$$r\rho\frac{\partial T}{\partial t} = 2h(T_{probe} - T) + rk\frac{\partial^2 T}{\partial x^2} - 2\sigma\varepsilon_w(T^4 - T_0^4), \tag{41}$$

where r is the probe radius, and T_0 is the effective black body temperature of the surroundings. Neglecting the last two terms in Eq. (42) (conduction and radiation terms) the estimated rise time of the probe response is:

$$\tau = \frac{\rho\left(\frac{\pi D^2 L}{4}\right)c}{h(\pi DL)} = \frac{\rho Dc}{4h}, \tag{42}$$

where τ is the rise time, c, is the heat capacity (133 J/kg-K), D is the probe wire diameter (m), and ρ is the density of tungsten (19300 kg/m^3) [Ref. 20,p. 543].

The second technique relied on measurement of the asymptotic temperature rise from Joule heating of the probe wire and the relations:

$$q = \frac{V^2}{R} = I^2 R = hA\Delta T, \tag{43}$$

$$R(T) = R_0(1 + \alpha\Delta T), \text{ and} \tag{44}$$

$$R_{probe} = \frac{V_2 R_1}{V_1 - V_2}. \tag{45}$$

Here V_1 is the voltage applied by the function generator with series resistance R_1, V_2 is the measured voltage output on the oscilloscope, and R_{Probe} is the probe resistance (Figure 4-5).

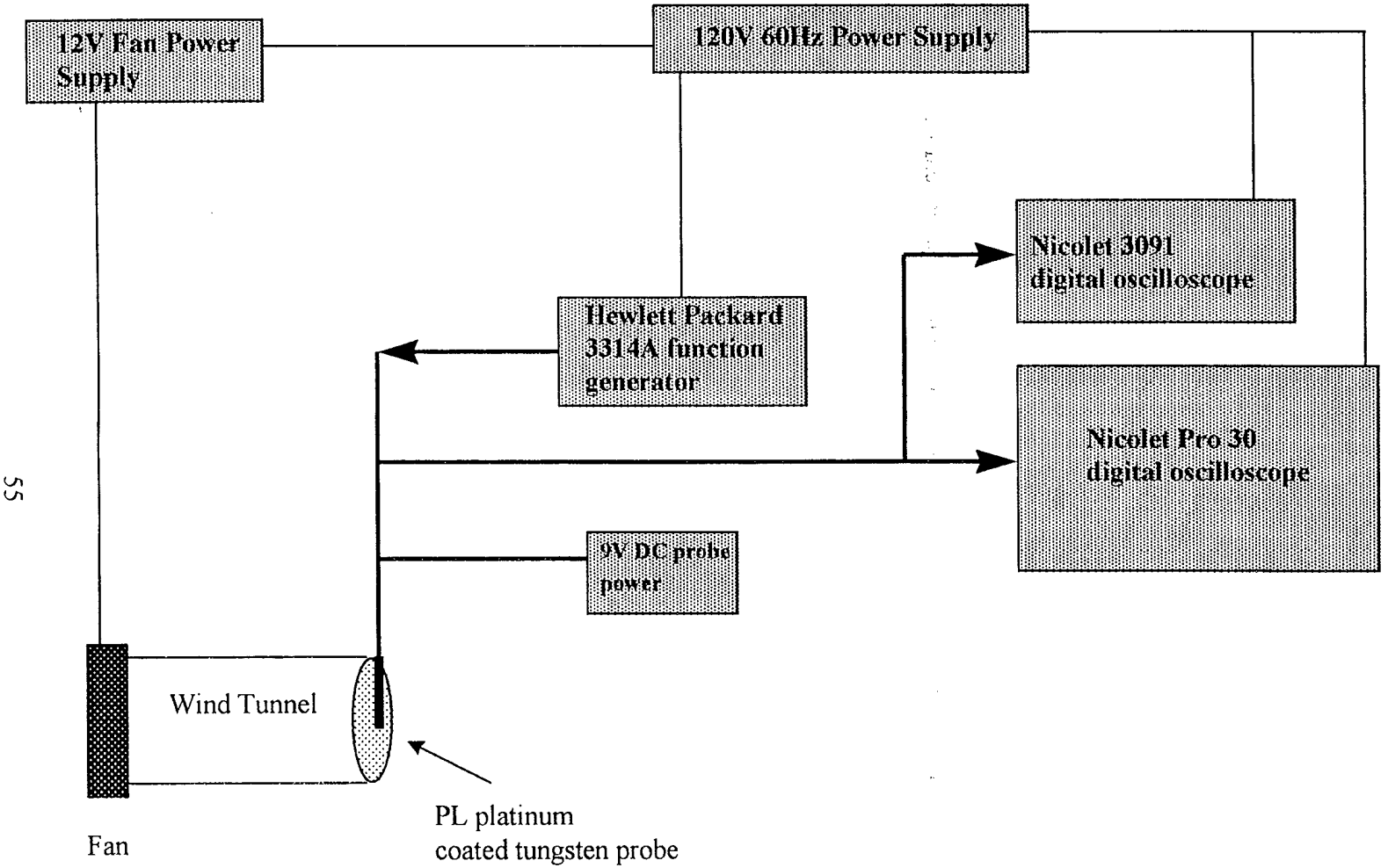

Figure 4-4: Laboratory bench setup for measurement of PL probe coefficient of thermal conductivity, h.

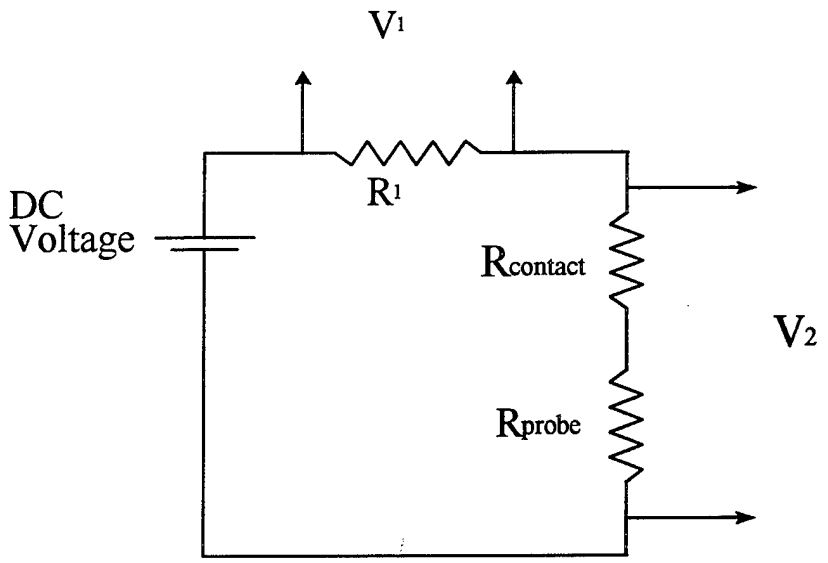

Figure 4-5: Circuitry for the measurement of probe resistance.

Air velocity was varied from 0 to 5.8 m/s for both of the above methods and the minimum voltage possible was used to reduce overheat effects. Conduction effects through the probe wire supports were measured as described in Lomas [Ref. 19:p. 69] by placing the probe in a vacuum and measuring the heat transfer rate to the probe support needles by:

$$q_{probe} = I^2 R. \tag{46}$$

Finally, one probe was subjected to a vacuum under a zero air flow condition and varying pressure as measured with a Vaisala PA 11 digital barometer.

3. Results

The three sets of data are shown in Tables 4-8 to 13. Values for h were calculated using the MATLAB program listed in Appendix D.

Sensitivity to probe overheating was found and is shown in Tables 4-13 and 4-14. This overheat condition was thus minimized as much as was possible when making measurements. The reason for this sensitivity is unknown and is still being investigated.

Contamination of the probe wire through normal use resulted in an increase in the observed probe response time by about 20% over that of a thoroughly cleaned probe. This effect was thought to be negligible and was first discounted as an error source. Perry in [Ref. 13:p. 56] discusses its possible causes and prevention.

Conduction of heat through the probe wire supports was measured to be 0.0015W at an overheat of 53 K, zero wind speed, and a pressure of 0 mBar. This power flow decreases as the square of the input voltage and is therefore very small for our voltages and corresponds to a 2.8×10^{-5} W/K temperature difference between the probe wire and the probe supports.

Air Velocity (m/s)	**V_L (mV)**	**V_U (mV)**	**$V_L+(1-1/e)\Delta V$ (mV)**	**1/e Rise Time (ms)**	**h (W/m^2-K)**
0	448.08	515.8	490.89	1.94	1555
1	442.80	491.2	491.20	1.14	2646
2	443.60	482.4	467.96	0.91	3314
3	442.60	476.6	464.45	0.75	4022
4	442.80	474.0	462.52	0.72	4189
5	442.66	471.2	460.70	0.65	4640
5.8	442.77	469.7	459.82	0.62	4865

Table 4-8: Experimental data for time constant measurement technique of Probe #1 (new) using Nicolet 3091 and varying air velocity(1 May 97).

Air Velocity (m/s)	**V_L (mV)**	**V_U (mV)**	**$V_L+(1-1/e)\Delta V$ (mV)**	**1/e Rise Time (ms)**	**h (W/m^2-K)**
0	362.5	520.2	462.2	2.46	1226
1	359.75	461.75	424.2	1.19	2535
2	360.5	444.5	413.6	0.94	3209
3	360.0	432.0	404.5	0.87	3467
4	360.0	425.5	401.4	0.76	3969
5	359.5	421.5	398.8	0.73	4132

Table 4-9: Experimental Data for time constant measurement technique of Probe #2 (new) using Nicolet 3091 and varying air velocity (14 May 97).

Air Velocity (m/s)	V_L (mV)	V_U (mV)	$V_L+(1-1/e)\Delta V$ (mV)	1/e Rise Time (ms)	h (W/m^2-K)
0	450.4	556.4	517.4	2.32	1063
1	449.8	510.6		0.870	2810
2	449.5	499.2		0.705	3468
3	449.4	492.2		0.596	4102
4	449.6	489.8		0.526	4648
5	449.5	485.8		0.505	4841

Table 4-10: Experimental Data for time constant measurement technique of Probe #3 (1991) using Nicolet 3091 and varying air velocity (29 May 97).

Air Velocity (m/s)	V_L (mV)	V_U (mV)	ΔT (K)	h (W/m^2-K)
0	584.0	731.0	96.7	3184
1	573.8	675.0		4582
2	573.5	658.5		5456
3	573.5	647.5		6267
4	573.5	640.7		6900
5	573.5	637.8		7210
5.8	573.5	633.6	37	7712

Table 4-11: Experimental Data for asymptotic temperature change technique of Probe #1 (new) using Nicolet 3091 and varying air velocity (2 May 97).

Air Velocity (m/s)	V_L (mV)	V_U (mV)	ΔT (K)	h (W/m^2-K)
0	450.4	556.4	46.0	3853
1	449.8	510.6	28.9	5638
2	449.5	499.2	24.1	6584
3	449.4	492.2	21.1	7428
4	449.6	489.8	19.9	7810
5	449.5	485.8	18.0	8574

Table 4-12: Experimental Data for asymptotic temperature change technique of Probe #3 (1991) using Nicolet 3091 and varying air velocity (29 May 97).

Pressure (mb) @ Input voltage (V)	V_L (mV)	V_U (mV)	ΔT (K)	h (W/m^2-K)
1019.5 (2V)	571.5	717.5	97	3144
0 (200mV)	112.0	121.8	27	
12	111.7	113.3	4	1924
12 (600mV)	168.1	174.0	10	1128
49.7	168.0	172.8	8	1379
98.4	168.0	171.9	6	1691
151	168.5	171.8	5	2005
201	168.1	171.8	5	2005
201 (800mV)	224.4	233.7	12	1201

Table 4-13: Experimental Data for asymptotic temperature rise technique for Probe #1 (new) using Nicolet Pro 30 and varying pressure and zero wind speed (5 May 97).

Input Voltage (V p-p)	V_L (mV)	V_U (mV)	1/e Rise Time (ms)	Overheat (K)	h (W/m^2-K)
1	279.2	286.8	0.750	10	6475
2	259.8	321.6	0.725	40	8120

Table 4-14: Sensitivity of coefficient of heat transfer to overheat condition (8 May 97).

4. Summary

The values for the coefficient of heat transfer, h, using the rise time method are consistent with those associated with the calculated ΔTs from Section IV-A. The values of h derived from the time constant method, Tables 4-8 and 4-10, are almost one half those from the asymptotic temperature rise technique, Tables 4-11 and 4-12.

The values of h are very sensitive to the amount of overheat, and therefore currents through the probe should be minimized to reduce error. Although measurements were made with four significant figures it was hard to achieve 20% accuracy in the values of h.

E. MEASUREMENT OF PROBE WIRE RESISTANCE

1. Purpose

The previous section measures resistance changes with probe current dynamically using digital oscilloscopes. Another method of determining h measured the probe resistance change with varying input current and changing wind velocity for static changes in the resistance. This version of the method in Section V-D relies on the accurate input of current to the probe and precise determination of current through the circuit using measured voltage across the load resistor, Figure 4-5.

2. Experimental Procedure

As shown in Figure 4-6 the probe resistance was measured using a Fluke 8840A multimeter and a $5^1/_2$ digit Keithley 197 Autoranging Microvolt DMM in response to a current input from the Hewlett Packard 6235A power supply. Different supply current levels were tried in order to minimize the overheat effects and change in load resistance with temperature. Relations for the calculation of ΔT and the coefficient of heat transfer have been developed in the previous section. Contact resistance in the probe was measured and considered in the results. Accurate determination of the load resistance was done with three independent instruments using the four wire measurement technique [Ref. 36].

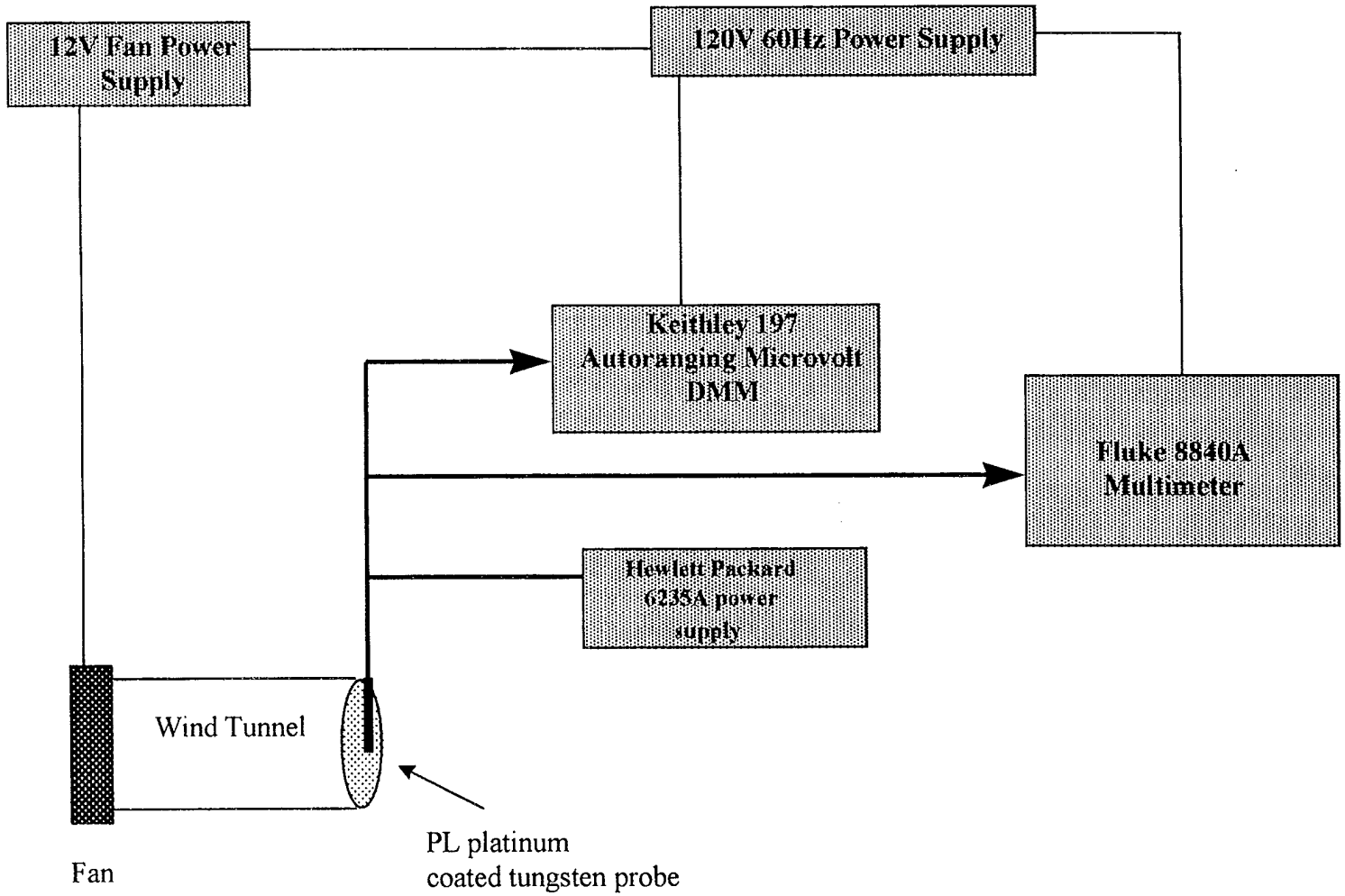

Figure 4-6: Laboratory bench setup for measurement of PL probe resistance.

3. Results

The results using

$$P = I^2 R = hA\Delta T \tag{47}$$

are shown in Table 4-15. The contact resistance of the probe was measured as 0.488Ω and has been subtracted from the tabular value of R_2 shown.

Possible error sources include a thermocouple type response of the probe wire supports and some heating effects from the Hewlett-Packard 331210A function generator.

Air Velocity (m/s)	V_1 (Volts)	R_1 (Ω)	I_1 (mA)	V_2 (Volts)	R_2 (Ω)	ΔT (K) with R_0=19.285	h (W/m^2K)
0	9.9847	999.15	9.9932	0.203364	20.3502	13.1511	2521.9
1	9.9889	"	9.9974	0.199086	19.9138	7.7633	4183.9
2	9.9901	"	9.9986	0.197777	19.7805	6.1175	5275.3
3	9.9909	"	9.9994	0.197103	19.7115	5.2656	6108.3
4	9.9913	"	9.9998	0.196650	19.6654	4.6965	6833.0
5	9.9915	"	0.0100	0.196344	19.6344	4.3137	7428.0

Table 4-15: Results of probe resistance method for determination of the coefficient of heat transfer of Probe #2 (9 May 1997).

4. Summary

Values for this method, which is a refinement of that used for Table 4-11 and 4-12, are also higher than predicted from either our model or the rise time technique.

V. DISCUSSION

A. MEASURMENT OF PROBE WIRE DIAMETER AND COMPOSITION

1. Purpose

All of the preceding experimental measurements and simulations rely on, among other parameters, the accurate knowledge of the platinum coated tungsten probe's diameter. The manufacturer, Thermo Systems Incorporated (TSI), gives this as 3.8 μm, but data taken in the course of this research raised doubt as to accuracy of this number.

Also questioned during the course of our research were the surface characteristics of the platinum coated tungsten wire as they relate to its reflectivity and heat transfer characteristics.

2. Experimental Procedure

A new sample purchased directly from TSI in 1997, and an older one obtained from the AFRL in 1991, were placed in the chamber of a Cambridge 20 KeV scanning electron microscope (SEM). The SEM had recently been calibrated and provided a scale accuracy of about 10 nm for our experiment. Measurements of the diameters were then taken at several positions along the wires, along with images of the regions measured. Images of the probe wires were also stored to disk for later analysis. A second sample of a Dantec pure platinum 5 μm wire was also imaged to provide further information about other vendor wire surface characteristics.

A Kevex Energy Dispersive X-ray (EDX) spectrograph then took representative measurements of the elemental composition at locations of the newer wire. These were recorded both where the platinum coating was present and at locations where spalling, thermal cycling, and possibly other processes had removed large patches revealing the underlying bare tungsten.

3. Results

Conservative measurements of the wire diameter at several locations, Figures 5-1 and 5-2, for the new wire revealed an actual diameter of 4.7 μm. Measurements of the older wire sample Figure 5- 3 showed its diameter to be 3.7 μm.

The characteristics of the new wire revealed an average of up to 22% bare wire (absence of platinum coating) over most of the surface with several large patches of bare tungsten, Figure 5-4 and 5-5. Striations in the platinum coating, very similar to the bark on a redwood tree, created a very rough and non-uniform reflective and radiative surface. (Figures 5-1,2,4,5,and 6).

In contrast to the rough surface seen in the new wire, Figures 5-1 and 5-2, the older wire's surface is significantly smoother and more reflective, Figure 5-3. Although the image quality is not quite as good as those for the newer wire, the lack of deep striations and dark patches is still discernible. The much smoother surface texture of a Dantec P11 pure platinum probe is shown in Figure 5-7.

Figure 5-8 shows that the tungsten areas were relatively pure in composition, while Figure 5-9 shows the significant amounts of copper that were detected by the EDX spectrum analyzer in the platinum areas. This probably indicates the presence of either contamination or impurities in the wire material, possibly introduced during the manufacturing process.

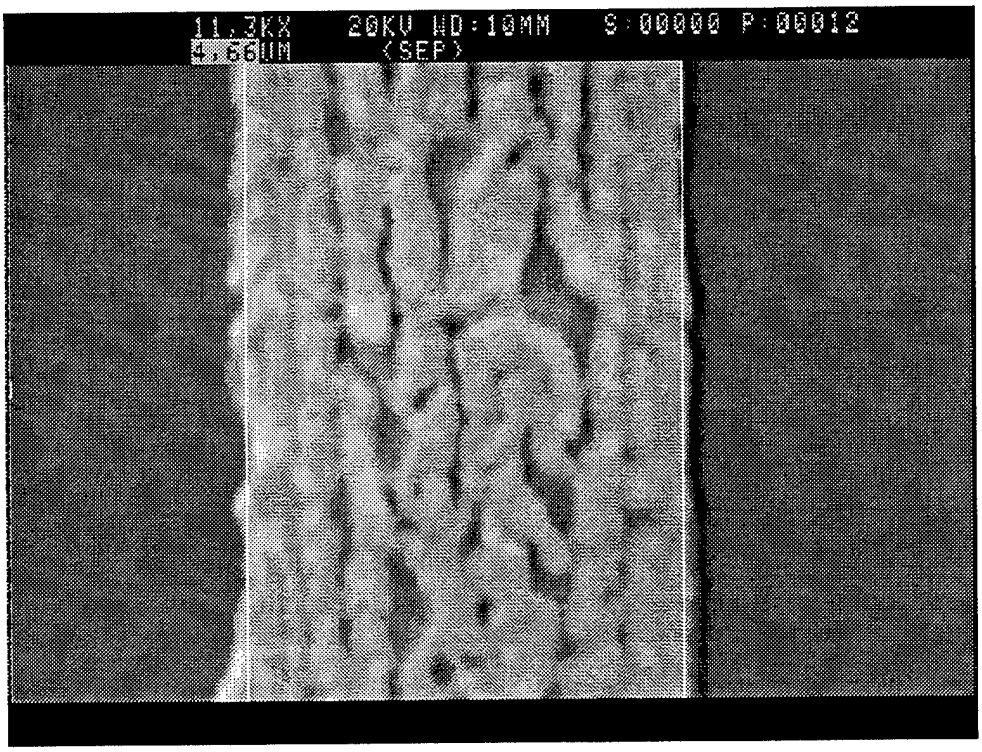

Figure 5-1: SEM image of the AFRL probe wire (new) showing a conservative diameter of 4.66μm.

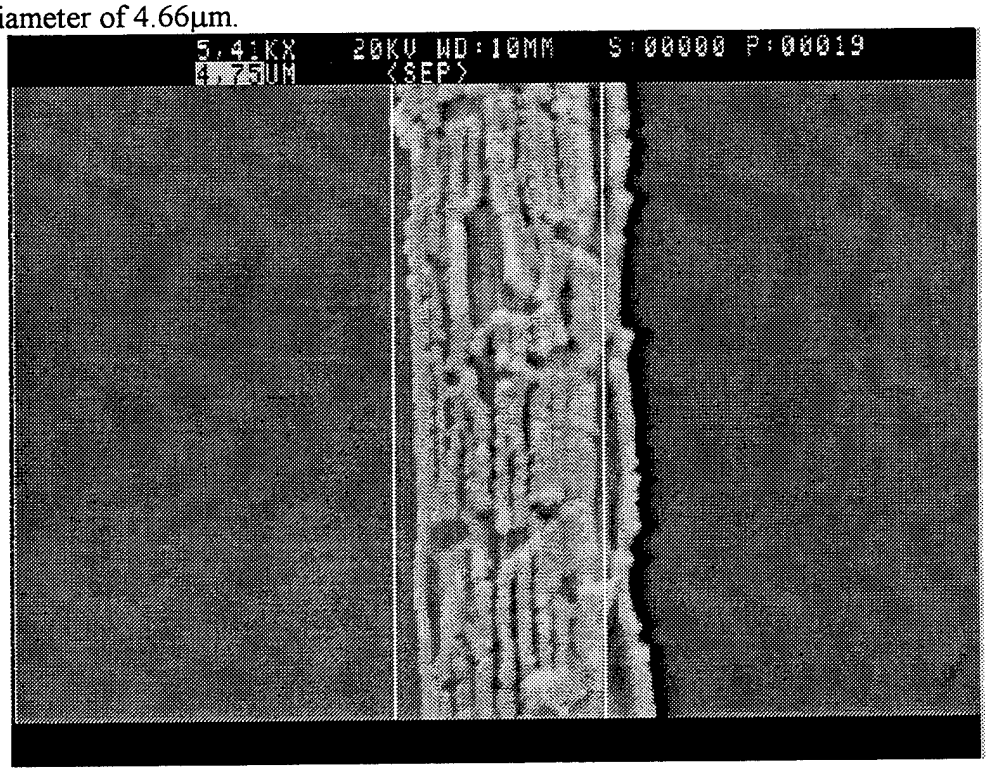

Figure 5-2: SEM image of portion of new wire with 4.75μm diameter and significant flaking .

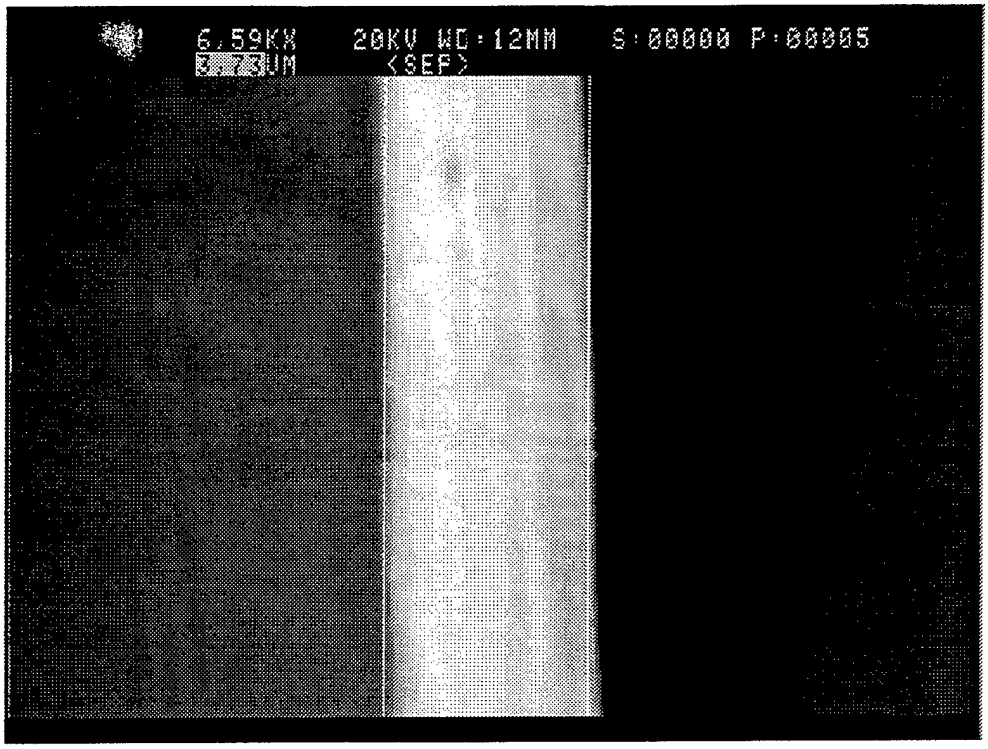

Figure 5-3: SEM image of portion of older (1991) wire with 3.73μm diameter.

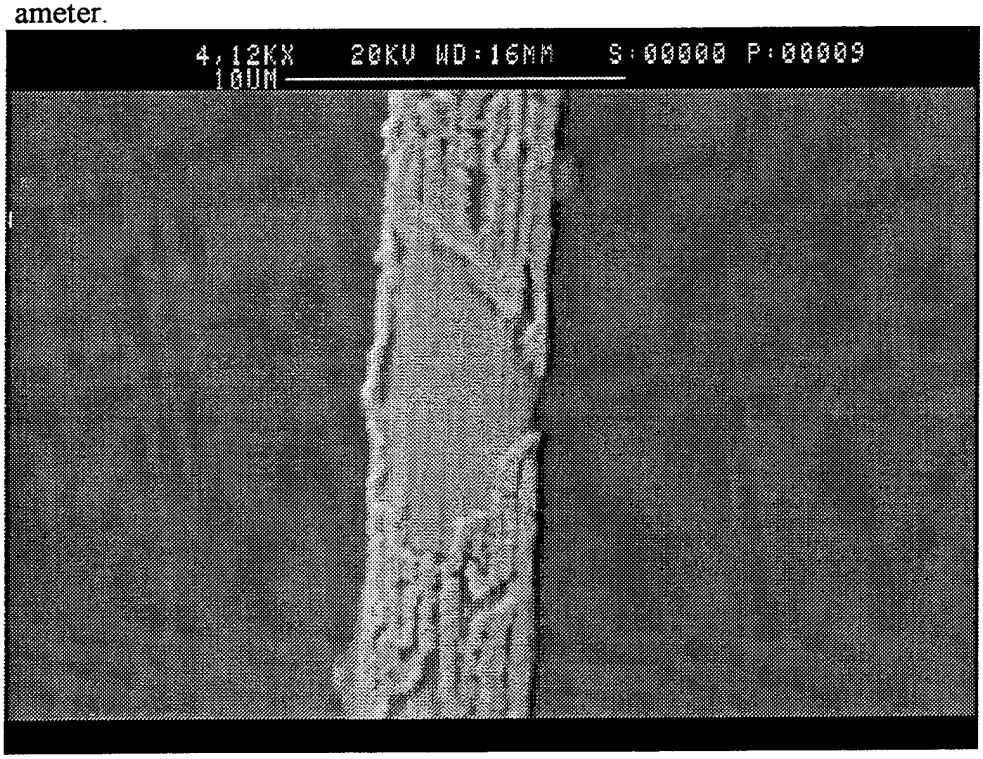

Figure 5-4: SEM image of large bare tungsten region with striations (new).

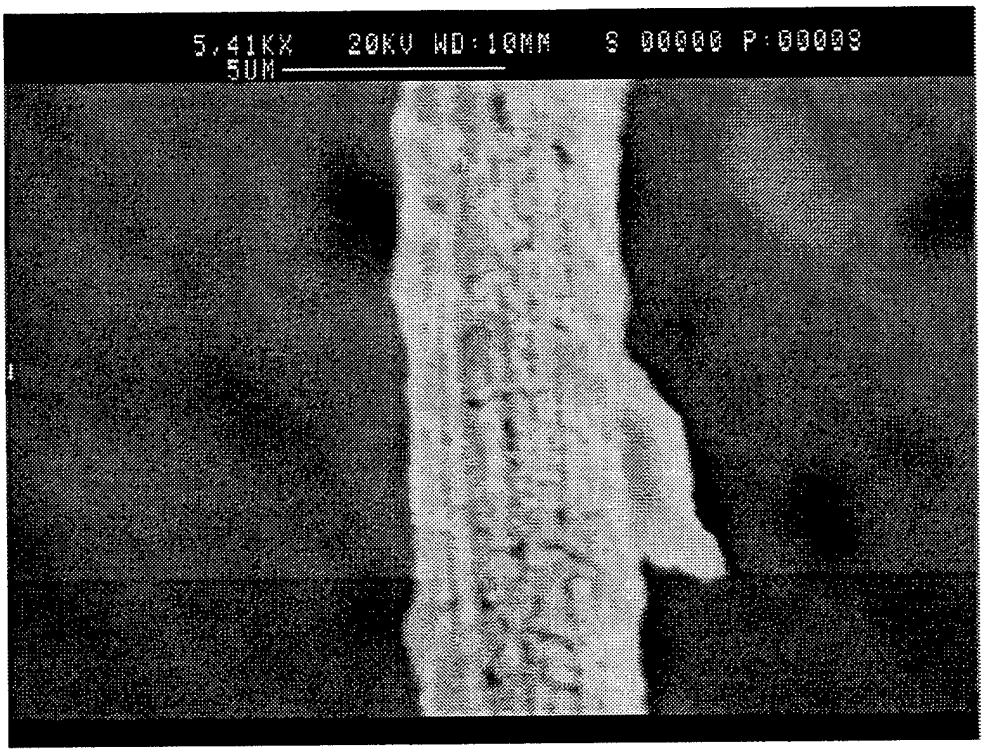

Figure 5-5: SEM image of striations and small bare patches (30 May 97).

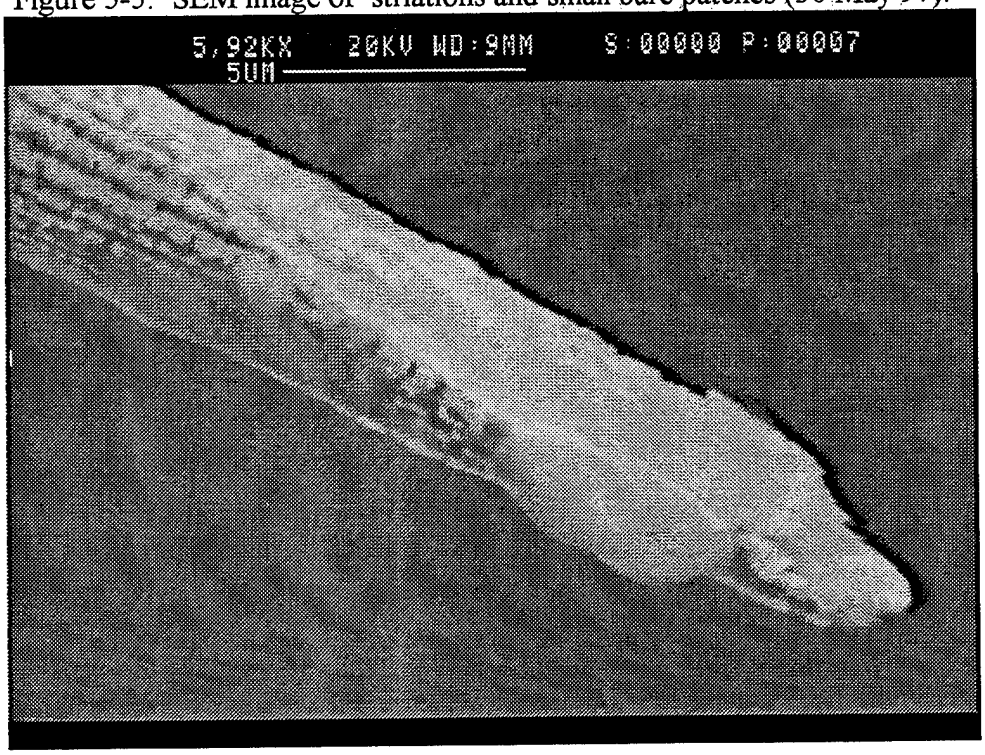

Figure 5-6: SEM image of wire end.

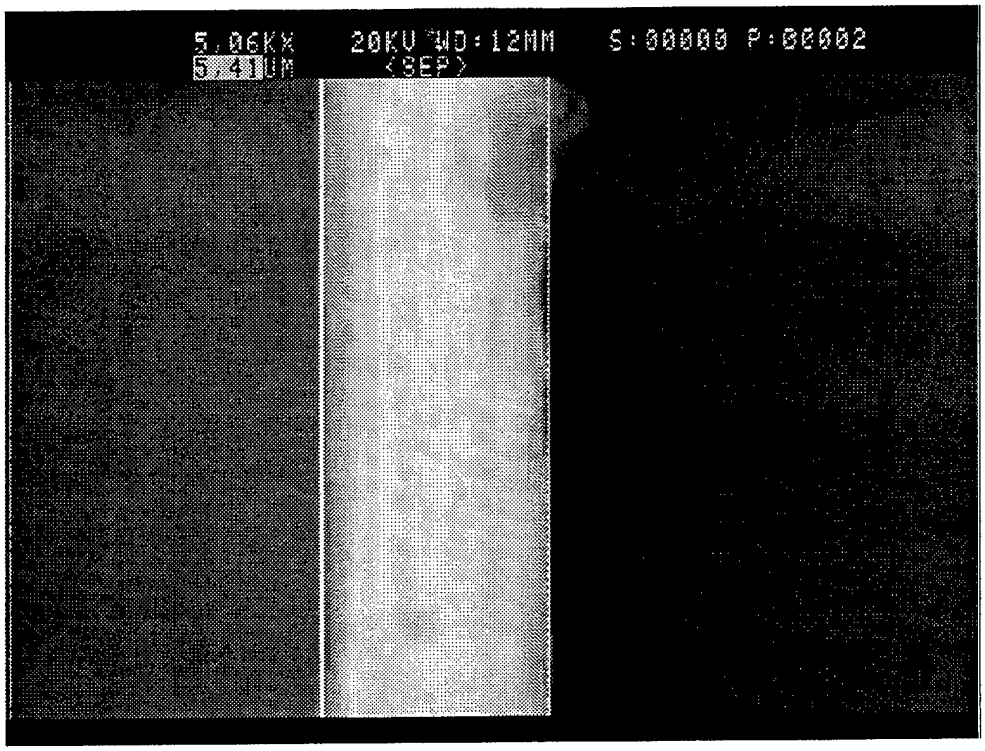

Figure 5-7: SEM image of a Dantec P11 5 μm pure platinum wire surface.

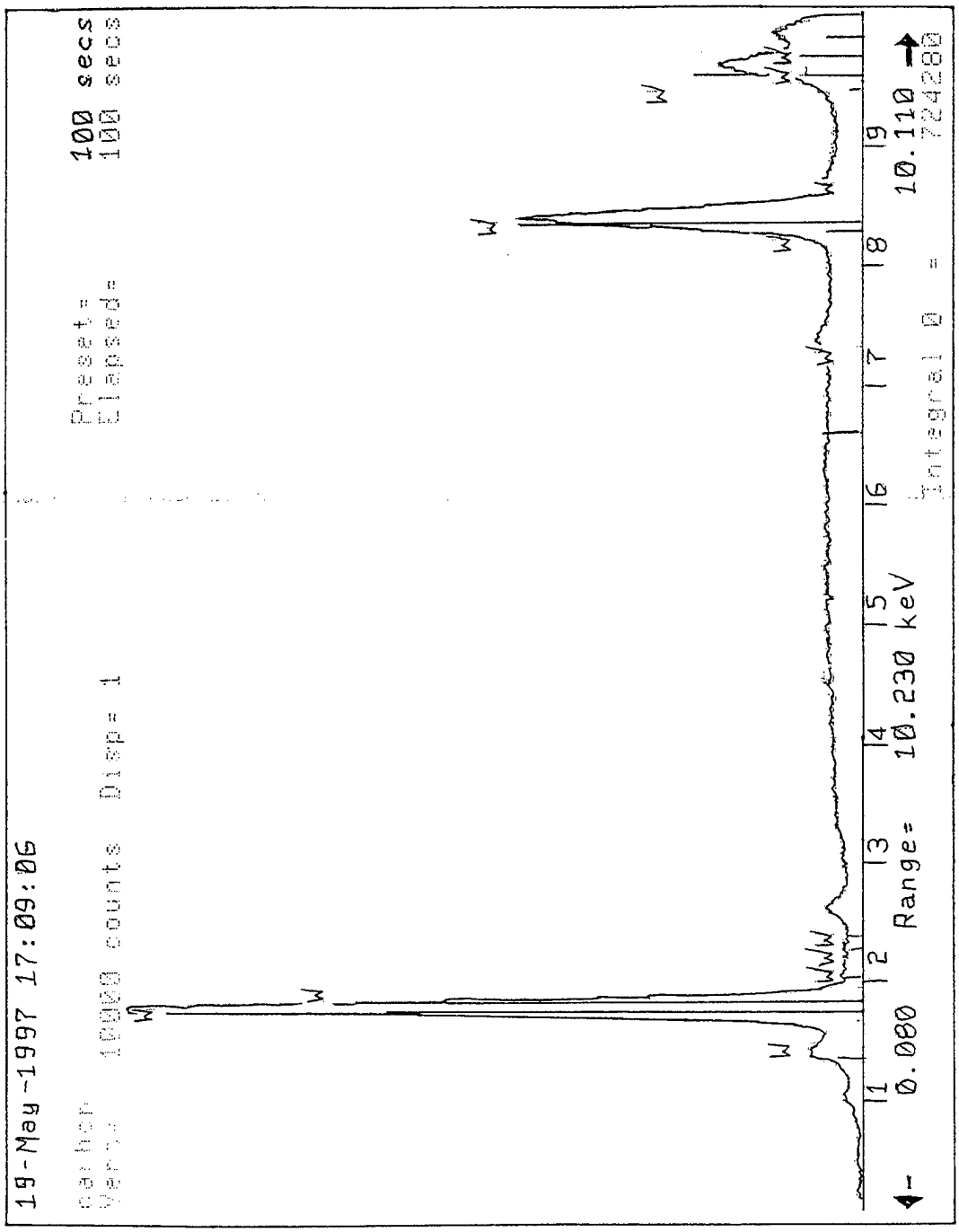

Figure 5-8: X-ray emission spectral components of bare tungsten wire.

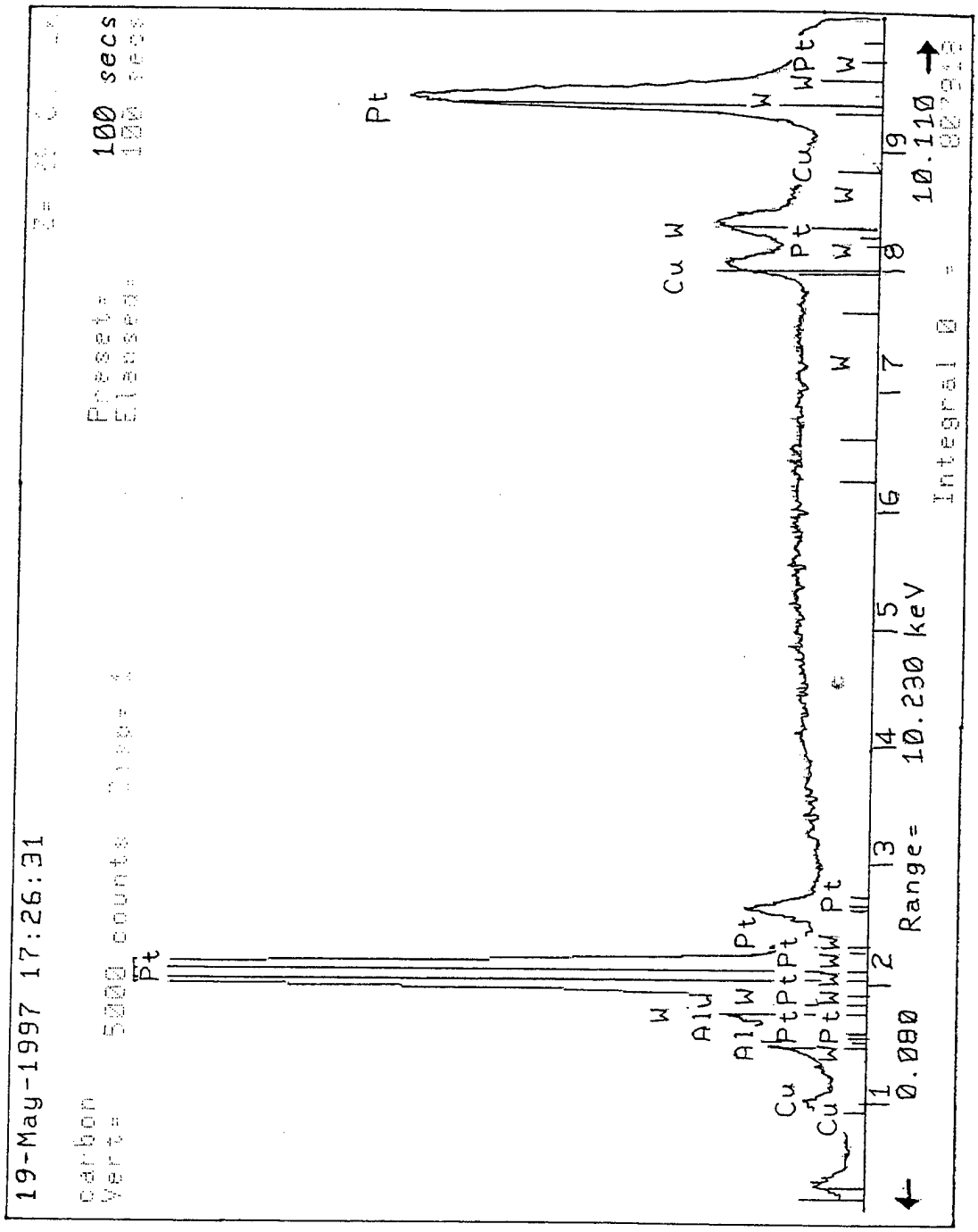

Figure 5-9: X-ray emission spectral components of platinum wire coating.

4. Summary

The new sample of the TSI platinum coated tungsten probe wire diameter was measured to be 24% greater than quoted by its manufacturer, while the older wire obtained from AFRL was 3% smaller than stated. Surface characteristics of the new wire showed a darker surface than appropriate for pure platinum and thus will introduce an error in the values for the emissivity and albedo assumed in the solar heating model calculations. Other heat transfer related effects from the rough and flaked surface of the new wire batch cannot be determined within the scope of this thesis research.

Overall, the older platinum coated tungsten wire showed very similar surface characteristics to the pure platinum wire, as expected. The newer wire was significantly different and showed marked surface roughness, bare patches, striations, and significantly larger diameter than specified.

B. COMPARISON OF MEASURED AND MODELED COEFFICIENTS OF HEAT TRANSFER, h

Figures 5-10 and 5-11 compare the coefficient of heat transfer as modeled in the MATLAB program of Chapter III, for Probes #1 and #3 and the two different measurement techniques, i.e., time constant and asymptotic temperature change. The large discrepancy using the asymptotic temperature change technique and the time constant procedure for both probe wires is not understood and is still under investigation.

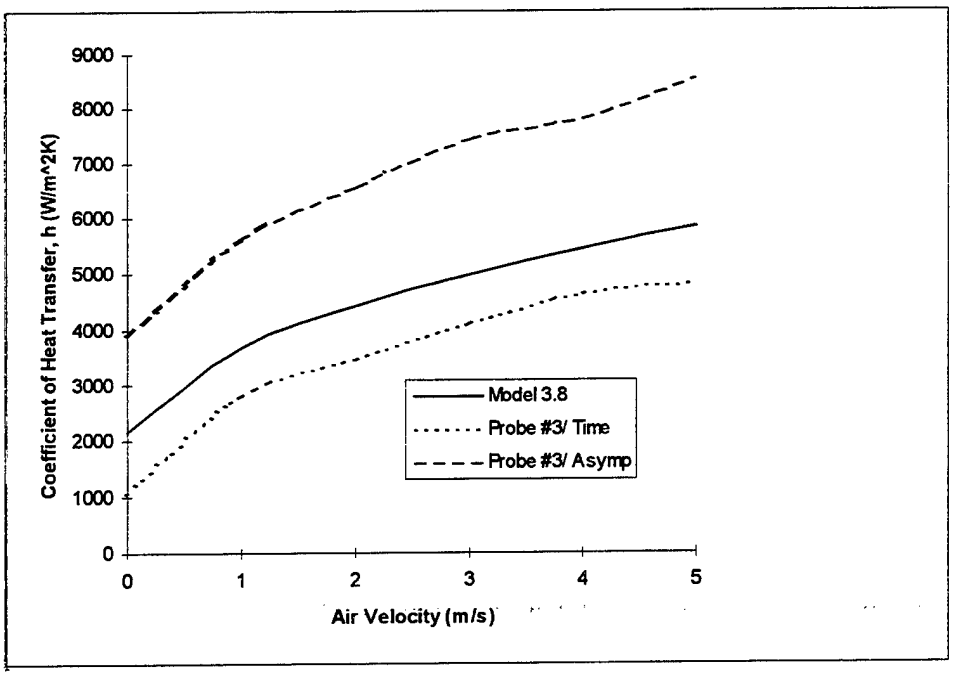

Figure 5-10: Modeled and measured h, for the 3.8 μm Probe #3 for measured rise time and asymptotic temperature increase techniques.

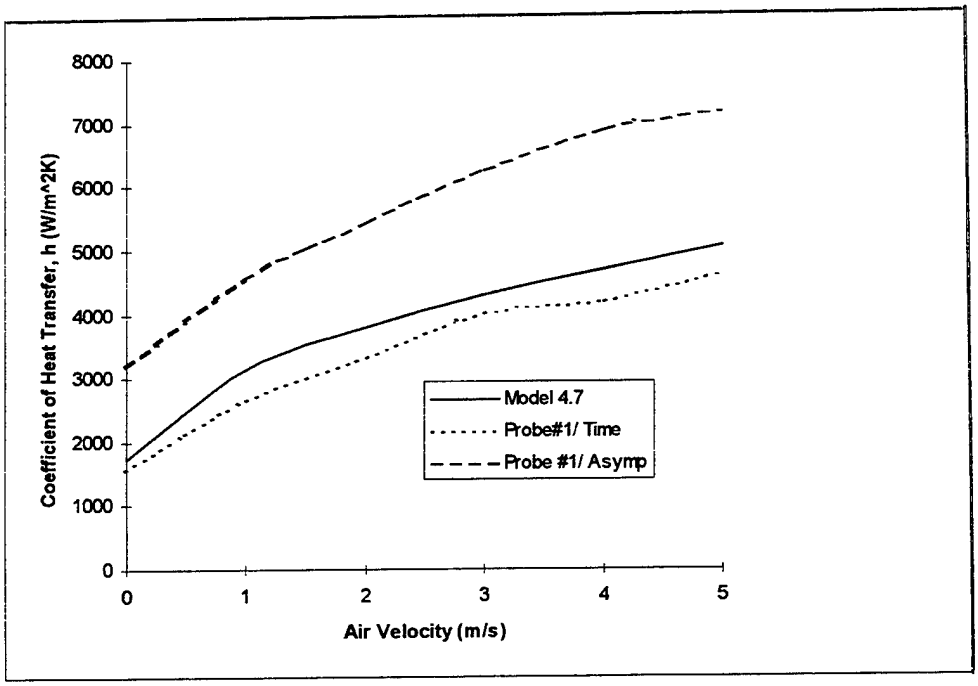

Figure 5-11: Modeled and measured h, for the 4.7 μm Probe #1 for measured rise time and asymptotic temperature increase techniques.

C. COMPARISON OF MEASURED AND MODELED DIFFERENTIAL TEMPERATURES

Figures 5-12 and 13 compare the differential temperature rise from solar and ohmic heating effects, measured experimentally in Section IV-A, to temperatures computed using the MATLAB model of Chapter III. Measured Probe #3 data , in Figure 5-12, compares favorably to the models for emissivities of 0.435 (platinum coated tungsten) and 0.444 (pure tungsten). The 4.7 μm Probe #2, Figure 5-13, does not correlate as well most likely due to the unknown heat transfer and absorption effects caused by the poor surface characteristics previously mentioned.

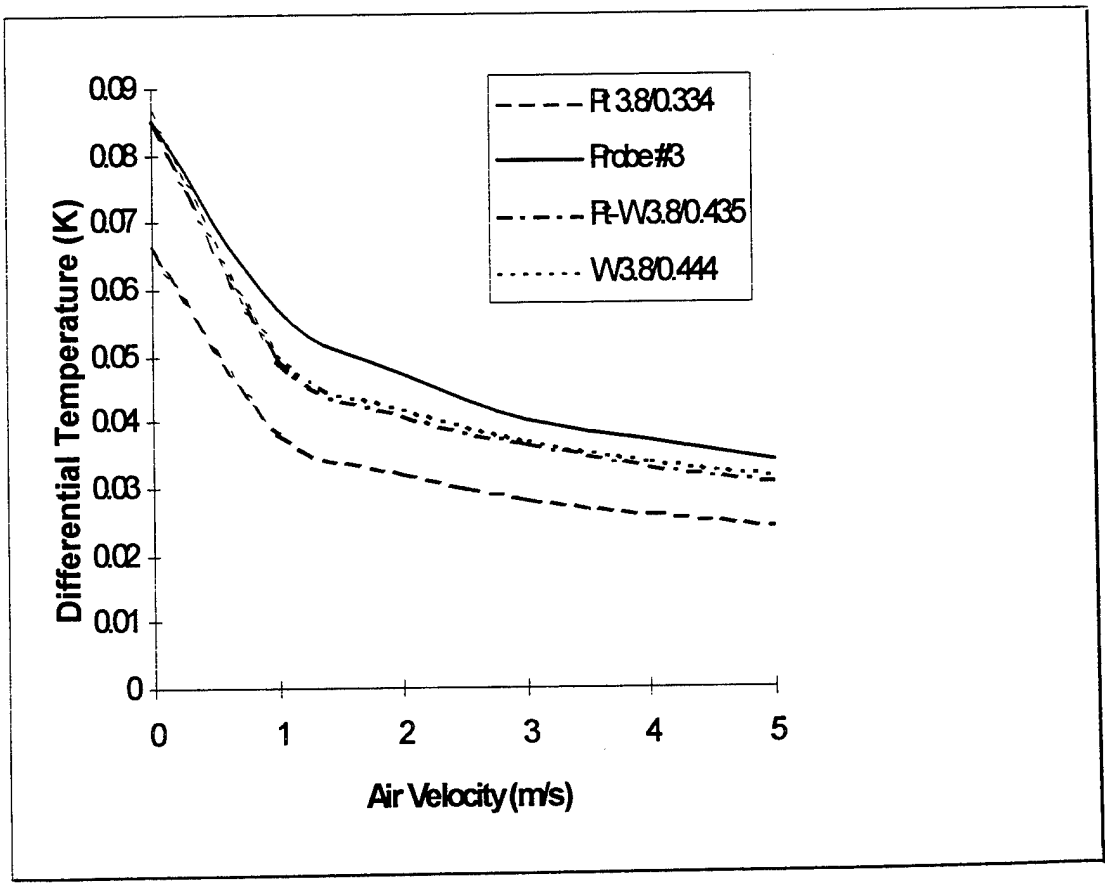

Figure 5-12: Modeled (dashed and dotted)and measured (solid) data for the 3.8 μm platinum coated tungsten wire Probe #3 differential temperature from solar and ohmic heating. Emissivities of 0.334 (pure Pt), 0.435 (Pt-W), and 0.444 (pure W) are shown for the modeled curves.

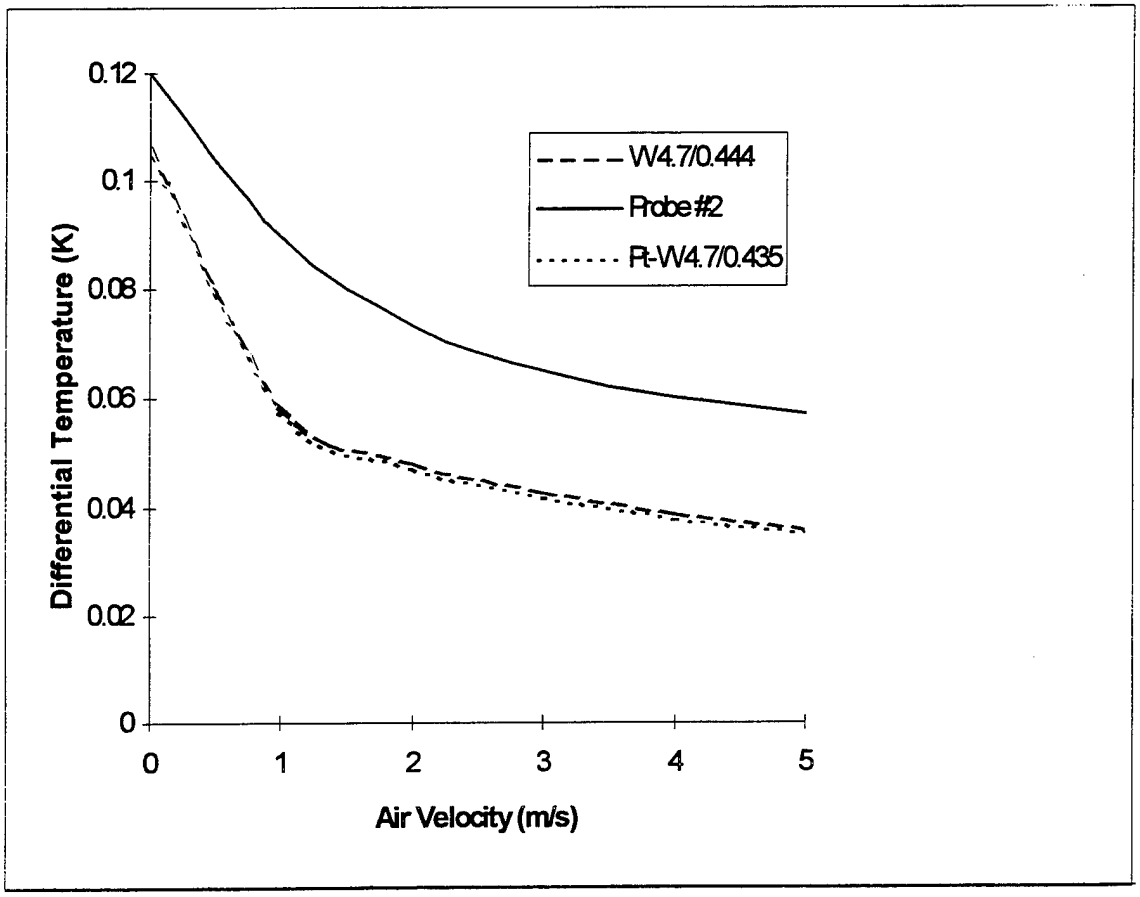

Figure 5-13: Modeled (dashed and dotted) and measured (solid) data for the 4.7 μm platinum coated tungsten Probe #2 differential temperature from solar and ohmic heating. Emissivities of 0.435 (Pt-W) and 0.444 (pure W) are shown for the modeled curves.

D. EFFECT OF PROBE WIRE DIAMETER VARIATION

The MATLAB simulation program developed for Chapter III provides a way to investigate the effect of different probe wire diameters on the differential temperature. Changes in the probe wire diameter with altitude on the differential temperature are reflected in Figure 5-14. Simply reducing the wire diameter will reduce the probe's differential temperature. For example, a reduction in wire diameter from 5 to 2 μm would result in a ΔT reduction from 0.16 to 0.07 K or a 64% improvement, at 30 km. Further

reduction of probe diameter below 2 μm into the more pronounced non-linear region would have a larger effect.

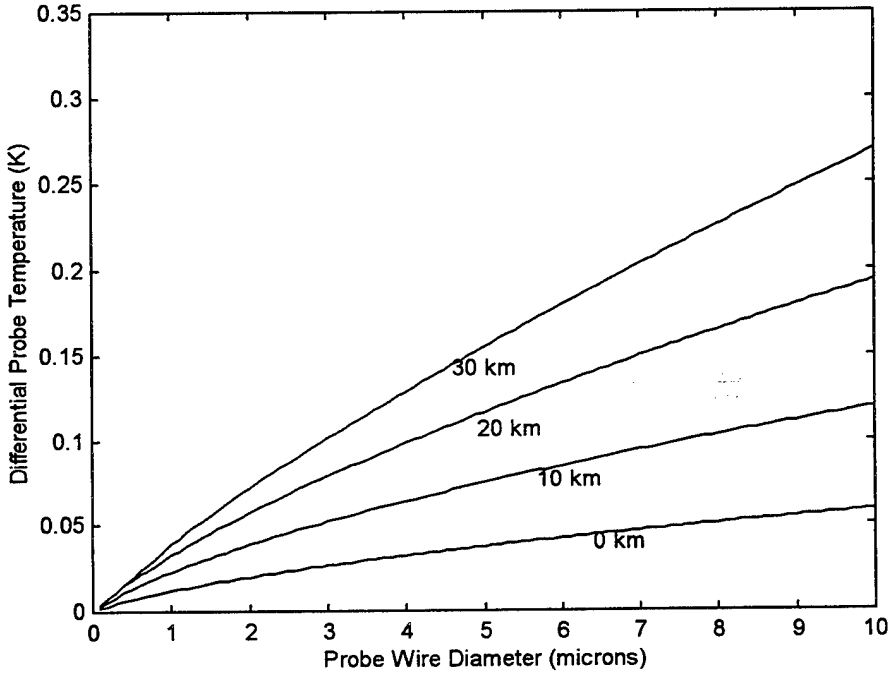

Figure 5-14: Effect of varying the AFRL probe wire diameter for the platinum coated tungsten wire on differential temperature at constant altitude and air velocity of 5 m/s.

E. EFFECT OF PROBE MATERIAL AND DIAMETER CHANGES

In light of the very poor surface characteristics discovered for the TSI wire, other probe wire materials were considered. The dominant parameter affecting the probe wire's solar absorption is the spectral emissivity. The spectral emissivity of several favorable replacement materials where calculated using the following relation:

$$\varepsilon_\nu = \frac{\int_0^\infty \rho(\nu)\alpha(\nu)d\nu}{\int_0^\infty \rho(\nu)d\nu}, \tag{48}$$

where $\alpha(\nu)$ is the absorptivity as a function of frequency and

$$\rho(\nu)d\nu = \frac{8\pi\nu^2}{c^3}\frac{h\nu}{e^{\frac{h\nu}{kt}}-1}d\nu, \tag{49}$$

which is the Planck blackbody spectrum [Ref. 32:p. 17]. Curves for the spectral emissivity versus energy from values tabulated in the CRC Handbook are compared with the corresponding black body spectrum of the sun, a 6000 K body, in Figure 5-15. The black body spectrum was used as the weighting factor for Figure 5-16, which compares the integrand of Eq. (48) for the four metals. Completing the above integrals, over the range corresponding to the transparent region of the atmosphere, about 0 to 195 nm, we then arrive at Table 5-1 which lists the spectral emissivity for the five wire materials investigated.

Revisiting the previous section and using the spectral emissivities of the new materials we can plot the change in differential probe temperature with varying wire diameter at a constant altitude and air velocity of 5 m/s as shown in Figure 5-17.

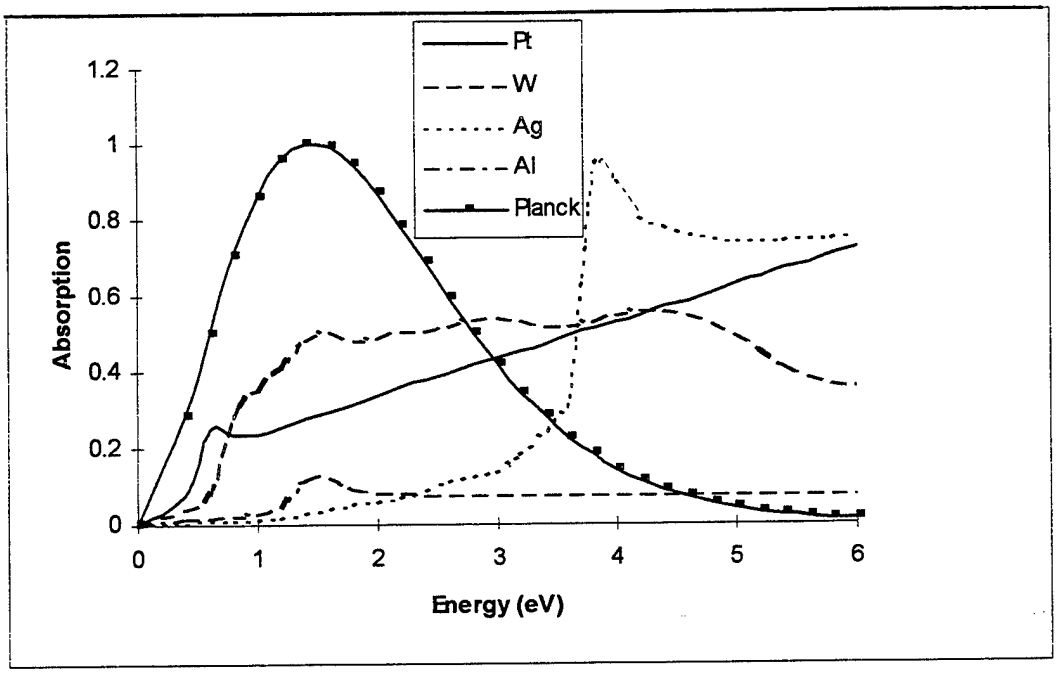

Figure 5-15: Emissivity versus energy for some probe materials of interest with 6000 K black body for comparison.

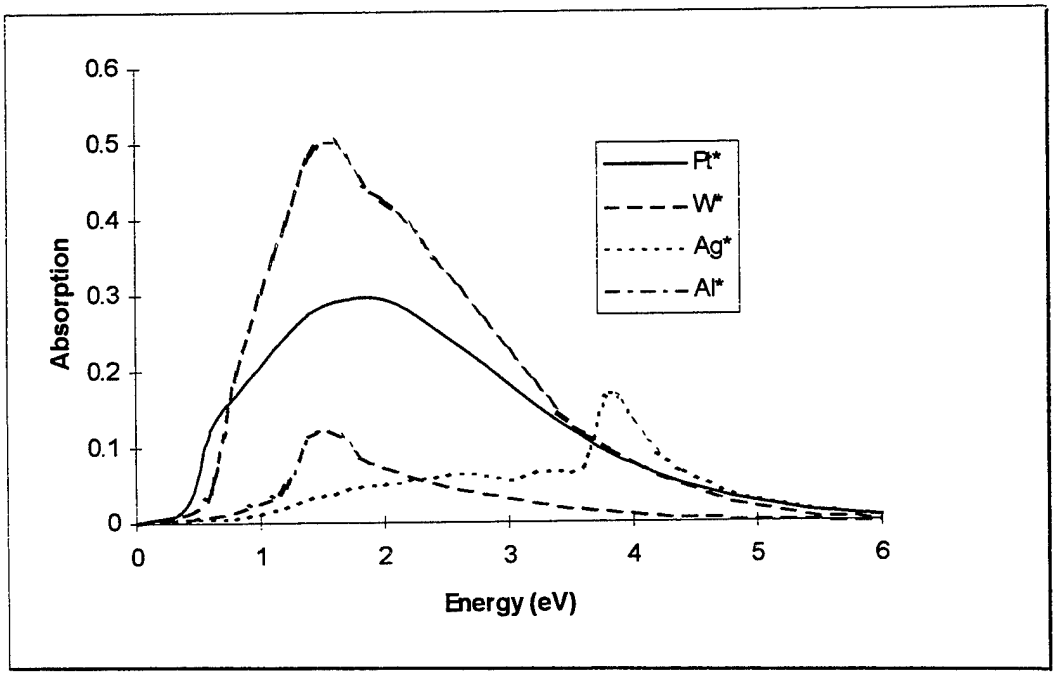

Figure 5-16: Weighted emissivity curve for different probe wire materials.

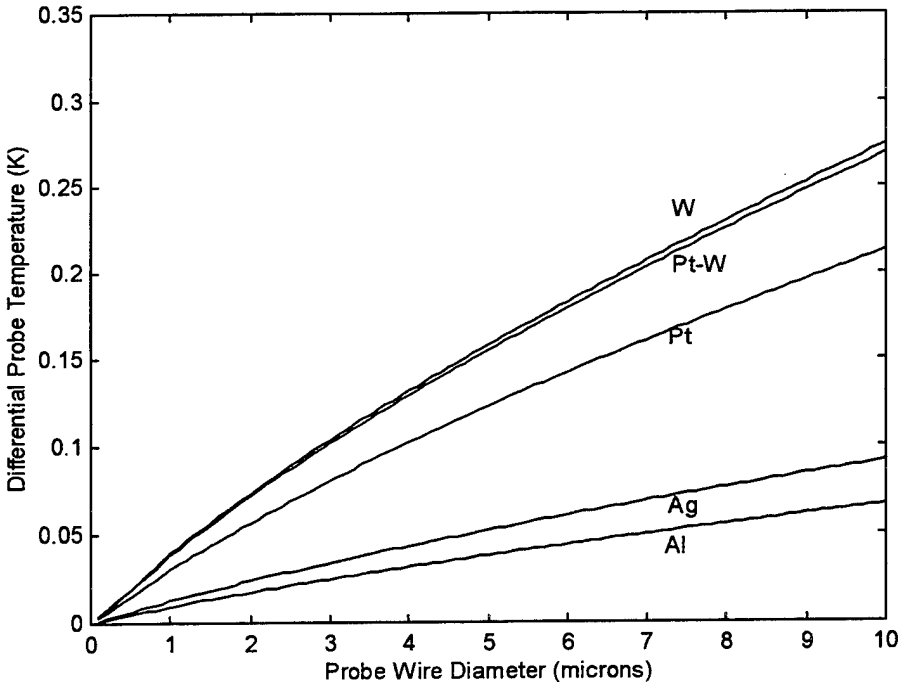

Figure 5-17: Effect of change in spectral emissivity on differential temperature and wire diameter at 30 km and 5 m/s.

Wire Material	Tungsten (W)	Platinum (Pt)	Silver (Ag)	Aluminum (Al)
Spectral Emissivity	0.444	0.334	0.116	0.073

Table 5-1: Average spectral emissivities of some selected metals for the solar spectrum.

In Figure 5-17 it is evident that a change of wire material from the present platinum coated tungsten to silver would improve wire solar absorption performance by 67% with both wire diameters at 5 μm and at an altitude of 30 km. Reduction of the wire diameter to 2 μm and change in material to silver would reduce the solar heating by 85% at 30 km. Since C_T^2 is proportional to ΔT^2 a factor of 6.7 reduction in the solar induced temperature would reduce C_T^2 error by a factor of 45.

VI. CONCLUSIONS

In this thesis, the measured values for the solar heating of the 4.7 μm platinum coated tungsten probe varied from 0.055 K at 5 m/s to 0.12 K at 0 m/s and 0.034 K at 5 m/s to 0.085 K at 0 m/s for the 3.8 μm probe, at sea level. These values were 12% to 34% larger than predicted by the detailed model for the 4.7 μm probe. Much better agreement occurred for the 3.8 μm platinum coated tungsten probe. Measurements and model results agreed to within 1-7%. Direct solar heating of the probe is significant. Temperature fluctuations over 0.175 K, at 30 km, can be induced for both 3.8 and 4.7 μm probes through the periodic modulation of the rotation and pendulum motion of the sonde package both due to the direct illumination (heating) of the probe but also because of the changing air flow (cooling) over the probe (Table 3-4). Notably, the maximum change in the probe's differential temperature occurs at an intermediate altitude of 11 km with decreasing differential magnitudes occurring above and below this altitude. This effect is due to solar heating and is best shown in Figures 3-21 and 3-22.

The uncertainty in measured versus modeled values for the differential temperature of the 4.7 μm platinum coated tungsten probe in the atmosphere is most likely due to the complicated surface characteristics of the TSI wire. Convection, radiation, and air flow in and around this rough surface introduces unknowns which could easily be of sufficient magnitude to account for the measured differences.

The determination of the value of the coefficient of heat transfer, h, is important in characterization of the probe's ability to transfer energy and was therefore modeled and measured with great care. Final values of h calculated through the model and measured experimentally agreed to within 20% at air velocities of 0 m/s and 10% at air velocities near 5 m/s. Probe wire surface characteristics most likely account for the consistently higher differential temperatures, of about 0.002 K, measured experimentally for the 4.7 μm probe.

Susceptibility to the direct solar heating effects can be substantially reduced by minimizing the probe wire diameter. Additional improvement to solar contamination effects can be realized by changing the probe material, notably to silver or aluminum.

VII. RECOMMENDATIONS

The best solution to solar contamination of data would be to perform only night data collection. As this is not always an option in all research and tactical situations other options are necessary. The TSI platinum coated tungsten wire measured has been shown to have very poor characteristics, from a solar absorption standpoint, and thus would be a prime candidate for replacement. This may have been a result of manufacturing defects. Options include pure platinum wires which present a much more reflective and thermally smooth surface or another material such as silver or aluminum. The diameter of the probe wire is also a major contribution to solar contamination and should be reduced. Similarly, the thermal heating of the probe supports must be minimized using highly reflective materials.

Replacement altogether of the probe assembly has been proposed. Some replacements include an acoustic sounder sensor or a laser/optical device. If the old design probe must be used for balloon sounding, further research could be performed into stabilization techniques for the sonde to minimize or remove the geometry dependence of the balloon - sun system. For the near term, reduction in the probe wire diameter and shift to a new wire material, such as silver or aluminum, is highly recommended.

APPENDIX A- AIRBORNE LASER PROGRAM SUMMARY

Table A-1: Highlights of the Airborne Laser Program acquisition process [Ref. 6:p. 12].

September 1992	Boeing and Lockheed receive separate contracts to assess how well existing large airplanes, the 707, 747, 767 and B-52 would perform while carrying a high-energy laser and beam control system. Both teams separately reach the same conclusion and recommend a 747 platform to the Air Force as the best option for the mission.
August 1993	Team ABL Proposal submitted
April 1994 (MS0)	Team ABL and Rockwell selected as two competing teams for Concept Study Design ($21 million, 33-month contract)
March-November 1995	Boeing conducts series of "Flex Blue" tests to determine vibration environment for the Airborne Laser.
April 1995	TRW begins construction of BDL-2, (building block COIL).
May-October 1995	Boeing Wind Tunnel Testing of Turret Designs.
July 1995	TRW TRACE facility produces first laser light to demonstrate 10 kW laser power goal
September 1995	Air Force Operational Concept Review (OCR).
October 1995-present	Lockheed Martin beam control tracking, pointing and adaptive optics compensation demonstrations
January 1996	Draft RFP for PDRR phase released
February 1996	Lockheed Martin beam control system brassboard operational
March 5-8, 1996	Team ABL Concept Design Review with Air Force; Final Package due within 30 days.
March 1996	Second Draft RFP for PDRR released.
May 1, 1996	U.S. Air Force releases Airborne Laser final PDRR RFP.
June 1996	TRW plans demonstration of 200 kW Laser modules.
July 1996	Team ABL submits Airborne Laser PDRR Proposal Response.
October 1996	Final technical program update to Air Force.
November 12, 1996 (MSI)	Air Force selects Team ABL as one contractor for Airborne Laser Dem/Val. $1.1 billion 5 year Program Definition and Risk Reduction (PDRR)contract to Team ABL (Boeing/Lockheed Martin/TRW) (c1)
1996-2000	PDRR Phase I (build one PDRR aircraft).
2000-2001/2	PDRR Phase II (test and fly PDRR aircraft.
2001/2-2004 (MSII)	Engineering Manufacturing and Development (EMD).
2004-2008 (MSIII)	Production (IOC 3 aircraft 2005/6, FOC 7 aircraft 2007/8).

Figure A-2: Airborne Laser Program acquisition timeline.

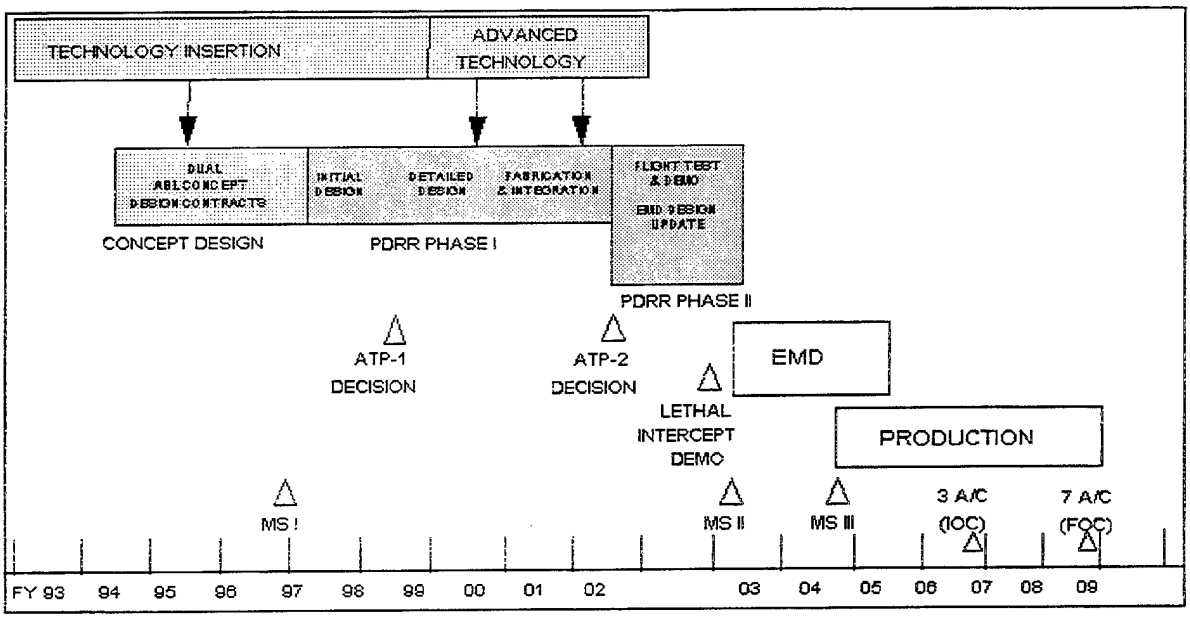

Figure A-2: ABL Program structure

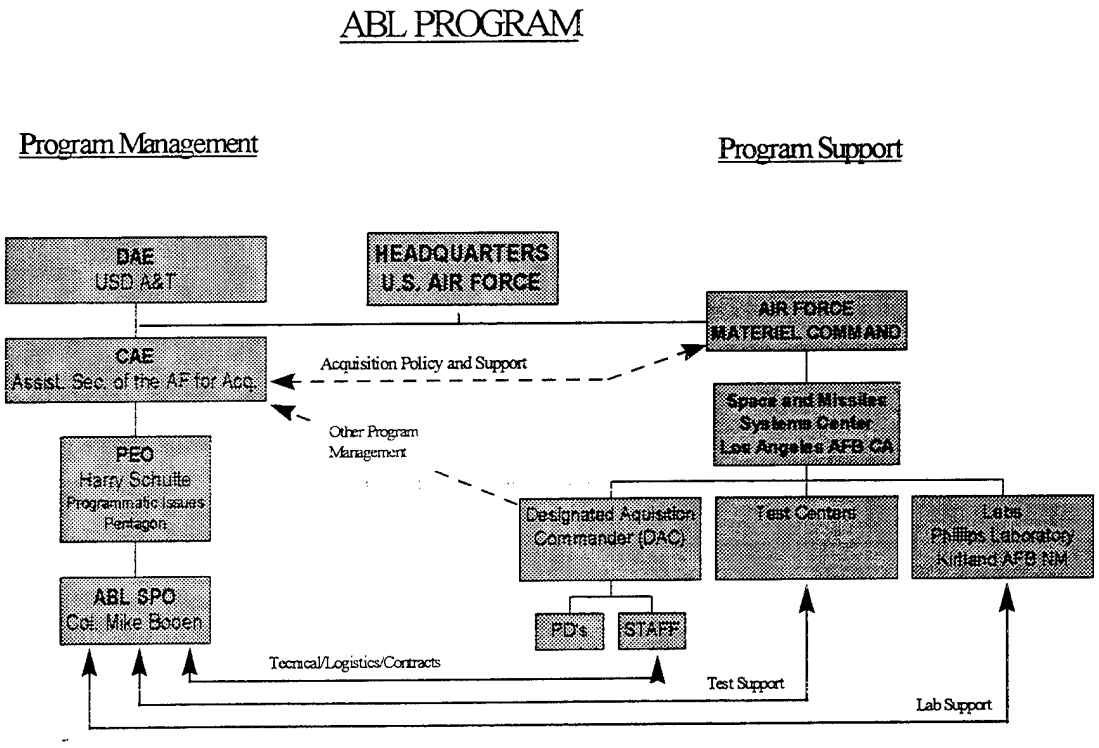

APPENDIX B - PROBE SIMULATION PROGRAM

```
%Daniel J. Richardson
%13 May 97

%Probe Temperature vs. Air Temperature
%Using Free and Forced Regimes
%and Low Re number Equations

%Set Constants:
    alpha=0.435;        %Solar Absorptivity of Probe
    epsilon=0.065;      %Emmisivity for 300K Radiation
    gamma=0.39;         %Solar Energy Reflected by the Earth (Albedo)
    sigma= 5.67e-8;     %Stefan-Boltzman Constant[W/m^2.k^4]
    Pe=615;             %Long Wave Radiation from Earth [W/m^2]
    Pa=250;             %Long Wave Radiation Emmited by the Atmosphere [W/m^2]
    k=0.3;              %Atmospheric Transmission Term
    D=4.7e-6;           %Diameter of Probe Wire [m]
    L=4.0e-3;           %Length of Probe Wire [m]
    v=5;                %Balloon Ascent rate
    beta1=1.458e-6;     %Dynamic Viscosity constant [kg/smk^1/2]
    S=110.4;            %Sutherland's Constant [K]
    z0=8.1;             %Scale Height [km]
    p0=101300;          %Scale Pressure [Pa]
    M=0.0289644;        %Mean Molecular Weight [kg/mol]
    R=8.31;             %Universal Gas constant [J/mole K]
    Psurf=890;          %Solar flux at the surface of the Earth [W/m^2]
    W=2.5;              %Wind Velocity Factor
    c=1010;             %Specific Heat [J/kg K]
    g=9.82;             %Gravity
    beta2=3.66e3;       %Coefficient oc thermal expansion [1/K]

%Atmospheric Variables:
    Altitude=0:10:30e3;    %Altitude in [m]
    kt=Altitude;           %Define array size
    Ps=Altitude;           %Define array size
    A2=Altitude;           %Define array size
    t=Altitude;            %Define array size
    Pr=Altitude;
    Re=Altitude;

  for i=1:length(Altitude);
      if (Altitude(i)<11000)
         T(i)=(Altitude(i)/1000-44.62)/(-0.15493);      %Temperature of Atm. [K] (0-11km)
         kt(i)=((Altitude(i)/1000)-50.57)/(-1983.47);   %Thermal conduct.[W/m-K] (0-12km)

      elseif (Altitude(i)>=11000 & Altitude(i)<20000)
         T(i)=217;                                      %    "     (11-20km)
         kt(i)=0.0195;                                  %    "     (12-20km)

       else
         T(i)=(Altitude(i)/1000+142.75)/0.75;           %    "     (20-30km)
         kt(i)=(Altitude(i)/1000+206.5)/11636;          %    "     (20-30km)
      end
  end

    Ps=(Altitude.^0.584)+890;            %Solar Flux [W/m^2]
    P=p0*exp((-Altitude/1000)/z0);       %Pressure [Pa]
    mu=beta1*(T.^(3/2))./(T+S);          %Dynamic Viscosity
    rho=(M.*P)./(T.*R);                  %Density
    nu=mu./rho;                          %Kinematic viscosity [m^2/s]

    %v=W*randn(size(Altitude))+5;        %Random Air velocity generation around probe

    deltaT=0.1;
    Gr=((rho.^2)*g*beta2*deltaT*(D^3))./mu;  %Grashof number
    Re=D*abs(v)./nu;                         %Reynolds Number
    Reef=(Re.^2+(0.9*Gr.^0.418).^2).^0.5;    %Effective Reynolds number mix.Convection
    Pr=(mu.*c)./kt;                          %Prandtl Number
```

```
    for j=1:length(Altitude)
        if (Re(j)<0.0132 )                    %Check for Free Convection ONLY regime
            h(j)=(0.32*kt(j)./D);             %p.131 Bryan

        else
            h(j)=(0.24+0.56*Reef(j).^0.45).*(kt(j)./D);  %Mixed convection
        end
    end

Nu=D*h./kt;             %Nusselt Number

%Areas Seen by the Probe:
    A1=pi*D*L;          %Surface Area of Probe wire
    A2=(D*L);           %Area of Probe seen by Sun
    t=0:0.25:750;
    ps=randn(1);        %phase factor for sun area
    pe=randn(1);        %phase factor for the Earth area
    wp=(2*pi)/20;       %angular frequency of Pendulum motion
    wr=(2*pi)/5;        %angular frequency of Rotation

    A2=abs(1.52e-8*(sin(wp*t+ps)+sin(wr*t+pe)))/2;      %Sinusoidal Sun Area Variation
    A4=abs(1.52e-8*(sin(wp*t+ps)+sin(wr*t+pe)))/2;      %Sinusoidal Earth Area Variation

    A3=A1;              %Area of Probe Radiating
    A4=(D*L);           %Area of Probe seen by Earth
    A5=A4;              %Area of Probe seen by Earth reflected Sunlight
    A6=A1;              %Area of Probe seen by Atmosphere


%Energy to/from the Probe:
   Solar=(alpha*A2.*Ps);              %Energy from the Sun
    Planck=(epsilon*sigma*A3*T.^4);   %Planck radiation term for Probe
    EarthS=(alpha*A4*Psurf*gamma);    %Reflected Energy of Sun from Earth
    EarthP=(k*epsilon*A5*Pe);         %Long Wave Planck Radiation from the Earth
    AtmP=(epsilon*A6*Pa);             %Long wave Planck Radiation from Atmosphere

   Tprobe=(Solar-Planck+EarthS+EarthP+AtmP+A1*h.*T)./(h.*A1);   %Final Probe Temp

    %deltaT=.095;
   Convection=h.*A1.*(Tprobe-T);      %Convective Heat Transfer from wire


%semilogx(Tprobe-T,Altitude/1000);
plot(h, Altitude/1000)
%grid;
%title('Probe Delta Temperature vs. Air Temperature');
ylabel('Altitude (km)');
xlabel('h');
```

APPENDIX C - DATA ANALYSIS PROGRAM

MATLAB Data Analysis program developed by Prof. Donald L. Walters:

```
% vizdata.m program to read the Sept 90 Anderson peak
%
% 21 Apr 1997: DLW
% set up constants
    fsample=1/1.25;
    f0=1/(2*pi);        %filter
    nfft=256;
    n2=nfft/2;
    n=52;

% setup up file parameters
    fid=fopen('c:\Met data\Ap092716.txt','r');
    cols=7;     % # of columns in the data set
    col=5;  % column # of temperature data

% read the file of arbitrary size
    [a,count]=fscanf(fid,'%f\t');
    status=fclose(fid);
    rows=count/cols;
    a=reshape(a,cols,rows);
    a=transpose(a);

% extract the high speed temperature data column
    b=a(:,col);
    c=b(rows-(nfft-1):rows);  %select end of array
    c=detrend(c);
    d=ifft(c);
    e=conj(d).*d;
    ps=e(2:(n2+1));                %subset of psd without DC term

% create frequency array
    f=1:n2;
    f=f*fsample/nfft;
    plot(f,ps);

% create RC high pass filter
    f1=(f/f0).^2;
    fltr=f1./(1+f1);        %One pole filter
    fltr=fltr.*fltr;        %Filter applied twice

% spectral variance fltr * psd (with + and - frequencies)
    ps2=ps.*fltr';
    semilogy(f,ps2)
    var=sqrt(2.*sum(ps2))

% time domain filter
    [B,A]=butter(1,0.16/.4,'high');   % create one pole RC
    b2=filter(B,A,b-b(1)   );            % apply filter
    b3=filter(B,A,b2);                % apply filter again
    var2=std(b3(100:rows))

% Compute Cn2
    z=a(:,2);               % Altitude
    cn2=b3.*b3.*(79e-6*(a(:,3)./(a(:,4).^2))).^2;

% Lowpass smooth the data
    [D,C]=butter(2,.05);
%   cn2=filter(D,C,cn2);
    semilogx(cn2,z,'r')
    axis([1.0e-20 1.0e-13 0 20000])
```

APPENDIX D- COEFFICIENT OF HEAT TRANSFER PROGRAM

```
%Daniel J. Richardson
%4 May 97

%Coefficient of Heat Transfer Measurement

%Define Constants
Alpha=0.0042;       %Constant for Platinum Coated Tungsten Wire
L=4.15e-3;          %Probe Wire Length
D=4.7e-6;           %Probe Wire Diameter
R1=50;              %Resistance across Source
R0=0.485;           %Probe Lead Resistance
V1=2.0;             %Input Voltage form Function Generator

%Measured Voltages
V2=0.2244;              %Voltage Measured at Low Point of Rise
V3=0.2337;              %Voltage Measured at Asymptotic High

%Calculate Required Terms
A=pi*D*L;                       %Area Of Probe Wire
R2=(R1*V2)/(V1-V2)-R0;      %Probe lead Resistances
R3=(R1*V3)/(V1-V3)-R0;      %  "
dT=(R3-R2)/(R2*Alpha)       %Differential Probe Temperature

h=(V3^2)/(A*dT*R3)
```

LIST OF REFERENCES

1. Hufnagel, R.E., "Propagation Through Atmospheric Turbulence, " in The Infrared Handbook, The Infrared Analysis Center, Environmental Research Institute of Michigan, 1989.

2. Gebhardt, F. G., "High Power Laser Propagation", Applied Optics, Vol. 15, No. 6, June 1976.

3. YAL-1A Attack Laser. United States Air Force Fact Sheet. Office of Public Affairs, Phillips Laboratory. Internet source: http://www.plk.af.mil

4. "WSMR Active Tracking Experiment", ABL News .Volume I Number III, Jul 1995. Internet source: http://www.plk.af.mil/Plhome/TM/newsletters/volI_number3/jul95.html

5. Brown, James H., et al, Study of Possible Solar Heating Effects on Thermosonde Probes - Error Analysis, Geophysics Laboratory Hanscom AFB Ma., July 1989.

6. Airborne Laser Program Milestones. United States Air Force Fact Sheet. Office of Public Affairs, Phillips Laboratory.

7. Tatarski, V.I., Wave Propagation in a Turbulent Medium, Dover Publications, New York, 1961.

8. Strohbehn, J.W., "Laser Beam Propagation in the Atmosphere", Topics in Applied Physics, Vol. 25, New York, 1978.

9. Walters, D.L. and Slaven, A., Private communication, Starfire Optical Range Kirtland Air Force Base, New Mexico, April 1997.

10. Walters, D.L., "Measurement of Optical Turbulence with Higher-Order Structure Functions", Applied Optics, Vol. 34, No. 9, March 1995.

11. Klein, Miles V., and Furtak, Thomas E., Optics, John Wiley and Sons, New York, 1986.

12. Fried, D.L., "Optical Resolution Through a Randomly Inhomogenous Medium for Very Long and Very Short Exposures", Journal of the Optical Society of America, Vol. 56, August 1966.

13. Perry, A.E., Hot-wire Anemometry, Clarendon Press Oxford, 1982.

14. Brown, J.H., et al, Sonde Experiments for Comparative Measurements of Optical Turbulence, Air Force Geophysics Laboratory Hanscom Ma., February 1982.

15. Laser Aircraft Contract Announced. Office of the Assistant Secretary of Defense (Public Affairs) News Release No. 636-96, 12 November 1996. Internet source: http://www.dtic.dla.mil/defenselink /news/Nove96/b111296_bt636-96.html

16. Brown, James H. and Robert E. Good, Thermosonde and UHF Radar Measurements of C_n^2 at Westford Massachusetts - July 1981, Air Force Geophysics Laboratory Hanscom Ma., February 1984.

17. Weitekamp, M.R., Investigation of the Source of Thermosonde Measured Diurnal Variation of Optical Turbulence, M.S. Thesis, Naval Postgraduate School, Monterey, California, December 1990.

18. Roper, Daniel S., Investigation of Systematic Effects in Atmospheric Microthermal Probe Data, M.S. Naval Postgraduate School, Monterey, California, December 1992.

19. Lomas, Charles G., Fundamentals of Hot Wire Anemometry, Cambridge University Press, New York, 1986.

20. White, Frank M., Heat Transfer, Addison-Weseley Publishing Company, Reading Massachusetts, 1984.

21. White, F.M., Fluid Mechanics, New York, Mcgraw hill, 1979.

22. Richards, Bryan E., Measurement of Unsteady Fluid Dynamic Phenomena, Hemisphere Publishing Corporation, Washington, 1977.

23. Kreith, Frank, and Bohn, Mark S., Principles of Heat Transfer, Harper and Row, Publishers, New York, 1986.

24. Kothandaraman, C.P. and Subramanyan, S., Heat and Mass Transfer Handbook, Halsted Press, New York, 1975.

25. Handbook of Geophysics and the Space Environment, ed. A.S. Jursa, Air Force Geophysics Laboratory, 1985.

26. Hinze, J.O., Turbulence, McGraw-Hill, New York, 1959.

27. Collis, D.C., and Williams, M.J., "Two Dimensional Convection From Heated Wires at Low Reynolds Numbers", Journal of Fluid Mechanics, Vol. 6, 1959.

28. CRC Handbook of Chemistry and Physics, ed. Lide, David R. 71st Ed., 1991.

29. Suits, Gwynn H., "Natural Sources", The Infrared Handbook, Environmental Research Institute of Michigan, 1978. (p. 3-55)

30. Thermo Systems Incorporated

31. Blevins, Robert D., Flow-induced Vibration, Robert E. Krieger Publishing Company, Malabar, Florida, 1986.

32. Eiseberg, Robert, and Resnick, Robert, Quantum Physics of Atoms, Molecules, and Particles, John Wiley & Sons, New York, 1985.

33. Gast, V.J., Characterization of Atmospheric Turbulence for High Resolution Imaging and Laser Propagation, M.S. Thesis, Naval Postgraduate School, Monterey, California, December 1992.

34. Walters, D.L., and Kunkel, K.E., "Atmospheric Modulation Transfer Function for Desert and Mountain Location: The Atmospheric Effects on r_0", Journal of the Optical Society of America, Vol. 71, April 1981.

35. Wilson, J. and Hawkes, J.F.B., Optoelectronics, An Introduction, Prentice Hall, 1989.

36. Walters, D.L., Private communication, Naval Postgraduate School, Monterey, California, Mayl 1997.

37. Coulman, C.E., et al, "Optical Seeing - Mechanism of Formation of Thin Turbulent Laminae in the Atmosphere", Applied Optics, Vol. 34, No. 24, August 1995.

38. Walters, D.L., "Measurement of Optical Turbulence with Higher-order Structure Functions", Applied Optics, Vol. 34, No. 9, March 1995.

39. Kreith, Frank, and Black, William Z., Basic Heat Transfer, Harper and Row Publishers, New York, 1980.

INITIAL DISTRIBUTION LIST

1. Defense Technical Information Center.....2
   8725 John J. Kingman Rd., STE 0944
   Ft. Belvoir, VA. 22060-6218

2. Dudley Knox Library.....2
   Naval Postgraduate School
   411 Dyer Rd.
   Monterey, CA. 93943-5101

3. Professor Anthony A. Atchley.....1
   Chairman, Department of Physics
   Naval Postgraduate School (Code PHAc)
   Monterey, CA. 93943

4. Professor Donald L. Walters.....5
   Naval Postgraduate School (Code PHWe)
   Monterey, CA. 93943

5. LCDR Daniel J. Richardson.....5
   VP-30 Student Control
   Box 24
   NAS Jacksonville, FL. 32212-0024